UNIVERSITY of LIVERPOOL

Sliding Mode Control of Renewable Energy Generation Systems

Thesis submitted in accordance with the
requirements of the University of Liverpool
for the degree of Doctor of Philosophy

in

Electrical Engineering and Electronics

by

Mohammed Abdullah Alsumiri , BSc, MSc

May 2015

Sliding Mode Control of Renewable Energy Generation Systems

by

Mohammed Abdullah Alsumiri

All praise be to ***Allah****, there is no power and no strength save in* ***Allah****. And His peace and blessings be upon His messenger* ***Prophet Muhammad****, whose way of life has been a continuous guidance for me.*

In the name of Allah, the most Beneficent, the most Merciful

Ha, Meem. The revelation of the Book (the Holy Quran) is from Allah, the All-Mighty, the All-Wise. Indeed, within the heavens and earth are signs for the believers. And in the creation of yourselves and what He disperses of moving creatures are signs for people who are certain [in faith]. And [in] the alternation of night and day and [in] what Allah sends down from the sky of provision and gives life thereby to the earth after its lifelessness and [in His] directing of the winds are signs for a people who reason [intellectuals]. These are the evidences of Allah, which We recite to you with truth. Then in which speech after Allah and His evidences will they believe?

The Holy Quran, Chapter: Al-Jathiyah, Number: 45, Verses:1-6

Acknowledgements

First of all, I would like to praise, thank and glorify ***Allah*** for giving me strength, capability and opportunity to do this work. Then I would like to express my gratitude to all those who gave me the possibility to complete this work.

I would like to express my sincere appreciation and thanks to my supervisor Dr. Lin Jiang for his meticulous supervision, intellectual guidance, invaluable support, continuous encouragement and kind criticism throughout my doctoral studies. Thanks is extended to my previous supervisor Professor Wenhu Tang for his invaluable support and guidance at the early stage of my studies. This Ph.D. thesis would not have been possible without your generous and indispensable help.

I would like to acknowledge the Royal Commission for Jubail and Yanbu, Saudi Arabia which fully sponsored my Ph.D. study at the University of Liverpool. I am grateful to H.H. Prince Saud bin Abdullah bin Thunayan the Chairman of the Royal Commission for Jubail and Yanbu. My sincere appreciation is extended to Dr. Abdullah bin Hamad Al-Salamah the economic adviser to H.H. the Chairman of the Royal Commission for Jubail and Yanbu for his invaluable support and encouragement. Also, I am grateful to the Department of Electrical Engineering and Electronics, The University of Liverpool, for providing the research facilities, making it possible for me to conduct this research.

I am deeply indebted to my father and my mother, words are not enough to express my heartfelt thank to you. I would like to extend my sincerest thanks and appreciation to my brothers and sisters. From the bottom of my heart, I am indebted to my wife and my children for their patience, understanding, encouragement and love during the whole period of my postgraduate life.

Abstract

Sliding Mode Control of Renewable Energy Generation Systems

by

Mohammed Abdullah Alsumiri

As a result of decades of research and innovation in the renewable energy industry, advanced technologies have been developed for both wind and solar energy conversion systems. However, there are still some aspects of the systems that need to be enhanced to enable maximum and cost effective energy conversion. Wind is emerging as an alternative source for electrical power generation. Small-scale wind power generation system applications are becoming widespread because of rising fuel prices and the demand for reducing carbon emission. For such applications, vertical axis wind turbines (VAWT) appeal due to their ability to capture wind from different directions and their low noise-pollution.

Wind energy and its conversion system are studied first. The need for advanced maximum power point tracking (MPPT) controllers is discussed in literature focusing on widely implemented algorithms. Sliding mode control theory has been studied and implemented in controlling wind power generation system (WPGS). The dynamic performance of the WPGS using sliding mode control has shown improved dynamic performance, overshoot errors eliminations and higher energy conversion ratios than the widely used proportional integral (PI) control.

A new approach in WPGS control strategy by development of a novel soft control strategy based on the mathematical residue theorem has been introduced. The idea of using the residue theorem is to set a soft dynamic boundary for controlled variables around a reference point, so that controlled variables lie

on a point inside this boundary. The stability of the system has been ensured by following the Forward Euler method. The developed control strategy has been implemented in different control techniques of a small-scale permanent magnet synchronous generator (PMSG) based WPGS. The introduction of the new control approach based on residue theorem has further improved the energy conversion ratio by 2.5%. Moreover, a wind speed estimation algorithm is provided and implemented to the proposed controllers to overcome the wind speed measurements issues, i.e. cost and accuracy.

Furthermore, an improved back-EMF observer based on residual theorem has been designed to estimate the mechanical rotor speed of the PMSG using the stator current and voltage measurements. The improved back-EMF observer has overcome the well-known limitation of the classical back-EMF at low speed observation. In addition, the wind speed has been estimated using the calculated power obtained from the PMSG voltage and current measurements as well as the estimated rotor speed. Based on the wind and rotor speeds, the tip speed ratio (TSR) is calculated and controlled to its optimal value.

A MPPT controller has been developed for photovoltaic power generation systems based on a sliding mode control scheme in stand-alone configuration. The developed controller provides a solution to atmospheric conditions measurement issues and it enhances the efficiency of the PV power system. In addition, the developed controller overcomes the power oscillation around the operating point which appears in most implemented MPPT techniques. The MPPT operation is achieved by regulating the input voltage of the PV system using DC-DC boost converter topology. Moreover, a single-ended primary-inductor converter (SEPIC) topology has been employed in PV power systems. The restrictions on the application of SEPIC have been solved based on sliding mode control. The efficiency of the PV system has significantly improved.

Contents

List of Figures

List of Tables

Chapter 1

Introduction

In the last few decades the usage of renewable power plant has increased rapidly. The existence of renewable resources over a wide geographical area of the world adds substantial focus to development and research in renewable energy technology. In 2012, the global production of energy from renewable energy resource was about 13.2% [1]. Since 1990, solar photovoltaic and wind power have grown at average annual rates of 46.8% and 24.9% respectively [1]. This chapter aims to provide background information related to the field of research and an overview of the contents of this thesis. The motivations and objectives of this study are stated as well as the contributions of this research.

1.1 Introduction of Renewable Energy

Renewable power is the generation of electricity from resources which are naturally replenished such as wind, sunlight, tides, waves and geothermal heat. Due to environmental advantages and continuity of the resources, renewable energy has received much attention from both researchers and governments. In this thesis two sources of energies will be evaluated, i.e. wind and sunlight.

Wind power is the conversion of kinetic energy, which is stored in the wind, to electricity. Among all renewable power generation systems, solar photo-

voltaic and wind power have the fastest growth rate. Nowadays, wind power generation is considered one of the alternatives to conventional power generation systems [2]. Small-scale wind power generation system applications are becoming widespread because of rising fuel prices and the demand for reducing carbon emission. For such applications, vertical axis wind turbines (VAWT) are appealing due to their ability to capture wind from different directions and low noise pollution [3].

According to the European Wind Energy Association, the European total installed wind energy capacity was 208 MWatts in 2005. With an annual growth of 665 MWatts, this in 2011 became 4,200 MWatts. It has been declared that, by 2020, Europe should add around 10 GWatts to the grid, which means an increase of 165% from 2012 [4].

The conversion of sunlight into electricity, which is the second scope of this thesis, is known as solar power. This conversion can be direct, using photovoltaic, or indirect, using concentrated solar power. The concentrated solar power is in practice the heat which is generated from a reflection of sunlight using mirrors and lenses [5]. The photovoltaic solar power system, which is discussed in this thesis, is a conversion of photons to electric current.

Despite the fact that renewable energy can replace conventional sources in future, there is still some doubt regarding its cost and efficiency. Much focus has been paid either by governments, associations or researchers on overcoming these limitations. In fact the renewable energy conversion efficiencies, especially solar and wind, are highly affected by the nature of the source or variations of the atmospheric conditions, i.e. solar irradiance and wind speed. There is a widely accepted control approach to track and extract the maximum possible energy during the variations of atmospheric conditions. This control approach is called a maximum power tracking algorithm.

1.1.1 Solar Energy

The conversion of solar energy into thermal energy or electricity is highly dependent on the solar radiation where the system is located. The solar irradiance can be defined as the power flux density of solar radiation and is measured in watts per meter squared [6]. The energy density of solar radiation, which is the peak sun hours, plays an important role when designing solar energy conversion system. Since the sun is a black body, solar radiation can be modelled with that of an absolute black-body phenomena, "which is a model introduced in physics to characterize the radiation spectrum of a body with a constant temperature" [6]. It is worth noting that there are three factors affecting solar energy conversion system calculations, i.e. temperature, power density and wave length. The relationship between these factors is given by Planck's formula [6]:

$$W_\lambda = \frac{2\pi hc^2}{\lambda^5} \times \frac{1}{e^{hc/\lambda kT} - 1} W/m^2, \tag{1.1.1}$$

where h is the Planck's constant ($6.63 \times 10^{34} Ws^2$), k is the Boltzmann's constant (1.38×10^{23}) and c is the speed of light in vacuum which is $299,722,458 m/s$. λ is the wavelength and T is temperature.

As mentioned previously, electricity can be generated from sunlight using photovoltaic technology. The electrons on the semiconductor materials absorb the energy stored in the photons from the sun and electricity is generated in the form of a DC current [7]. Typically, an individual PV cell can produce 1 or 2 Watts of power and is connected in series and parallel combination with other PV cells to boost the output power. This combination of PV cells is called PV modules. Similarly, a set of PV modules can be connected together to form a PV array capable of producing more power [7].

Solar power generation using photovoltaic is a promising alternative to the conventional power generation system. It can be considered the fastest and easiest provider of electrical power. Several advantages stand out in photo-

voltaic power generation systems, i.e. short time to design and install a new photovoltaic power plant, noiseless operation, and require less maintenance because of its static structure and, of course, availability globally [8].

However, the initial cost and the lower energy conversion efficiency limit the applications of the photovoltaic power generation system. Fortunately, this initial cost will be reduced as new technology makes it suitable and attractive for residential applications [8].

As mentioned previously, photovoltaic power generation systems are highly affected by the variations in atmospheric conditions, so that the maximum power operating point varies as the atmospheric conditions change, i.e. solar irradiance and ambient temperature. As a result, it is necessary to develop and implement a maximum power point tracking algorithm. Many MPPT algorithms use microprocessors for flexibility and compatibility with various photovoltaic power generation systems [9, 10]. The nonlinearity nature of photovoltaic power generation systems, in terms of the output power and current, introduces the requirement for continuous adjustment of the photovoltaic terminal voltage for the correct achievement of maximum power point operation [9].

1.1.2 Wind Power

Wind is the power that forces the air to move from high pressure to low pressure areas. The kinetic energy in the wind is proportional to the cube of the wind speed. In fact, the wind speed is affected by some geographic factors such as temperature, height above sea level and humidity [11]. The wind speed is high in high places, such as on the top of mountains and hills and also offshore locations. Given that wind power is related to the cubic of the wind speed, a slight change in wind speed will produce a noticeable change in power. For example, if the wind speed is reduced by 50% the power will reduce by 87.5%.

Albert Betz, a German physicist, found a maximum theoretical limit that can be harvested from the wind's kinetic energy. This limit is about 59.3% of the wind power [12]. However, this will further fall when power is being converted from mechanical energy to electrical energy. For example if the efficiency is 70%, the converted power from the wind energy to electric power is 41.5%.

The power in the wind is determined by the amount of air molecules moving across an area during a period of time [11]. This can be defined as the perpendicular area of the wind flow. The mass in the volume of the cylinder, m, which passes across an area, A, in a period of time, t, can be determined from, ρ which is the air density and V which is the volume of the cylinder. KE is the kinetic energy stored in the wind.

$$KE = \frac{1}{2}mv^2, \tag{1.1.2}$$

$$P = \frac{KE}{t} = \frac{0.5mv^2}{t}, \tag{1.1.3}$$

$$\rho = \frac{m}{V}, \tag{1.1.4}$$

$$V = \text{area} \times \text{length} = AL, \tag{1.1.5}$$

$$m = \rho V = \rho AL. \tag{1.1.6}$$

The velocity of air molecules is

$$v = \frac{L}{t}, \tag{1.1.7}$$

By substituting the value of v, we get:

$$P = 0.5\rho Av^3. \tag{1.1.8}$$

The power per unit area can be defined as:

$$\frac{P}{A} = 0.5\rho v^3. \tag{1.1.9}$$

The change in wind direction or speed over a distance can be defined as wind shear. However, the wind shear might be vertical or horizontal. The horizontal wind shear, which is the change of wind speed with height, is an important factor in wind turbine power estimation calculations [11, 13]. A general method of calculating wind speed at greater height with respect to a known wind speed at lower height is:

$$\frac{V_m(h)}{V_m(h_{ref})} = \frac{\ln(\frac{h}{h_0})}{\ln(\frac{h_{ref}}{h_0})}, \tag{1.1.10}$$

where V_m is the maximum wind speed, h is the height above ground, h_{ref} is the reference height (typically 10m). The surface roughness length (h_0) is the height above ground level where the wind speed is theoretically zero. The power law for a wind shear is:

$$v = v_0(\frac{h}{h_0})^{\alpha}, \tag{1.1.11}$$

where v_0 is the measured value of wind speed and h is height. The wind shear exponent α is about 0.14 for stable weather conditions and varies for different weather conditions [13].

1.1.3 Wind Power Generation System

For wind power generation systems, the device which transforms the wind flow to mechanical rotation is the wind turbine. There are two classifications of wind turbine, according to their axis [14]. The first is the horizontal axis wind turbine (HAWT) in which, the mechanical axis is horizontal. The second is the vertical axis wind turbine (VAWT) in which the mechanical axis is vertical. Figures 1.1 and 1.2 show the typical horizontal and vertical axial wind turbines respectively.

In the horizontal axis wind turbine, the generator and the gearbox are typically located at the top of the tower. In fact, HAWTs have a high energy conversion ratio [15]. Because of yaw mechanism required for orientation,

HAWTs could be self-starting [16]. However, the installation costs of horizontal axis wind turbines are relatively high as they need stronger towers due to the location of the generator and gearbox [15].

A vertical axis wind turbine, in which the spin axis is perpendicular to the ground, is cost effective. The generator and the gearbox are located at ground level [15]. One major advantage of the vertical axis wind turbine over the horizontal is that the operation of the vertical axis wind turbine is independent of the direction of the wind [17].

Figure 1.1: Offshore horizontal axis wind turbine [18]

The main drawbacks of WPGS are the low efficiency and the high initial cost. To overcome these drawbacks, the optimal operation point should be achieved either by controlling the blade pitch angle or by controlling the tip speed ratio (TSR), which is the ratio between the rotation speed and the wind speed [20]. For small-scale WPGS the only possible control variable for

Figure 1.2: Small-scale vertical axis wind turbine [19].

achieving higher efficiency is the TSR, which can be controlled by adjusting the rotation speed with respect to wind speed. By adjusting the speed of rotation in order to satisfy the optimal TSR, the highest possible energy can be converted from the wind and highest possible power coefficient, (C_p), can be achieved [21]. The power coefficient is defined as the ratio of the electricity produced by wind turbine to total energy available in the wind. The operation of WPGS can be classified into two categories [22]:

1 . Constant speed wind turbines, in which the pitch angle will control the wind turbine blade to maintain, a constant speed of rotation, hence the power is constant.

2 . Variable speed wind turbines, in which the speed of rotation is adjusted to achieve a constant power coefficient [23].

The use of variable speed wind turbines can maximise the energy conversion efficiency since the operation speed can be varied in accordance with the wind speed [24, 25]. The rotation speed variation in which the maximum energy conversion is ensured can be achieved using the power electronic converter. In fact, the applications and the requirements of a system can suggest which converter topology to be used [26]. Another advantage of using variable speed wind turbines with AC generators is the simplicity of controlling the output voltage in battery charging applications [22, 27]. The simplicity arises from the usage of power electronics circuits which can control the output voltage and frequency. In this research variable speed wind turbine has been employed. Maximum power point tracking (MPPT) techniques are implemented to determine the optimal TSR. MPPT can be obtained by either the knowledge of the wind turbine characteristics, such as C_p versus TSR curve, or by estimating the optimal reference signals of the control system [28]. Therefore, an advanced controller should be developed and implemented instead of the classical PI controller in order to [29]:

i . Ensure better disturbance rejection.

ii . Maintain required control quality in the wider operating range.

iii . Shorten the frequency's transient responses, avoiding the overshoots.

iv . Be robust to uncertainties in the system.

Any application rating up to 50kW can be considered a small-scale application. The applications of small-scale WPGS have increased over the last few decades, especially domestic applications. For such applications, VAWT has received much attention because of its arrangement allowing easy access for generator maintenance and reducing the load on the turbine tower [30]. The configuration of the small-scale WPGS is illustrated in Figure 1.3.

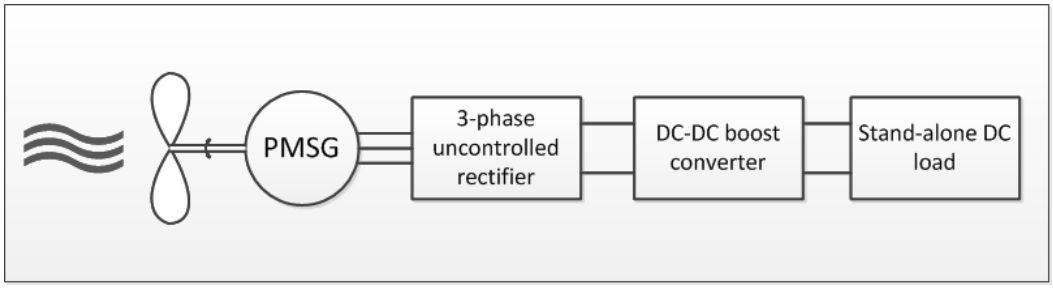

Figure 1.3: Small-scale PMSG-based WPGS.

1.2 Control of Wind Power Generation System

Renewable energy conversion systems are the structures in which the energy is transformed from its renewable resource to electrical energy [31]. Control plays an important role in advanced renewable energy conversion systems. The idea of improving the energy conversion efficiency by advanced control has been highlighted in many articles published in the field. Generally, the objectives of the control system are to protect and to optimize the operation. In renewable energy conversion systems, the most important objective of the control is having the ability to cope with the unpredictable nature of the renewable resources [31].

1.2.1 Literature Review

Permanent magnet synchronous generators (PMSGs) have the most advantages over other types of electrical generators used in wind power generation systems, since they are stable under normal operation and do not require an external DC supply for the excitation windings. Initially they were used only for small and medium power ratings, nowadays, PMSGs are also used for higher power ratings because of their advantages [32]. WPGS is a cost effective solution for stand-alone power generation, such as street lighting utilities.

In fact, wind power generators mostly serve at low speeds, since the speed of the wind is limited [6]. There are two ways to couple a generator and prime mover. One way is direct coupling, which is shaft to shaft connection, and the other is to couple them through a mechanical gear box system. The selection of the coupling method depends on the generator type. For example, PMSG is a low speed generator, hence, direct coupling to the prime mover is preferred. The absence of the mechanical gearbox provides an advantage by reducing the mechanical power losses which will increase the overall system efficiency [33]. In some cases, the use of a mechanical gearbox is a must regardless the losses, i.e. when the rated generator speed is higher than the turbine's speed. However, it can be effective for wind power generation systems that employ induction generators. Basically, induction generators were not designed to operate and generate electrical power at low speed. Nevertheless, the use of low speed induction generators is valid. It requires a specially designed generator with higher air gap strength, which means the size of the induction generator will be twice the size of the PMSG for the same power rating. This topology will also reduces the energy conversion system efficiency [6].

There were many studies on the effectiveness of large-scale power generation from wind but the results highlight some limitations, such as the certainty of the location and the high initial cost. Noise pollution is another major limitation. However, it has been suggested to generate a power at a small-scale because of the higher advantages gained, such as cost effectiveness, simple construction, as well as flexibility [34]. Also, it has been recommended to employ a PMSG instead of induction generation and to implement a sensorless controller.

The effect of excess wind speed on the variable speed wind generator was discussed in [35], where the techniques in limiting the voltage to the grid were also investigated. It was deduced that there are methods to limit the aerodynamic conversion under high wind speed. These methods are either pitch control, in which the blades are turned out of the wind, stall control, in which

the blades lose their aerodynamic efficiency at higher wind speed or passive stall control.

A phase delay speed controller with a single anemometer was investigated in [36]. It was concluded that for a large-scale wind turbine a single anemometer cannot measure the entire wind speed acting since the turbine's rotor sweeps a large area. Also, from a control point of view, was the implementation of a classical PI controller to improve the system dynamic performance are advised.

It can be concluded from the previous discussions that the wind energy conversion system is an efficient source of renewable energy at small-scale because of its advantages. Also, it has been recommended to employ a PMSG in a sensorsless control configuration as a cost effective energy conversion system.

The design of the controller and the control strategy play an important role in achieving an efficient power conversion ratio. Most of the studies focused on implementing a MPPT control technique due ti its influence on harvesting the maximum possible power from the wind. Although they almost focused on the same strategy, they developed different MPPT control algorithms. Other important topics to mention are the elimination of the mechanical sensors, since their cost are relatively high, as well as the disadvantages of the mechanical equipment and coupling.

Basically, there are two well known methods to determine the maximum power point, i.e. the anemometer or calculations [37, 38, 39]. In the anemometer method, the wind speed is measured and a look up table is used to match the measured wind speed with corresponding value of power. In the calculations method, the rotation speed is calculated using the electrical parameters at the output terminals of the generator. However, the anemometer method is unsuitable method for small-scale applications because it will add an extra cost. This method can be suitable for large-scale application since the cost of the anemometer is lower compared to the initial cost of the system. The calculations method can be preferred for PMSG-based WPGS in small-scale

applications since the frequency is directly proportional to the angular acceleration of the rotor. Hence, the power can be calculated using the power versus speed curve [38]. However, a discussion on the operation and control of small and medium wind turbines with fixed blades angle has been summarised in [40]. The performance and operation were evaluated under MPPT control technique by implementing a digital control. The research findings deduced that feed-forward process gives better results and operation than the MPPT.

A nonlinear control theory improves the performance and the speed achievement to the tracked maximum power point speed [41]. In order to achieve a high performance controller at low speed, mechanical speed sensors are required. Most sensorless controllers techniques are unstable at low speed since the estimation techniques are parameter dependent, especially the classical back-EMF speed observer. Several methods have been reported using high frequency signal injection neglecting the back-EMF and stator resistance, where the speed and position is estimated using the variations of the machine inductance [42, 43, 44]. A wind speed and rotor position sensorless control for wind turbines directly driving permanent magnetic generators was proposed in [45]. The rotor position was estimated using a sliding-mode observer, which uses the stator currents measurements, and the voltages were obtained from the machine-side converter controller. [46] provided a solution to deal with unknown wind speeds. The wind speed is estimated using the efficiency curve of the blade. Most of the back-EMF observers reported in literature applied a low pass filter, which null the high frequency components, as well as introduce the required phase delay for an accurate commutation [47]. However, the magnitude of the back-EMF is small at low-speed, which results in lack of robustness. Moreover, the size of the filter is a function of speed so that the filter will not work effectively in variable speed operations. An adaptive filter size was proposed in [48]. The filter time constant was designed to vary with speed variations. Adaptive filter approach can provide an appropriate solution

for large-scale PMSG-based WPGS, since the magnitude of the back-EMF is high at low-speed.

The limitations of the extracted power from wind, which is 59% according to the Betz limit, make it necessary to employ MPPT controllers to achieve the highest possible power conversion from WPGS. In fact, many MPPT algorithms have been proposed. [49, 50] propose modified hill climb for optimal operating point search, the results show acceptable performance. A TSR observer was proposed in [51], using perturbation and observation method, and compared to optimum TSR value.

Obtaining MPPT operation during high variations in wind speed causes stress on the shaft and overshoots in the speed response [52]. However, the idea of having two control loops exists to limit the power during high wind speed. The transition between the operating regions can also cause damage to the WPGS [53]. The transition can be achieved either by activating both controllers together or by activating the one control loop at a time, which can be ensured using logic switches [54, 53]. However, there will be occasions where the controllers either activate the wrong loop or interface close to the rated operating point [55]. A new control strategy with DC-DC converter was proposed in [56]. Two MPPT algorithms have been developed for controlling the speed under two different modes of operation, i.e. normal power point and limited power point (LPP) algorithms. LPP is a predetermined reduced point under restricted conditions.

It can be deduced from the above argument that the MPPT is required for achieving efficient energy conversion. The anemometer method is preferred to avoid the osculations around the reference point, which is a major drawback of hill climbing search. It can also be concluded that the speed observation technique is a serious issue for low speed WPSG, since the well known classical back-EMF observer has poor performance at low speed estimation.

The disturbances cause a nonlinear dynamic effect to the wind power gen-

eration system. Since the uncertainties of the system dynamic are significant, the WPGS can be described as a complex nonlinear system which operates in noisy environments. For the WPG control system to achieve the desired output, the implementation of nonlinear control is necessary. Nonlinear feedback control based on differential geometric has received much attention regardless of the fact that it is still weak in handling uncertainties. Several approaches for feedback linearisation methods, such as dynamic surface control, have been developed to overcome the problem [57]. Lyapunov-based control design techniques such as sliding mode control have good ability to handle fast-time varying and functional uncertainties and can replace the nonlinear feedback control in such environments.

Lyapunov control design techniques, in which the uncertainty satisfies the matching condition with defined upper bound, are commonly employed to stabilise uncertain dynamical systems [58, 59, 60]. This technique allow the existence of continuous state feedback controllers so that the convergence of the state to the origin ensures in finite time. Some robust control theories deal with linear system and the results are obtained by assuming the nominal part of the system is linear. When the actual system exhibits nonlinear behavior, its uncertainty element must be chosen sufficiently large to encompass the nonlinear phenomena, because its normal part is restricted to be linear [58]. A major drawback of such method is the ignorance of the nonlinearity of the system, which can result in over conservative control in high nonlinearity systems. Designing a robust control Lyapunov function, which allows the nominal plant to be nonlinear, can improve the disadvantage of robust linear control [58, 60].

Recently, extensive research has been undertaken on controlling PMSG for wind energy conversion applications. [61, 62] suggested to follow a second order sliding mode approach, so that a finite time reaching and robustness during the wind perturbation can be achieved. In addition, a combined high order sliding mode controller was reported in [63], in which the system tracked an

average point rather than a fixed point. This technique can ensure maximum conversion of power only when the wind perturbation is small, so that the average point is around the actual maximum power point. It can be deduced that high order SMC is more applicable for large-scale WPGS than small-scale WPGS, since the cost for the large-scale WPGS is high and the simplicity of implementations are not a concern.

A constant gain of SMC is required to be maintained in order to achieve a robust and finite time convergence of the sliding boundary. However, using a constant gain does not allow the compensation in the uncertainty of state variable [64, 65]. A further drawback of a constant gain is that a steady-state error during wind speed variations may be introduced.

Nonlinear adaptive control of nonlinear system was reported in [58]. The state and perturbation were observed using sliding mode observer and a high gain observer. It has been deduced that the estimation accuracy is improved when the driving term of the observer error dynamic is reduced. Also, the adaptive control law has been obtained using the estimated nonlinear function rather than parameters estimation. Uncertainties elimination was a solution provided in [66, 67]. The idea is to eliminate the nonlinear dynamics and the uncertainties by using the time delay values of the control input as well as the state variables derivation which occur at a previous point.

1.2.2 Problems

The classical proportional integral (PI) control, which is widely accepted in industry, has difficulties in controlling nonlinear systems. Feedback linearisation can be a solution for some applications. The idea of feedback linearisation is to transform the nonlinear system to an equivalent simple linear system, either by full or partial transformation. However, feedback linearisation does not have the ability to handle the uncertainties of generator parameters vari-

ations or external load disturbances [58, 57]. Moreover, the parameters of the PI controller cannot be easily adapted [68].

Due to these limitations, which will in fact significantly affect the energy conversion ratio, Lyapunov-based control design techniques such as sliding mode can be the appropriate solution. Sliding mode control is a discontinuous control which is powerful in handling uncertainties and disturbances. The discontinuity nature of sliding mode introduces the ultimate robustness of the controller. The sliding mode control forces the operating point to reach the sliding surface by increasing the switching gain [68]. As a result of the discontinuity nature and switching gain, large chattering will be introduced in the system dynamic performance. Chattering effect can be described as oscillations in the output response with less than infinity frequency. It is worth mentioning that when the discontinuity dynamics change, the ultimate robustness and accuracy of the sliding mode nature are partially lost [62].

1.3 Motivations and Objectives

The amount of energy extracted from renewable sources is limited, so it becomes necessary to implement efficient control algorithms to maximize the energy conversion ratio. However, the classical control algorithms such as the hill climbing technique cannot obtain the desired objectives as well as satisfactory dynamic performance, since wind power systems are nonlinear. The challenges in such systems can be described as a chain containing efficiency, complex control algorithm and cost, each one of which affects the other two factors.

As discussed previously, the complexity of control algorithms leads to an increment in the system cost. This can be considered one of the issues which limits the widespread usage of renewable power generation. Also, most control algorithms nowadays implement reference signals using mechanical speed mea-

surements, i.e. encoders and anemometers. In fact, some control algorithms use more than one anemometer to improve system efficiency. Apart from the cost caused by the mechanical speed measurements, they introduce a DC offset that can reduce the reliability of the system and can drive the system to instability.

The challenges in reducing the overall cost of renewable power generation systems, which has high demand, still exist especially with reference to WPG industry. The major objectives of this thesis are to develop a simple and efficient control system, which can reduce the cost and improve the efficiency of the wind power generation system and the solar PV power system.

1.4 Contribution of Research

In order of importance, the major contributions of this thesis can be summarised as the followings:

1 . A new MPPT control approach has been developed for WPGS. This control approach can be adapted to non-linear systems since it can handle the uncertainties of a non-linear system. The aim is to generate a soft dynamic controlled boundary by implementing the mathematical residue theorem and to force the operating point to lie on a point inside the controlled boundary. This point represents the reference maximum power operation point. The developed soft dynamic boundary control approach can overcome some major drawbacks of the commonly used control strategies in terms of handling uncertainties and robustness.

2 . Based on the new control approach, an improved back-EMF observer has been proposed. The observer has been developed using the residual value of the back-EMF. As the investigated WPGS operates at low speed, it has been deduced in literature that the classical back-EMF observer has

poor performance at low speed operation. The improved back-EMF observer using residual back-EMF values has better performance and more accurate speed estimation than the classical back-EMF observer at low speed.

3 . Based on the improved back-EMF observer, a sensorless MPPT TSR controller has been developed. A direct wind speed estimation using the generated power has been proposed and implemented.

4 . A photovoltaic power conversion system has been investigated. Sliding mode control has been implemented for MPPT controller for the PV power system. A dynamic sliding surface has been proposed for the MPPT controller. This surface insures the maximum power operating point and does not require atmospheric condition measurements.

5 . A new application of single-ended primary inductor in PV power system has been investigated. The difficulties of the control design have been simplified using sliding mode control with dynamic sliding surface.

6 . Adaptive gain sliding mode MPPT controller has been proposed for WPGS. The design and implementation of the adaptive gains improve the dynamic performance of the WPGS, in terms of eliminating the overshoot errors and improving the respond time, during rapid wind variations.

7 . Rotor and wind speeds estimations have been proposed using fuzzy inference system. The developed fuzzy rotor speed estimator can estimate the rotor speed at low speeds which is a drawback of the classical back-EMF observer. The fuzzy inference system has been developed using the torque component of the permanent magnet synchronous generator current.

Based on the above contributions several papers have been published. The publications are listed below:

1. **MA Alsumiri**, WH Tang, and QH Wu. Maximum power point tracking for wind generator system using sliding mode control. *In Power and Energy Engineering Conference (APPEEC), 2013 IEEE PES Asia-Pacific*, pages 1-6. IEEE, 2013.

2. **MA Alsumiri**, WH Tang, and QH Wu. Wind and Rotor Speeds Estimation Using Fuzzy Inference System for Wind Generation System. 7^{th} *Saudi Students Conference-UK, The University of Edinburgh*, Edinburgh, UK, 2014

3. **MA Alsumiri**, L. Jiang, and W. H. Tang. Maximum Power Point Tracking Controller for Photovoltaic System Using Sliding Mode Control. 3^{rd} *Renewable Power Generation Conference (RPG 2014)*, page 7.3.3 (2014): 7-3. IET,2014

4. **MA Alsumiri**, L. Jiang, and W. H. Tang. Sliding Mode Maximum Power Point Tracking Controller for Photovoltaic Energy Conversion System with SEPIC Converter. 8^{th} *Saudi Students Conference-UK, Imperial College London*, London, UK, 2015.

5. **MA Alsumiri**, L. Jiang, Liuyin Li, and W. H. Tang. A New Approach In Maximum Power Point Tracking Controller for Wind Power Generation System Using Residue Theorem. Manuscript has been submitted to IET Renewable Power Generation Journal, March, 2015.

6. Liuying Li, Yaxing Ren, **Mohammed Alsumiri**, Joseph Brindley, Lin Jiang. A Self Learning Algorithm to Detect Optimal Power Curve in Wind Turbine Generation Systems for Maximum Power Point Tracking. Manuscript has been submitted to the 4^{th} *Renewable Power Generation Conference (RPG 2015).*

1.5 Thesis Outline

As the introduction of the thesis, Chapter 2 illustrates the PMSG-based WPGS model. The PMSG has been presented in the *abc* stationary reference frame. The Clarke and Park transformations have been applied to the PMSG model in the stationary reference frame in order to represent the PMSG in the *dq* rotating reference frame. Also, the DC-DC boost converter has been studied and the small signal model illustrated. A discussion on the classic control is included and applied to the wind power generation system.

Chapter 3 focuses on the control strategies of wind power generation systems, which implement permanent magnet synchronous generators. The sliding mode control theory is studied in this chapter. Different MPPT controllers have been proposed using sliding mode control. Moreover, in this chapter the dynamic performance of the PMSG-based WPGS is compared using the classical PI controller and the proposed SMC.

A new approach in maximum power tracking controller for wind power generation systems is proposed in Chapter 4. The new approach uses the mathematical residue theorem. The related literature is stated in the introduction section, as well as a mathematical overview. The development of the new control strategy is discussed throughout this chapter. The design equation and the proofs are provided. Different MPPT controllers are proposed and tested using the new control strategy and covered within the chapter. Moreover, the experimental verifications of the new control strategy are provided. The WPGS simulator is demonstrated. A real time implementation of the proposed control approach has been completed using dSPACE. The result analysis and validations of the new control approach are discussed in detail.

Chapter 5 introduces an improved back-EMF observer using the residual value of the speed. Also, in this chapter, the proposed observer as well as the wind speed estimator are used for the development of sensorless tip speed ratio

maximum power point tracking controller for wind power generation systems. The introduction of the chapter covers the related literature and background information. In addition, a sensorless MPPT controller for WPGS is proposed using the hill climb algorithm. The description of the algorithm and the operation of the proposed hill climb MPPT algorithm are illustrated and analysed. Moreover, a comparative study between the two controllers that are described in this chapter has been undertaken.

Also in this chapter, fuzzy inference systems are introduced. A rotor speed and a wind speed estimator are proposed using a fuzzy inference system. FIS design is described step by step and the results of both estimators are illustrated. Classical back-EMF speed observer is discussed and tested, and finally, in the conclusion section, a comparison between the proposed fuzzy rotor speed estimator and the back-EMF speed observer is undertaken.

Photovoltaic power conversion systems are studied in Chapter 6. The applications of DC-DC power converter circuitry are investigated in this chapter. A new application of single ended primary inductor converter topology on PV power system is introduced. The converter design and its control system are covered in this chapter. The performance of PV power system using the single ended primary inductor converter is compared with that using boost converter topology. The background information and the literature review of the investigated topologies are covered in the introduction section of this chapter.

Finally, a summary of the thesis findings are presented in Chapter 7, along with, some suggestions for future research work.

Chapter 2

Modeling of Permanent Magnet Synchronous Generator Based Wind Power Generation System

This chapter introduces the electrical model of a permanent magnet synchronous generator based wind power generation system. The electrical model in *abc* stationary reference frame is illustrated. The steps in modeling the PMSG in the $d-q$ rotating reference frame are discussed including Clarke and Park transformations. Also, this chapter studies the classical control of WPGS. The dynamic performance of the WPGS has been discussed using classical control.

2.1 Modeling of the Wind Power Generation System

The Investigated PMSG-based WPGS consist of a VAWT directly coupled to a PMSG which fed a stand-alone DC load through uncontrolled rectifier and DC-DC boost converter. Figure 1.3 illustrates the block diagram of the

investigated PMSG-based WPGS. The advantages of such configuration, where a mechanical gearbox is not used, is reducing the power loss and decreasing the WPGS cost. The uncontrolled 3-phase diode rectifier which is directly connected to the output terminals of the PMSG provides DC voltage and current to the boost converter. The boost converter is controlled to achieve a MPPT operation. The power rating for the investigated system is 165 Watts.

2.1.1 Wind Turbine Model

The output power of the wind turbine is the extracted kinetic energy stored on the wind by a power coefficient. The wind power is related to the cube of the wind speed [11, 69].

$$P_w = \frac{1}{2}\rho A V_w^3, \tag{2.1.1}$$

where ρ is air density, A is the swept area of the wind turbine and V_w is the wind speed. The mechanical power is calculated using a power coefficient as follows:

$$P_m = \frac{1}{2}\rho C_p A V_w^3. \tag{2.1.2}$$

The calculation of the power coefficient depends on the wind turbine type either vertical axis or horizontal axis wind turbine type. The power coefficient C_p is a function of the tip speed ratio and the pitch angle of the blade. This relationship is provided by the manufacturer of the wind turbine. However, the relationship is a set of non-dimensional curves. In order to approximate the value of the power coefficient many polynomials were introduced. Most of them consider the effect of the pitch angle [70, 71]. Generally, for all small-scale WPGS the pitch angle is fixed so that the cost of controlling the mechanical pitch angle is avoided. The equation which relates the C_p and the tip speed ratio (TSR) λ is as follows [11]:

$$C_p = -0.13\lambda^3 - 0.12\lambda^2 + 0.45\lambda, \tag{2.1.3}$$

$$\lambda = \frac{\omega_r R}{V_w}, \tag{2.1.4}$$

where R is the radius of the wind turbine rotor, which is $0.381m$ for the investigated VAWT, ω_r is the rotational speed. The coefficients of the above equation have been obtained and approximated using curve-fitting techniques. The characteristics of the wind turbine are calculated and the power versus rotational speed curve is computed and shown in Fig. 2.1. The top points of each curve indicate the maximum power point correspond to a mechanical speed. In order to achieve maximum power extraction the operation point should always be at the top of curve. As seen from Fig. 2.1 as the wind speed is changing the power curve changes so to overcome the change of wind speed and to mention MPPT operation a variable speed operation is required.

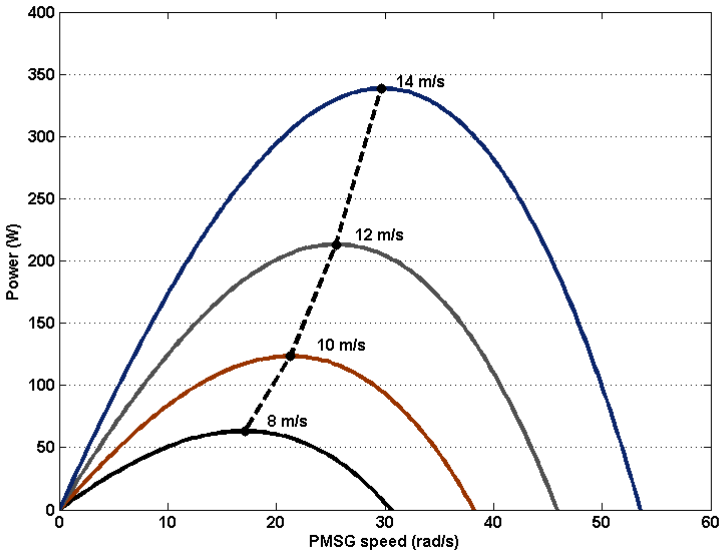

Figure 2.1: Power versus speed curve of the investigated VAWT.

2.1.2 Dynamic Model of PMSG

In understanding and investigating PMSG behavior and operation, PMSG is represented in a mathematical form. The stator of PMSG consists of three

windings with equal number of turns N, hence they are of the same resistance R_a [72, 73]. These windings are distributed along the stator in such a way that the induced flux is sinusoidal and the displacements of the three windings are 120 electrical degrees. So the three phases are formed and the voltage equations can be represented as follows:

$$\begin{bmatrix} V_a \\ V_b \\ V_c \end{bmatrix} = R_a \begin{bmatrix} i_a \\ i_b \\ i_c \end{bmatrix} + \frac{d}{dt} \begin{bmatrix} \psi_a \\ \psi_b \\ \psi_c \end{bmatrix}, \tag{2.1.5}$$

where V_a, V_b and V_c are the voltages of the three phase windings, i_a, i_b and i_c are the currents of the three phase windings. ψ_a, ψ_b and ψ_c are the flux linkages of the three phase windings. These flux linkages are the sum of the self and mutual inductances and can be represented as follows:

$$\begin{bmatrix} \psi_a \\ \psi_b \\ \psi_c \end{bmatrix} = \begin{bmatrix} L_{aa} & L_{ab} & L_{ac} \\ L_{ba} & L_{bb} & L_{bc} \\ L_{ca} & L_{cb} & L_{cc} \end{bmatrix} \frac{d}{dt} \begin{bmatrix} i_a \\ i_b \\ i_c \end{bmatrix} + \psi_{PM} \begin{bmatrix} \sin(\theta_e) \\ \sin(\theta_e - \frac{2\pi}{3}) \\ \sin(\theta_e + \frac{2\pi}{3}) \end{bmatrix} \tag{2.1.6}$$

where ψ_{PM} is the permanent magnet rotor flux, θ_e are the electrical displacement angle and L_{aa}, L_{bb} and L_{cc} represent the self inductances of phase a, b and c respectively. The mutual inductances of phase a are represented as L_{ab} and L_{ac} and same to mutual inductances of the other two phases. The PMSG can be represented in the space vector as follows:

$$v_{abc} = \frac{2}{3}(v_a + av_b + a^2 v_c), \tag{2.1.7}$$

$$i_{abc} = \frac{2}{3}(i_a + ai_b + a^2 i_c), \tag{2.1.8}$$

$$\psi_{abc} = \frac{2}{3}(\psi_a + a\psi_b + a^2 \psi_c), \tag{2.1.9}$$

where a represents the 120 electrical degree phase shift between the windings. The dynamic model of PMSG has been developed in the dq synchronous reference frame in which the d-axis is aligned with the magnet axis and the q-axis

is orthogonal to the d-axis with respect to the direction of rotation. Figure 2.2 shows the transformation stages and axis. These transformation has been performed through two stages. The first stage is the Clarke transformation in which the 3-phase fixed coordinates are transformed to the fixed 2-axis $(\alpha - \beta)$ coordinate [74].

$$i_\alpha = i_a, \tag{2.1.10}$$

$$i_\beta = \frac{1}{\sqrt{3}} i_a + \frac{2}{\sqrt{3}} i_b. \tag{2.1.11}$$

The second stage is the Park transformation in which the fixed 2-axis co-

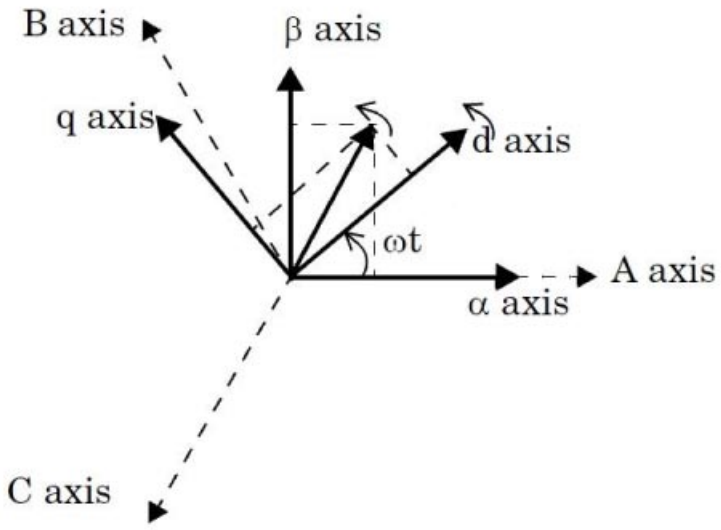

Figure 2.2: Transformation from abc to dq0 [73].

ordinates $\alpha - \beta$ are converted to a synchronous rotating coordinate$(d - q)$, which rotates at the synchronous speed, by introducing the mechanical rotor displacement angle $\theta = \omega t$ [74].

$$i_d = i_\alpha \cos(\theta) + i_\beta \sin(\theta), \tag{2.1.12}$$

$$i_q = -i_\alpha \sin(\theta) + i_\beta \cos(\theta). \tag{2.1.13}$$

The PMSG can be represented in the $d-q$ synchronous reference frame as follows:

$$V_{dq} = R_a i_{abc} e^{-j\theta_e} + \frac{d}{dt}\psi_{abc} e^{-j\theta_e}, \tag{2.1.14}$$

where,

$$\psi_{dq} = \psi_{abc} e^{j\theta_e}, \tag{2.1.15}$$

$$e^{j\theta_e} = \cos(\theta_e) + j\sin(\theta_e), \tag{2.1.16}$$

$$\theta = \omega t. \tag{2.1.17}$$

Therefore,

$$V_{dq} = R_a i_{abc} e^{-j\theta_e} + e^{-j\theta_e}\frac{d}{dt}\psi_{dq} e^{j\theta_e}, \tag{2.1.18}$$

$$V_{dq} = R_a i_{dq} + \frac{d}{dt}\psi_{dq} + jw\psi dq. \tag{2.1.19}$$

Rearranging the equations by representing the inductances we got,

$$V_d = R_a i_d + \frac{d}{dt}(L_s + L_{md})i_d - w_e(L_s + L_{mq})iq, \tag{2.1.20}$$

$$V_q = R_a i_q + \frac{d}{dt}(L_s + L_{mq})i_q + w_e(L_s + L_{md})id + w_e\psi_{PM}, \tag{2.1.21}$$

where L_s are the self inductance and L_{md} and L_{mq} are the mutual inductances between the d and q axis. By introducing,

$$L_d = L_s + L_{md}, \tag{2.1.22}$$

$$L_q = L_s + L_{mq}, \tag{2.1.23}$$

we got,

$$V_d = R_a i_d + L_d\frac{di_d}{dt} - \omega_e L_q i_q, \tag{2.1.24}$$

$$V_q = R_a i_q + L_q\frac{di_q}{dt} + \omega_e(L_d i_d + \psi_{PM}). \tag{2.1.25}$$

The mechanical equation which describes the mechanical behavior of the generator is as follows:

$$T_m = T_e + J\frac{d\omega_r}{dt} + B\omega_r, \tag{2.1.26}$$

$$\omega_e = p\omega_r, \tag{2.1.27}$$

$$T_e = 1.5p(\psi_{PM} i_q + (L_d - L_q) i_d i_q). \tag{2.1.28}$$

where T_m and T_e are the mechanical and electrical torques respectively. B and J are the fractional and the inertia of PMSG. p is the number of pole pairs.

2.1.3 Linearise PMSG model

In order to implement vector control strategy the linearisation of the voltage equation is needed. The linearisation of the PMSG model is done by removing the cross-coupling between the dq-axis voltages [75]. This cross coupling can be seen in voltage equations in terms of $(-\omega_e L_q i_q)$ and $(\omega_e(L_d i_d + \psi_{PM}))$ for d-axis and q-axis respectively. The dq-axis voltages equations after removing the cross-coupling are as follow:

$$V_d = R_s i_d + L_d\frac{di_d}{dt}, \tag{2.1.29}$$

$$V_q = R_s i_q + L_q\frac{di_q}{dt}. \tag{2.1.30}$$

The advantages of the linearisation can be surmised as:

i . The simplicity of current controller design.

ii . The accuracy of the control is increased since d-axis and q-axis currents are controlled independently.

2.2 DC-DC Boost Converter

The DC-DC boost converter is a popular non-isolated power stage topology; it can be described as a step-up power stage. In the boost power stage the output voltage is always greater than the input voltage [76]. Figure 2.3 shows the basic construction of a boost power stage. The design of a boost converter requires at least one power electronics switch, usually MOSFET or IGBT, and a diode. The inductor and capacitor is to make-up the output filter [77]. Also, the output capacitor supplies the load current during the ON state. Figures 2.4 and 2.5 shows the ON and OFF states equivalent circuit respectively.

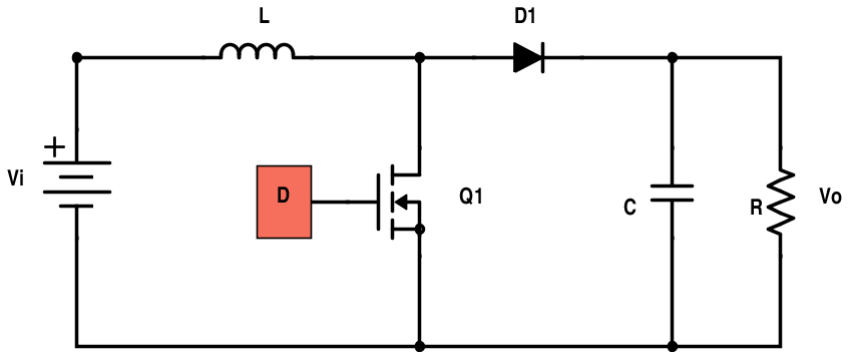

Figure 2.3: Basic construction of a boost converter.

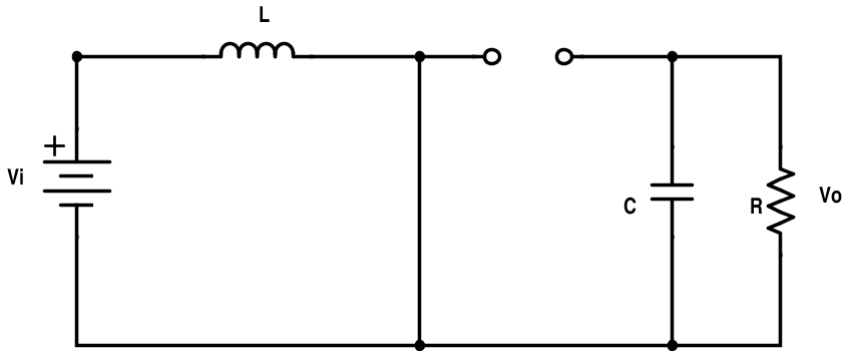

Figure 2.4: Equivalent circuit of the ON state boost converter.

The inductor current classifies the mode of operation either continuous or discontinuous mode of operation. In continuous inductor current mode, current

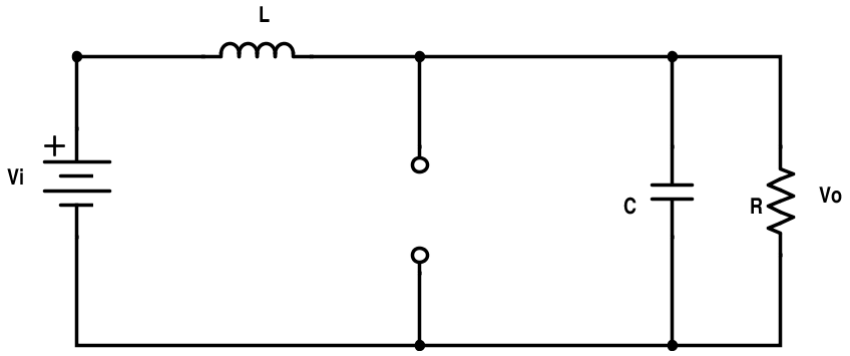

Figure 2.5: Equivalent circuit of the OFF state boost converter.

flows continuously in the inductor during the switching cycle in steady-state operation. Figure 2.6 shows the inductor current in continuous mode of operation, where I_L and I_O represent the inductor and output current respectively. V_Q and V_O indicate the trigger and output voltages respectively. T_{ON} and T_{OFF} are the ON and OFF times and $T_S = T_{ON} + T_{OFF}$. In discontinuous inductor current mode shown in figure 2.7, inductor current reaches zero during the switching cycle, where I_D represents the diode current. It is desirable for a power stage to stay in only one mode over its expected operating conditions because the power stage frequency response changes significantly between the two modes of operation [78].

2.2.1 Small Signal Model of DC-DC Boost Converter

The averaged model of a DC-DC boost converter is obtained by averaging the sets of differential equations that describe the mode of operation [79, 73]. For a boost converter operating in continuous current mode, the first state is when the transistor is ON. The state equations that describe the operation can be presented as follows:

$$\frac{di_L}{dt} = \frac{V_{in}}{L}, \tag{2.2.1}$$

$$\frac{dv_c}{dt} = -\frac{V_c}{RC}. \tag{2.2.2}$$

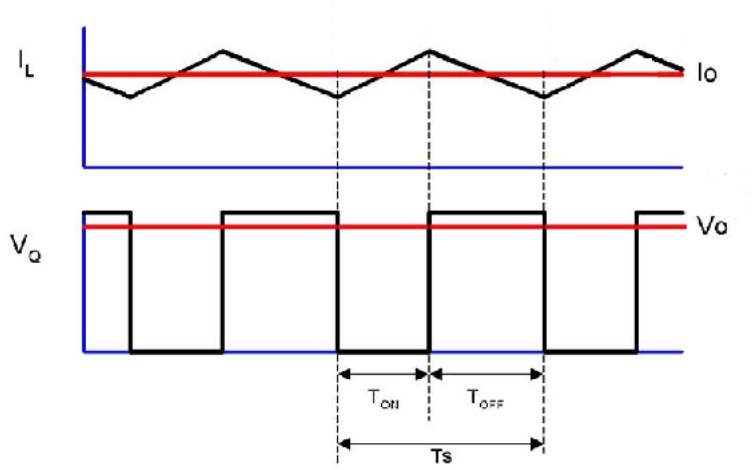

Figure 2.6: Inductor current and voltage in continuous mode of operation.

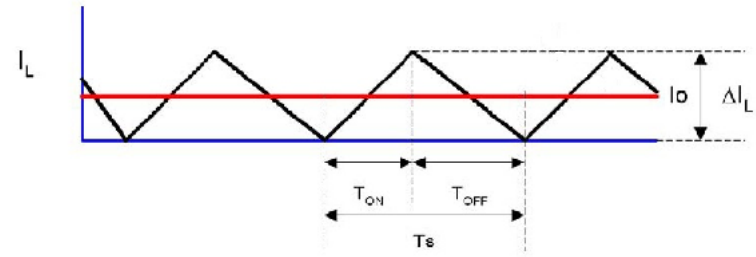

Figure 2.7: Inductor current in discontinuous mode of operation.

When the transistor is OFF, which is the second state, and the diode is forward biased. The state equations that describe the operation can be shown as follows [79]:

$$\frac{di_L}{dt} = \frac{V_{in} - V_c}{L}, \tag{2.2.3}$$

$$\frac{dv_c}{dt} = \frac{I_L}{C} - \frac{V_c}{RC}. \tag{2.2.4}$$

By averaging the state equations for the ON and OFF states, the duty cycle ratio D is introduced. The averaged state equations are as follows:

$$\frac{dI_L}{dt} = \frac{V_{in} - (1-D)V_c}{L}, \tag{2.2.5}$$

$$\frac{dV_c}{dt} = \frac{(1-D)I_L}{C} - \frac{V_c}{RC}. \tag{2.2.6}$$

By replacing the control parameters that are the input and state variables, with a dc steady-state value and a small time-varying component we get:

$$\frac{d(I_L + \tilde{i_L})}{dt} = \frac{V_{in} + \tilde{v_{in}} - (1-(D+\tilde{d}))(V_c + \tilde{v_c})}{L}, \tag{2.2.7}$$

$$\frac{d(V_c + \tilde{v_c})}{dt} = \frac{(1-(D+\tilde{d}))(I_L + \tilde{i_L})}{C} - \frac{(V_c + \tilde{v_c})}{RC}. \tag{2.2.8}$$

By neglecting the product of the DC steady state value and the small signal value, the state equations can be written in terms of the small signal values as follows:

$$\frac{d\tilde{i_L}}{dt} = \frac{\tilde{d}V_c + \tilde{v_{in}} - (1-D)\tilde{v_c}}{L}, \tag{2.2.9}$$

$$\frac{d\tilde{v_c}}{dt} = \frac{(1-D)\tilde{i_L} - \tilde{d}I_L}{C} - \frac{\tilde{v_c}}{RC}. \tag{2.2.10}$$

The state feedback system block diagram of the linearised model was built using the above equation and shown in figure 2.8.

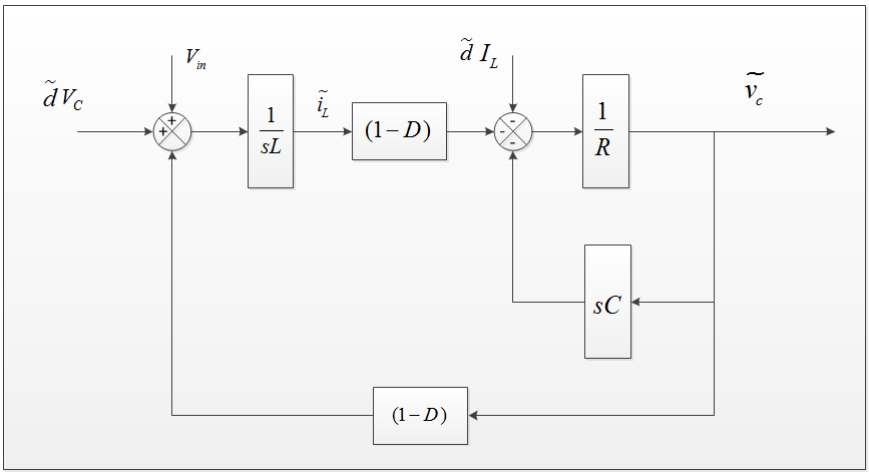

Figure 2.8: Linearised state feedback block diagram.

By simplifying the block diagram using Mason's rule, the transfer functions of the linearised boost converter model can be presented as follows [80, 81]:

$$\frac{\tilde{v_c}}{\tilde{d}} = \frac{(1-D)V_c - LI_L s}{LCs^2 + \frac{L}{R}s + (1-D)^2}, \tag{2.2.11}$$

$$\frac{\tilde{I_L}}{\tilde{d}} = \frac{(V_c C s + 2(1-D)I_L}{LCs^2 + \frac{L}{R}s + (1-D)^2}, \tag{2.2.12}$$

$$\frac{\tilde{v_c}}{\tilde{I_L}} = \frac{(1-D)V_c - LI_L s}{(V_c C s + 2(1-D)I_L}. \tag{2.2.13}$$

2.3 Classical PI controller

Proportional and Integral controllers (PI) are commonly used in control applications since they are easy to design, implement and tune. However, in WPGS classical PI controllers might not be the desired control strategy as it becomes difficult to handle uncertainties in non linear environments. So that the achievement of efficient and robust operations can not guaranteed. Generally, the idea of PI controller is to regulate the error between the measured input and the desired output. This error along with its integral provide a signal for the controller action with respect to time.

In this application PI control strategy has been implemented to investigate the system dynamics and to compare them with advanced control strategies. In WPGS application, the PI controller has been employed to PMSG after removing the cross-coupling between the d-axis and q-axis circuits. The linear model after adding the decoupling voltages, which remove the cross-coupling to improve the system dynamic performance, to the system can be shown in (2.1.29) and (2.1.30). The structure of the PI controller can be shown as follows [82]:

$$G(s) = k_p + \frac{k_i}{s}, \tag{2.3.1}$$

where k_p and k_i are the proportional and integral gains respectively. The PI controller has been implemented to the PMSG in such a way that the d-axis and q-axis currents are compared with d-axis and q-axis reference currents. The errors are regulated using PI controllers to generate d-axis and q-axis voltages which are transformed into pulse width modulation (PWM) signal to drive

the DC-DC converter switch. The reference q-axis current is generated from the speed control loop. The open loop transfer functions of the mechanical speed (G_m), the d-axis (G_d) and q-axis (G_q) can be obtained from the PMSG linearised model as the followings [73]:

$$G_m(s) = \frac{1}{B + Js}, \tag{2.3.2}$$

$$G_d(s) = \frac{1}{R_s + L_d s}, \tag{2.3.3}$$

$$G_q(s) = \frac{1}{R_s + L_q s}. \tag{2.3.4}$$

By multiplying (2.3.1) to (2.3.2), (2.3.3) and (2.3.4) The closed loop transfer function of the speed control (H_m) is given by (2.3.5). Where the closed loop transfer functions of the d-axis (H_d) and q-axis (H_q) currents control are given by (2.3.6) and (2.3.7) respectively [73].

$$H_m(s) = \frac{k_{pm}s + k_{im}}{Js^2 + (k_{pm} + B)s + k_{im}}, \tag{2.3.5}$$

$$H_d(s) = \frac{k_{pd}s + k_{id}}{L_d s^2 + (k_{pd} + R_s)s + k_{id}}, \tag{2.3.6}$$

$$H_q(s) = \frac{k_{pq}s + k_{iq}}{L_d s^2 + (k_{pq} + R_s)s + k_{iq}}. \tag{2.3.7}$$

The block diagram of the linearised model of a PMSG with PI speed and current controllers are shown in Figure 2.9. It can be shown in the figure that the decoupling voltages have been add to remove the cross coupling between the d-axis and q-axis currents control loops. Tuning of the speed and current controller's gains have been done manually. The manual PI tuning procedure can be described in the following way. Step one is to set all gains to zero. Then, increase the proportional gain (k_p) until the output oscillates around the set

point. After that, set the integral gain (k_i) until the system becomes nearly stable. Finally, fine the k_p until the system becomes stable and the desired output achieved.

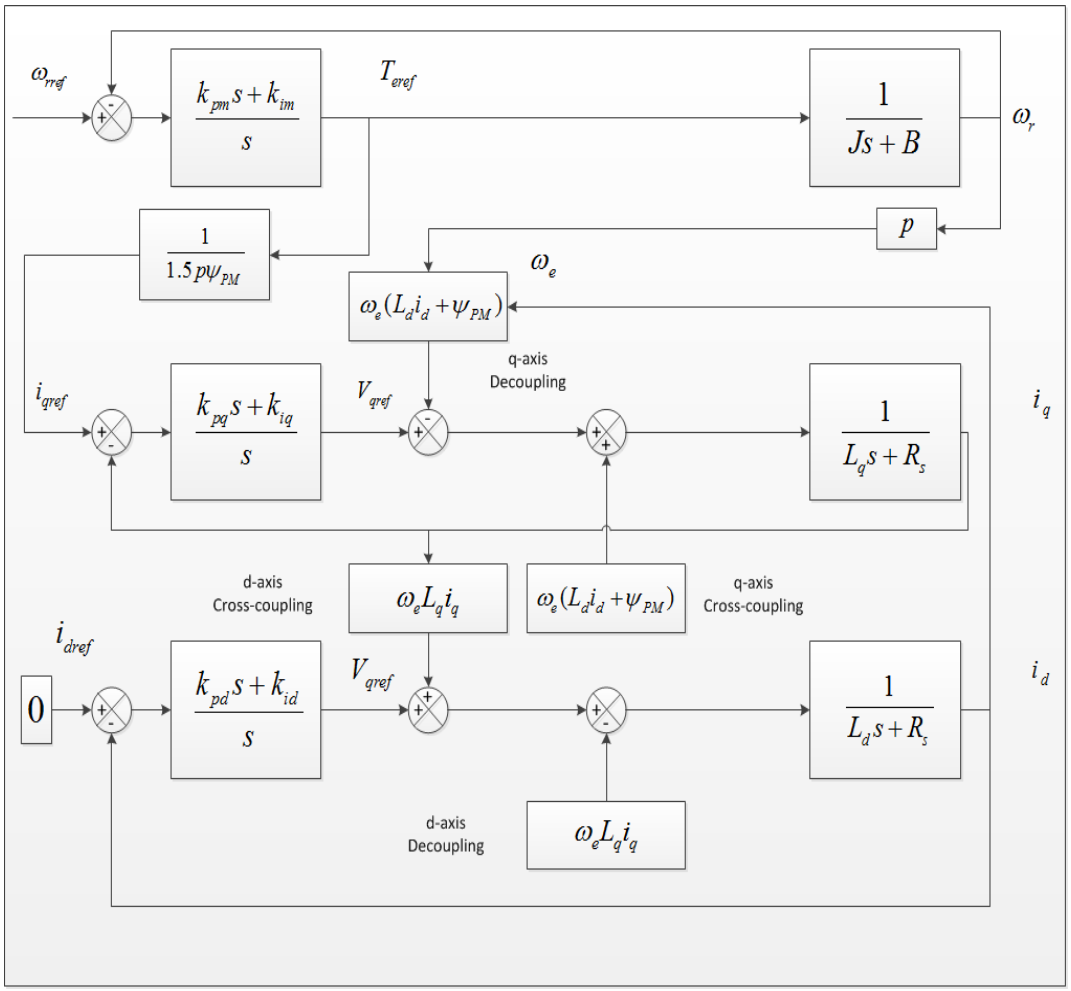

Figure 2.9: Block diagram of the linearised model of a PMSG with PI speed and current controllers.

2.4 Simulation Results and Analysis

The dynamic performance of the PMSG-based WPGS has been investigated by simulations using classical PI controller. The WPGS consist of PMSG, AC-

DC uncontrolled rectifier, DC-DC boost converter and a stand alone DC load. The WPGS has been simulated at low and rated speeds $8m/s$ and $10m/s$ respectively. The values for the wind speed have been chosen to match the normal operation values of wind speed and to analyse the WPGS during transients [73]. It is worth noting that the MPPT operation achieved when TSR is 0.82 and maximum energy conversion occurs when power coefficient is 0.22. Simulation results shows overshoot errors in the rotor speed. Figure 2.10 illustrates the speed performance of the PMSG using classical PI controller. The transient errors are clearly shown in the figure especially at rated wind speed, nevertheless, the MPPT operations have been achieved. Figures 2.11 and 2.12 show the power coefficient and the TSR respectively. It can be noted from the C_p analysis that the power loss during transients is high and the C_p is about 0.216 which is below the optimum value.

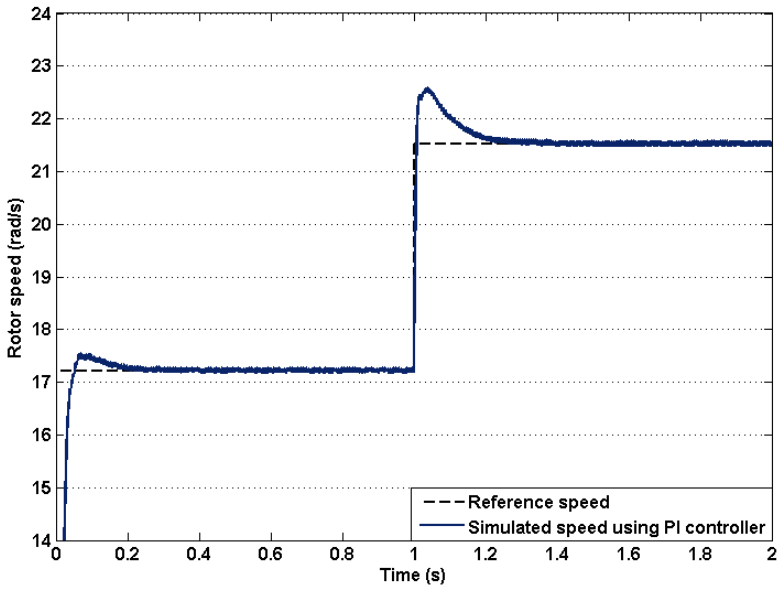

Figure 2.10: Simulated speed response of PMSG using classical PI controller.

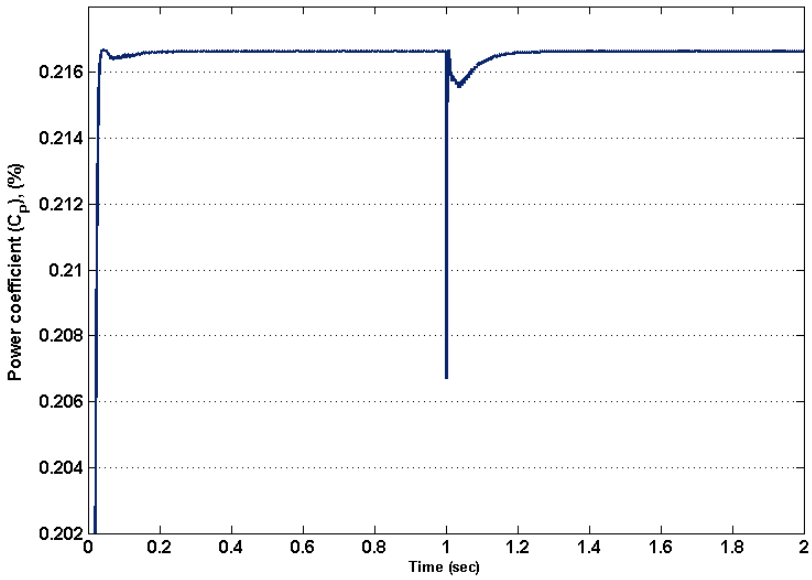

Figure 2.11: Simulation analysis of the power coefficient of WPGS.

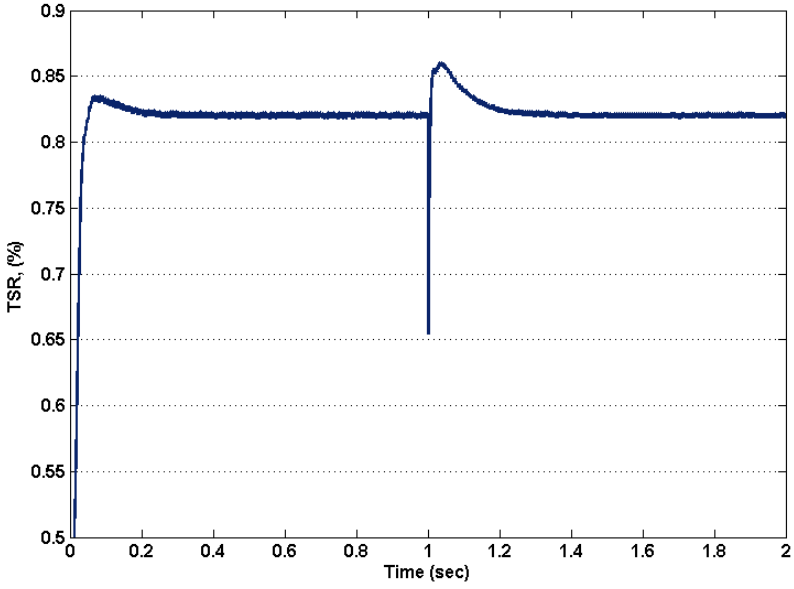

Figure 2.12: Simulation analysis of TSR of WPGS.

2.5 Conclusion

In this chapter the PMSG-based WPGS has been modeled. The power in the wind has been studied and the PMSG has been presented in the *abc* stationary reference frame. The electrical model has been discussed in both $\alpha - \beta$ reference frame and in $d - q$ rotating reference frame. The mechanical model of the PMSG has been studied and the linearised PMSG model has been illustrated. In addition, the classical control of PMSG-based WPGS has been discussed. The dynamic performance of the PMSG-based WPGS has been simulated and analysed using classical control. The overshoots appear in the speed performance and the power coefficient analysis indicates high loss of power. From the obtained results, it is strongly recommended to use more advanced control system to improve the dynamic performance and the energy conversion ratio of the WPGS.

Chapter 3

Maximum Power Point Tracking for Wind Power Generation System Using Sliding Mode Control

3.1 Introduction

The fast growing of wind power industry makes the research area of WPGS control more attractive to engineers and researchers from different backgrounds. According to the European Wind Energy Association, the wind energy installed in the EU is 24% of the total energy installed in the EU during 2011 [83]. For a small-scale WPGS, a permanent magnet synchronous generator (PMSG) has clear advantages over other types of electrical generator, such as a high torque to volume and inertia ratio, a high density of air-gap flux and it does not require an external DC supply for excitation windings [32, 84].

The accuracy of a PMSG model has a direct effect on its controller design. In [84], a particle swarm optimisation algorithm was proposed to identify

PMSG parameter variations during real operation conditions. It is known that the amount of extracted power from wind is limited, therefore it is necessary to employ a MPPT algorithm to control WPGS.

In this chapter, a first order SMC has been implemented to the small-scale WPGS as the simple design and implementation are targets to achieve. Adaptive gains have been proposed to overcome the drawbacks of first order SMC during wind speed variations. By introducing the adaptive gain to simple structured first order SMC, the steady states errors is eliminated and the uncertainty of the state variables are compensated. The adaptive gain can be a function of any measured variable, which is selected to be a function of wind speed in this research.

3.2 Sliding Mode Control Theory

Starting from late 1970s and continuing today, sliding mode control has received many attentions, since it has the advantages of quick response and robustness. SMC is a variable structure control strategy based on the feedback and high frequency switching control [28]. Moreover, it is insensitive to system parameter changes, disturbance and load variations [29]. The design of SMC consists of two main stages. The first stage is to achieve the design of a stable sliding surface and the second stage aims to obtain an optimum design of a control law, which forces system operating points to reach a predetermined surface in finite time [85].

3.2.1 Sliding Surface

A sliding surface is defined as the boundary that a controller forces operation points to lie on. The derivation of a sliding surface plays an important role

in obtaining an optimum design and it can be represented as follows [86, 87]:

$$s(x) = (\frac{d}{dt} + \gamma)^{n-1} e, \tag{3.2.1}$$

$$e = x_{ref} - x, \tag{3.2.2}$$

where s is the sliding surface and n is the relative degree, which is the number of differentiation until the control indices appear. The value for n can be determined from the control equation. For first order SMC n is equal to 1. γ is a positive constant matrix and e is an error between a reference value (x_{ref}) and a controlled variable (x).

3.2.2 Condition of Convergence

The main objective of SMC is to ensure the achievement of operation points to approach a predetermined sliding boundary in finite time from an arbitrary initial condition. This condition occurs when the signs of $s(x)$ and $\dot{s}(x)$ are opposite and the following conditions are satisfied [85].

$$\lim_{s \to 0_+} \dot{s} < 0, \tag{3.2.3}$$

$$\lim_{s \to 0_-} \dot{s} > 0. \tag{3.2.4}$$

By satisfying the two conditions the convergence of the operating point to the sliding surface is defined by the Lyapunov equation as the following [88]:

$$s.\dot{s} \prec 0. \tag{3.2.5}$$

3.2.3 Controller Design

The structure of SMC includes two parts, i.e. one is concerned with the exact linearisation and the second part is to stabilise the controller. To analyse the motion during the sliding mode, there is a widely accepted approach which is called equivalent control. In this approach, the discontinuous control, which

makes the sliding surface $s(x)$ approach 0, is replaced by an equivalent control. This equivalent control is obtained by setting $\dot{s}(x) = 0$ for the investigated system [85]. The structure of such a controller can be expressed as:

$$u = u_{eq} + u_n, \tag{3.2.6}$$

where u_{eq} is the equivalent control element and it is calculated along the sliding mode as below, where K represents a positive constant.

$$\dot{s}(x) = 0, \tag{3.2.7}$$

$$u_n = -Ksgn(s), \qquad sgn(s) = \begin{cases} 1, & s > 0 \\ 0, & s = 0. \\ -1, & s < 0 \end{cases} \tag{3.2.8}$$

3.3 Direct Speed Control Using Sliding Mode Control

3.3.1 Speed Controller Design

A speed controller is used in order to achieve a reference value of (i_q), which is the torque component of the current, consequently a maximum torque can be obtained. The mechanical speed error is defined as the difference between the actual mechanical speed of PMSG, which is expressed in (2.1.26), and the reference speed ω_{rref}, which is generated from a MPPT controller. Therefore, the mechanical speed error is expressed as below:

$$e = \omega_{rref} - \omega_r. \tag{3.3.1}$$

For $n = 1$, the sliding surface can be obtained from equation (3.2.1) as the following:

$$s(\omega_r) = e, \tag{3.3.2}$$

$$\dot{s}(\omega_r) = \dot{\omega}_{rref} - \frac{1}{J}T_m + \frac{1}{J}T_e + \frac{B}{J}\omega_r, \tag{3.3.3}$$

$$\dot{s}(\omega_r) = \dot{\omega}_{rref} - \frac{1}{J}T_m + \frac{1.5p\psi_{PM}}{J}i_q + \frac{B}{J}\omega_r, \tag{3.3.4}$$

$$u_{eq} = i_q^{eq} = \frac{J}{1.5p\lambda_{PM}}(\frac{1}{J}T_m - \dot{\omega}_{rref} - \frac{B}{J}\omega_r). \tag{3.3.5}$$

Based on equations (3.2.6) and (3.2.8), the proposed speed controller is derived as equation (3.3.6), where K_ω is a positive constant of the speed controller which is determined in subsection 3.3.4.

$$u = \frac{J}{1.5p\lambda_{PM}}(\frac{1}{J}T_m - \dot{\omega}_{rref} - \frac{B}{J}\omega_r) - K_\omega sgn(e). \tag{3.3.6}$$

3.3.2 Direct Current Controller Design

To implement the Field Orientated Control (FOC) [89], the direct current or the d-axis current is set to zero. So, the d-axis current error is the difference between the actual d-axis current, which is illustrated in (2.1.24) and zero. Therefore, the d-axis current error is expressed as the following:

$$e = i_{dref} - i_d \tag{3.3.7}$$

$$i_{dref} = 0. \tag{3.3.8}$$

For $n = 1$, the sliding surface can be obtained from equation (3.2.1) as below:

$$s(i_d) = e, \tag{3.3.9}$$

$$\frac{di_d}{dt} = \frac{1}{L_d}(V_d - R_a i_d + L_d\omega_e i_q), \tag{3.3.10}$$

$$\dot{s}(i_d) = \dot{i}_{dref} - \frac{V_d}{L_d} + \frac{R_a}{L_d}i_d - \omega_e i_q, \tag{3.3.11}$$

$$u_{eq} = V_d^{eq} = L_d(\dot{i}_{dref} + \frac{R_a}{L_d}i_d - \omega_e i_q). \tag{3.3.12}$$

From equations (3.2.6) and (3.2.8), the proposed direct current controller design is shown in equation (3.3.13), where K_d is a positive constant of the d-axis current controller.

$$u = L_d(\dot{i}_{drref} + \frac{R_a}{L_d}i_d - \omega_e i_q) - K_d sgn(e). \tag{3.3.13}$$

3.3.3 Quadrature Current Controller Design

The quadrature current controller is used in order to obtain a q-axis reference voltage. The reference quadrature current, which is generated from the speed controller, is compared to the actual q-axis current of the PMSG, which is shown in (2.1.25), to obtain the q-axis current error. Therefor, the q-axis current error is expressed as follows:

$$e = i_{qref} - i_q. \tag{3.3.14}$$

For $n = 1$, the sliding surface can be obtained from equation (3.2.1) as follows:

$$s(i_q) = e \tag{3.3.15}$$

$$\frac{di_q}{dt} = \frac{1}{L_q}(V_q - R_a i_q - L_q \omega_e i_d - \omega_e \psi_{PM}), \tag{3.3.16}$$

$$\dot{s}(i_q) = \dot{i}_{qref} - \frac{V_q}{L_q} + \frac{R_a}{L_q} i_q + \omega_e i_d + \omega_e \frac{\psi_{PM}}{L_q}, \tag{3.3.17}$$

$$u_{eq} = V_q^{eq} = L_q(\dot{i}_{qref} + \frac{R_a}{L_q} i_q + \omega_e i_d + \omega_e \frac{\psi_{PM}}{L_q}), \tag{3.3.18}$$

Based on equations (3.2.6) and (3.2.8), the proposed direct current controller design is derived as equation (3.3.19), where K_q represents the positive constant for the q-axis current controller.

$$u = L_q(\dot{i}_{qref} + \frac{R_s}{L_q} i_q + \omega_e i_d + \omega_e \frac{\psi_{PM}}{L_q}) - K_q sgn(e). \tag{3.3.19}$$

Finally, the values of the d-axis and q-axis voltages are used in order to generate a PWM control signal for the DC-DC boost converter‘.

3.3.4 Controller Stability

The stability of a sliding mode controller can be verified by the Lyapunove equation. For the speed controller to be stable, K_ω should be selected as a positive constant and must meet the following condition [90].

$$\left[\frac{J}{1.5p\lambda_{PM}}(\frac{1}{J}T_m - \dot{\omega}_{rref} - \frac{B}{J}\omega_r)\right] < K_\omega. \tag{3.3.20}$$

The tuning of K_ω can be performed by selecting a positive value, then the value is increased until it reaches its optimum value, at which the actual speed reaches the reference speed in finite time. It should be noted that K_ω must be large enough to ensure the stability and MPP achievement under the worst case. This case is when $\omega_r = 0$, as the speed error is at its maximum and equal to ω_{rref} and K should be:

$$\left[\frac{J}{1.5p\lambda_{PM}}(\frac{1}{J}T_m - \dot{\omega}_{rref} - \frac{B}{J}\omega_r)\right] < K_\omega, \tag{3.3.21}$$

$$\frac{T_m\omega_{rref}}{1.5p\lambda_{PM}} < K_\omega. \tag{3.3.22}$$

Similarly the constant gain for the d-axis and q-axis current controllers must meet the following condition $0 < K_d$. The constant gain for the q-axis current controller can be chosen to be a function of wind speed. This is to maintain robustness and to eliminate steady-state errors. By simulating the system as a linear function, which is shown in equation (3.3.23), with respect to wind speeds gives a good response and the stability condition is achieved. For the worst case analysis, the condition for K_q is as below, where Y and Z are system dependent constants. The value of K_q, which is the sliding mode control gain, ensures the stability of the WPGS by allowing the SMC to compensate the uncertainty during rapid wind variations and eliminating the steady-states errors.

$$YV_w + Z = K_q, \qquad 0 < K_q. \tag{3.3.23}$$

The results from the stability analysis shows that the proposed controllers are stable under transient conditions and the controlled variables can reach the desired sliding surface.

3.4 Indirect Speed Control Using Sliding Mode Control

The main advantage of a sensorless indirect speed controller is to overcome the disadvantages of using mechanical sensors in terms of cost and reliability [91]. Practically, a controller has been designed in such a way that a reference q-axis current is generated at an optimum level according to its maximum power point for each wind speed. Furthermore, the generated optimum q-axis current is compared with the actual q-axis current and control actions are taken to increase or decrease rotation speeds. The d-axis current is compared with zero and the mechanical speed of the generator is controlled indirectly. This strategy benefits from having only two control loops instead of three loops used in the direct speed control as well as the simplicity of its design. Since the rotor position angle is required to obtain a dq model for the PMSG. In this controller, it is obtained using a back-EMF observer.

3.4.1 Controller Design

Based on the power-speed curve shown in Fig. 2.1 the maximum power point occurs when TSR is 0.82. By solving (3.4.2) for TSR, the power coefficient has a maximum value of 0.22. Then the maximum mechanical torque can be calculated for each wind speed from equation (3.4.3) and the optimum speed can be calculated from equation (3.4.1). The developed electrical torque is then calculated using equation (3.4.4). Hence, for each wind speed the optimum torque can be obtained, where *opt* represents the optimum condition.

$$\omega_{r-opt} = \frac{\lambda_{opt} V_w}{R_a}, \tag{3.4.1}$$

$$C_{p-opt} = -0.13\lambda_{opt}^3 - 012\lambda_{opt}^2 + 0.45\lambda_{opt}, \tag{3.4.2}$$

$$T_{m-opt} = \frac{1}{2}\rho C_{p-opt} A V_w^2, \tag{3.4.3}$$

$$T_{e-opt} = T_{m-opt} - J\frac{d\omega_{r-opt}}{dt} - B\omega_{r-opt}, \tag{3.4.4}$$

$$T_e = 1.5p(\psi_{PM} i_q + (L_d - L_q) i_d i_q). \tag{3.4.5}$$

By implementing FOC, the torque of PMSG can be controlled. The implementation of FOC to a PMSG requires two assumptions:

1 . The torque component should be aligned to the q-axis.

2 . The flux component should be aligned with the d-axis.

The torque component of the current (i_q) and the torque are directly proportional. The linear relationship can be achieved only when the rotor flux amplitude is kept as a constant. The d-axis current is set to zero, then the electro-mechanical torque can be directly controlled via the q-axis current from equation (3.4.6). Hence, the optimum q-axis current can be generated from (3.4.7).

$$T_e = 1.5p(\psi_{PM} i_q), \tag{3.4.6}$$

$$i_{q-opt} = \frac{T_{e-opt}}{1.5p(\psi_{PM})}. \tag{3.4.7}$$

The speed and the rotor position have been estimated using back-EMF observer.

3.4.2 Back-EMF Observer

When implementing a dq-axis model, an exact value of a rotor position angle is required. Many techniques in estimating the rotor position have been reported [92, 93]. In this section, a back-EMF observer has been used to estimate rotor positions, since the back-EMF is a function of the rotating speed. The sinusoidal back-EMF equation in the $\alpha - \beta$ co-ordinate can be presented as follows [73]:

$$e_\alpha = L\frac{d}{dt} i_\alpha + R_a i_\alpha + V_\alpha, \tag{3.4.8}$$

$$e_\beta = L\frac{d}{dt}i_\beta + R_a i_\beta + V_\beta, \tag{3.4.9}$$

where $e_{\alpha\beta}$, $V_{\alpha\beta}$ and $i_{\alpha\beta}$ are the back-EMF, voltage and current of a PMSG in the $\alpha - \beta$ co-ordinate and L is the PMSG inductance. The rotor position θ can be estimated from (3.4.8) and (3.4.9) as the following [94]:

$$\hat{\theta} = \tan^{-1}\left(\frac{e_\alpha}{e_\beta}\right). \tag{3.4.10}$$

3.5 Simulation Results and Analysis

The control diagrams of the two developed MPPT controllers are shown in Figs. 3.1 and 3.2 respectively. For both the controllers, the PMSG model in the $d - q$ rotating reference frame is obtained. A wind speed measurement is required for obtaining the MPPT algorithm. The PMSG voltage and current are measured and the rotor position is obtained. For the direct speed controller, the rotor position is calculated using the speed measurement, but for the indirect speed controller the rotor position is estimated.

The actual speed is compared with the reference speed and the controller action is taken by changing the duty ratio of the DC-DC boost converter. In the indirect speed controller, the q-axis current is compared with an optimum q-axis current obtained from a MPPT controller. Similarly a control action is to increase or decrease the duty ratio of the converter switch based on the sign of error. It is worth to mention that the sliding mode gain is set to be high so that a quick and accurate tracking performance are guaranteed when a fault happens [58].

In this research, the wind turbine is modeled as a vertical axial (VAWT) unit and the generator is a PMSG. The WPGS model has been simulated under variable wind speeds. The wind speed function starts at 8 m/s then it goes to 10 m/s. The values for the wind speed have been chosen to match the normal operation values of wind speed and to analyse the WPGS during

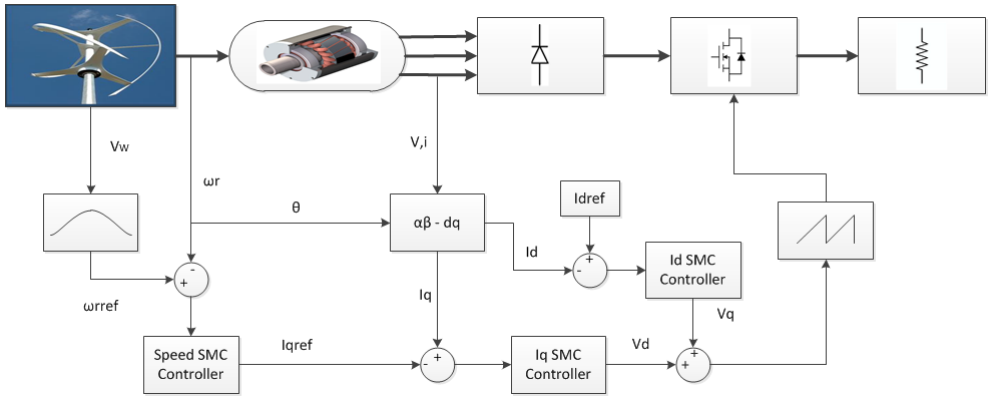

Figure 3.1: Control diagram of direct speed controller using SMC

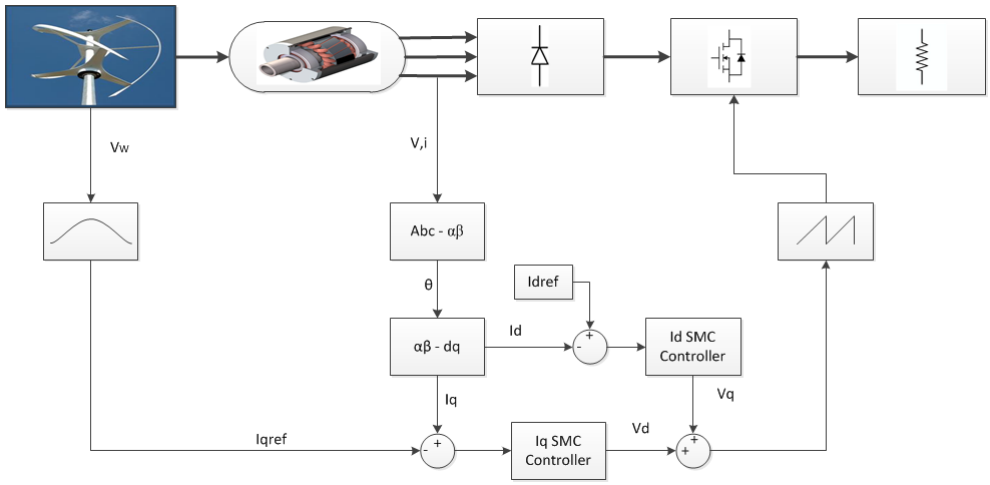

Figure 3.2: Control diagram of indirect speed controller using SMC

transients [73]. The parameters of the PMSG and the VAWT employed in this simulation are illustrated in Table 3.1. The parameter values have been obtained from nameplate date and lab test [73].

For the developed direct speed controller, the constant gain is set to be adaptive in order to achieve a better response and to reduce DC offset errors. Also, the gain value should be high to guarantee the fast and accurate performance when fault occur. Figure 3.3 shows the mechanical speed of the PMSG tracks the reference speed obtained from MPPT to ensure the maximum power point operation. It is clearly shown that the PMSG speed tracks the reference

Table 3.1: Actual Parameters of the WPGS

Parameters	Value
VAWT	
Type	Savonius VAWT
Radius of the blade	0.381 m
Rated Power	165 W
Maximum Power Coefficient	0.22
Optimal TSR	0.82
PMSG	
Type	GL-PMG500A
Rated Power	500 W
Stator Winding Resistance	0.35 Ω
Moment of Inertia	0.066 $Kg.m^2$

speed closely. C_p is shown in Fig. 3.4 under variable wind speeds. The value of C_p is about 0.216 which is below the maximum. The three-phase PMSG line currents are shown in Fig. 3.5, where it clearly shows that the PMSG line currents vary at different speeds to ensure maximum power extraction. Furthermore, it is noticeable that the generated AC currents change smoothly during transients, which reduce switching power losses.

The developed indirect speed controller has been tested and simulated. Figure 3.6 illustrates the mechanical speed, which is controlled indirectly, tracking the optimum speed and a maximum power conversion is obtained. The dynamic performance of the PMSG-based WPGS has been improved by using SMC-II. The C_p is illustrated in Fig. 3.7. The difference in C_p between the two SMC controllers are not noticeable.

The performance of the SMC controllers have been compared with a PI controller, which is presented in Section 2.3 concerning mechanical speeds and

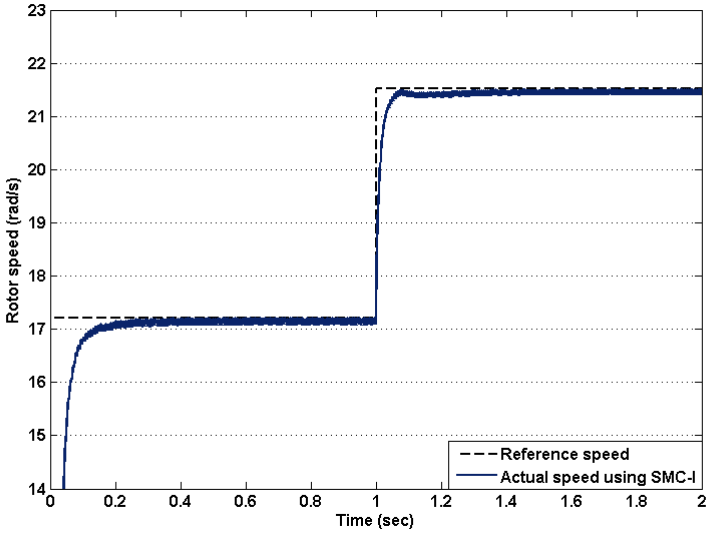

Figure 3.3: Actual speed tracking the reference speed of SMC-I (i).

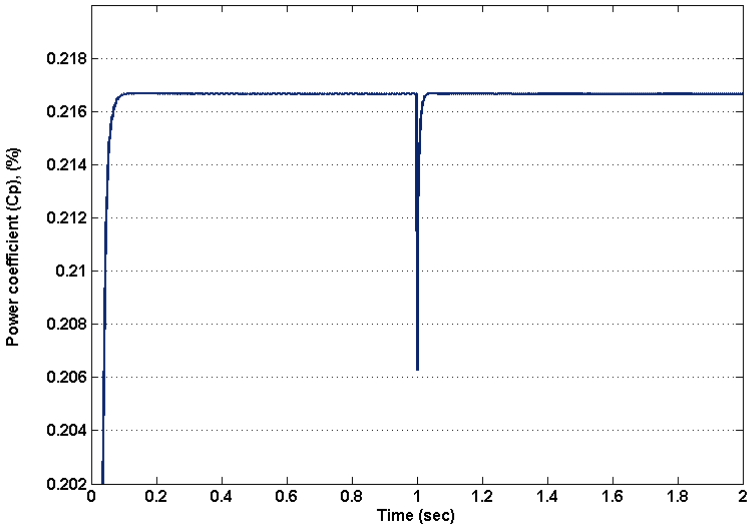

Figure 3.4: C_p under different wind speeds of SMC-I (i).

efficiency. The results are shown in Fig. 3.8. It is clear from the figure that there is no overshoot in the performance of the proposed controllers, while overshoot occurs in the speed performance of the PI controller. Also, the results obtained in Section 2.4 indicated a higher energy conversion ratio achieved

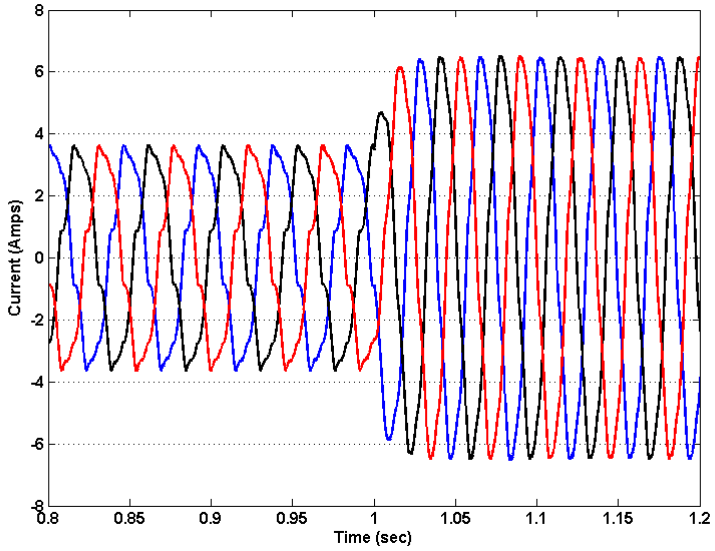

Figure 3.5: Three-phase line currents under wind speed variation of SMC-I (i).

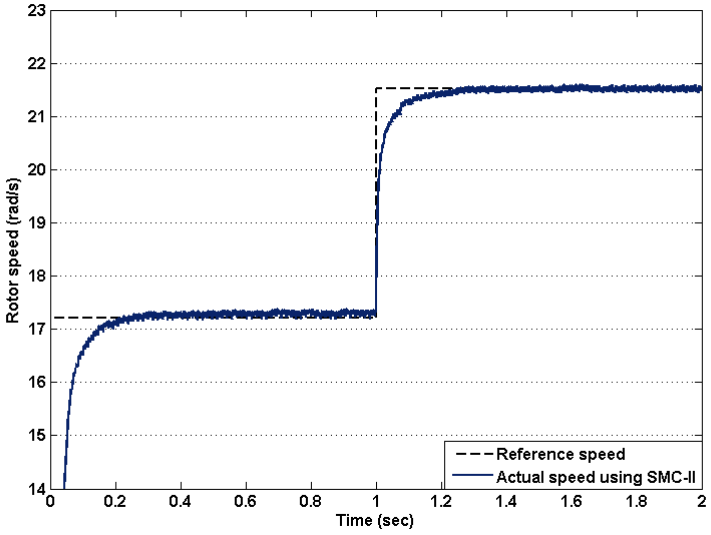

Figure 3.6: Actual speed tracking the optimum speed of SMC-II (ii).

when employing SMC to the control system of the WPGS. It can also be shown that the dynamic response is slower when implementing a classical PI control to the control system of the WPGS.

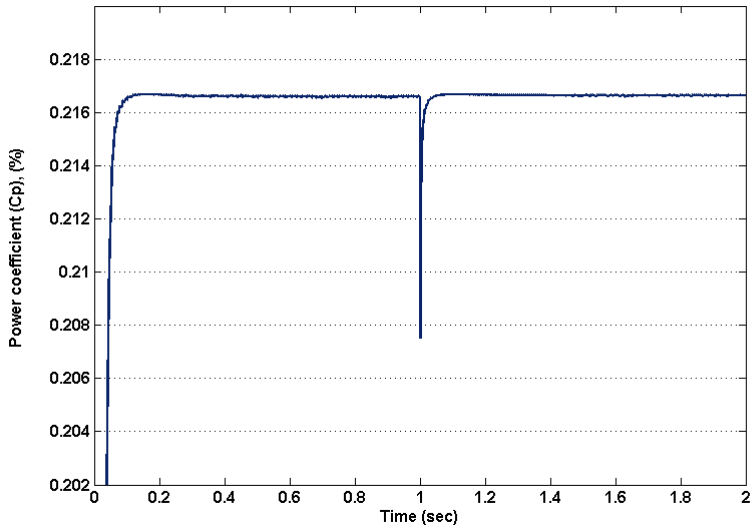

Figure 3.7: C_p under different wind speeds of SMC-II (ii).

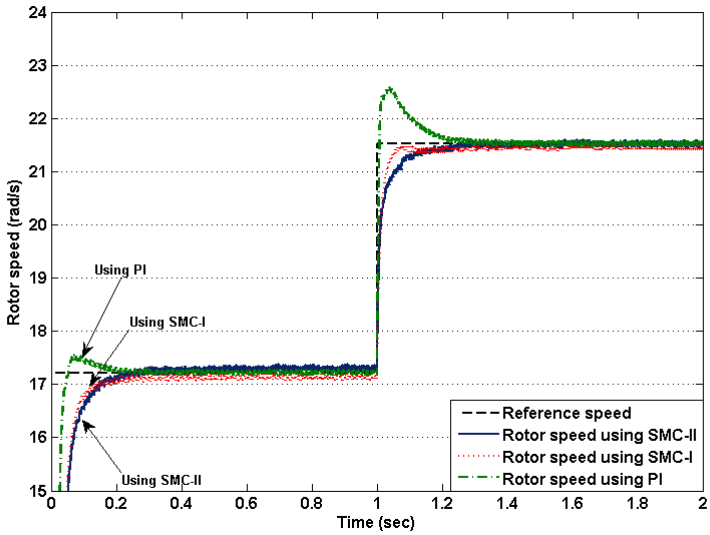

Figure 3.8: Comparison between the proposed SMC controllers and a PI controller.

3.6 Conclusion

In this chapter, a small-scale PMSG-based WPGS which is connected to a stand-alone DC load through a PWM controlled DC/DC converter has been

employed to investigate the dynamic responses of SMC controllers. Two controllers has been developed, simulated and tested based on SMC scheme. One of the controllers uses a direct speed controller, in which a mechanical speed sensor is present, while the other controller does not require a speed sensor and the speed is being controlled indirectly. The results for both the controllers demonstrate a satisfactory response and stable operations during transient and steady conditions. The comparison between the two controllers and a PI controller has been discussed. Moreover, it is noticeable that the speed response of the developed SMC controllers shows no overshoot, while when using the PI controller overshoot occurs. It can be concluded that the indirect speed controller using SMC gives satisfactory dynamic performance for a small-scale low-cost WPGS. Moreover, it can be deduced that using an adaptive gain for a SMC controller can improve the dynamic response of the system compared with that using a constant gain. Finally, it can be deduced that Lyapunov based controllers such as SMC can handle uncertainties better than PI controller in such non linear control environment.

Chapter 4

Maximum Power Point Tracking Controller for Wind Power Generation System Based on Residue Theorem

This chapter aims to introduce a new approach in wind power generation system control strategy by a development of a new soft control strategy using the mathematical residue theorem. This new control approach can improve the electrical power conversion ratio. Also the developed soft dynamic boundary control approach overcomes some major drawbacks of the commonly used control strategies, i.e. the weakening of feedback linearisation in handling uncertainties and the loosening of the ultimate robustness of SMC which occur when the discontinuity dynamics changes.

The control strategy has been implemented in different control techniques of a small-scale WPGS. In the first controller, it has been implemented and tested in the speed control loop of a permanent magnet synchronous generator to generate a reference q-axis current while both d-axis and q-axis current loops

are controlled by PI current controllers. For the second controller, it has been implemented to the speed control loop as well as the d-axis and q-axis current control loops. The idea of using the residue theorem is to set a soft dynamic boundary for controlled variables around a reference point, so that controlled variables lie on a point inside the boundary. The stability of the system has been ensured by following the Forward Euler method. In the third controller, the definition of the boundary has a different definition and the convergence of an operating point to the set point is ensured using an exponential function. Moreover, a wind speed estimation algorithm is provided and implemented to the proposed controllers to overcome the wind speed measurement issues. A comparison between sliding mode controller and the proposed controller is provided. Both simulation results and experimental verification are presented to validate the proposed approach in control strategy.

4.1 Introduction

Wind energy is growing fast in the word during the last few decades. According to the European Wind Energy Association, around one fourth of the installed renewable energy in Europe during the last two years is wind energy [83]. The amount of extracted power from wind depends on the wind and the control strategy of WPGS [95]. Wind turbines can be classified into two categories with respect to their operation speeds, i.e. constant speed turbines or variable speed turbines. For a small-scale application, it is preferred to use PMSG as directly driven. Also, it is recommended to use fixed pitch blades. For such systems the cost and maintenance are kept at minimum and the simplicity is achieved [96]. One objective of a WPGS controller is to reach the maximum possible power extraction from wind power by operating a wind turbine at its MPPT [52]. Another controller objective is to maintain the system stability. Several methods have been implemented in tracking the maximum

power point [97, 98]. The control of obtaining a MPPT during a high variation of wind speed, causes stress on the shaft and overshoots in the speed response [52]. For a PMSG, the output current is proportional to the electromagnetic torque and the rotation speed is proportional to the output voltage [99]. One reported method of implementing MPPT is approximation of the optimal current versus rotor speed characteristic. By measuring the output voltage of WPGS, the rotor speed can be calculated. The difference between the measured and estimated currents is used to control the duty cycle of a DC/DC converter [100, 101]. However, these methods require the knowledge of WPGS optimal characteristics, which is not accurate and varied with the rotor ageing [99].

Sliding mode control has been widely implemented in WPGS control due to its robustness and simple structure. Elimination of chattering effect, which is described as an oscillation in the output response with less than infinity frequency, is an area of concern when implementing SMC. Ideally, SMC generates a discontinuous control signal which switches at infinity frequency with restricted amplitude. The discontinuity dynamics of SM nature causes the chattering effect. This can be avoided by a slight change in the SM dynamics. However, it has been deduced in [62] that when the discontinuity dynamics changes the ultimate robustness and accuracy of the SM nature are partially lost. In addition, several approximation in switching elements and gain calculation can deteriorate the dynamic performance of the system [102]. In [103, 104], an artificial integrator was introduced so that the actual discontinuous control signal, when passed to the system became continuous in nature.

Wind power generation system is a complex nonlinear system which operates in noisy environments. Nonlinear feedback control based on differential geometric has received many attentions regardless the fact that it is still weak in handling uncertainties. Several approaches for feedback linearisation methods such as dynamic surface control have been developed to overcome the problem

[57]. Lyapunov-based control design techniques such as sliding mode control have a good ability to handle fast time varying and functional uncertainties and can replace the nonlinear feedback control in such environment.

The new control approach which is presented in this chapter, aims to achieve efficient control so that it can overcome and replace the followings;

i) The weakening of feedback linearisation in handling uncertainties.

ii) The loosening of the ultimate robustness of SMC which occur when the discontinuity dynamics changes.

iii) The steady-states error and chattering problems that appear in a sliding mode control scheme.

iv) The overshoot which appears with a PI controller.

Since SMC said to be a discontinuous control where the control signal of the proposed control strategy is continuous. The idea of using the residue theorem is to set a soft dynamic boundary for controlled variables around a reference point, so that controlled variables lie on a point inside the boundary. Three controllers have been proposed using residual controller. Two of them have the same boundary definition where the third controller has different definition of the speed boundary. For the two controllers and during transient, as a PMSG accelerating the generated control boundary decreases smoothly, since the generated control boundary depends on the difference between the actual and reference speeds. Then at steady state, the generated control boundary become nearly zero. For the third controller the boundary is selected to be the area from 0 to the reference speed. Also, a wind speed estimation algorithm is designed and implemented to provide a solution of the wind speed measurement issues.

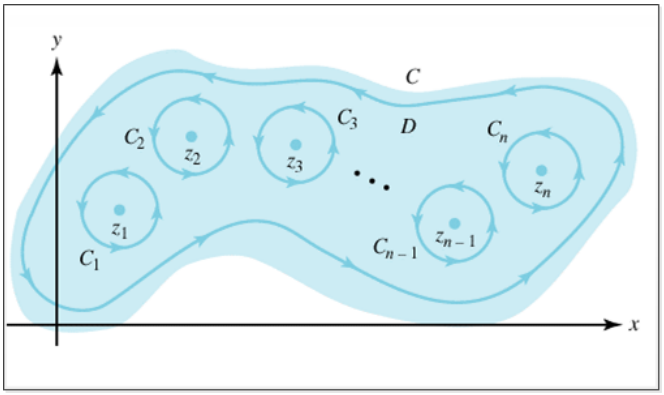

Figure 4.1: Illustration of the Cauchy's Residue Theorem [107].

4.2 Residue Theorem

The residue theorem is considered as one of the best tools to predict the area under a curve. The Cauchy Theorem stated that if a function is analytic on and in a closed contour C, then the integral over the closed contour is zero [105, 106].

Cauchy's Residue Theorem 1. *Let D be a simply connected domain, and let C be a simple closed positively oriented contour that lies in D. If $f(z)$ is analytic inside and on C, except at the points $z_1, z_2, ..., z_n$ that lie inside C [107]-[108], then*

$$\oint f(z)dz = 2\pi\iota \sum_{k=1}^{n} RES[f, z_k]. \tag{4.2.1}$$

The illustration of such a situation is shown in Fig. 4.1 [107], where ι is the complex representation, and the general form of the residue theorem can be expressed in equation (4.2.2).

$$RES\, f(x) = \frac{1}{2\pi\iota} \int_{-\infty}^{+\infty} f(x)\, dx. \tag{4.2.2}$$

The forward Euler method which is represented in equation (4.2.3), is implemented to ensure the convergence of the point to the reference point, so that

the stability of the system is maintained [109, 110].

$$\dot{y} \approx \frac{y(t+h) - y(t)}{h}, \tag{4.2.3}$$

where y is a controlled variable and h is a step size.

4.3 Development of MPPT Controllers Using Residue Theorem

4.3.1 Using Residual for speed Controller with PI current controllers

In this controller (Controller-I), a speed control loop has been designed using the residue theorem where the d-axis and q-axis current controllers are controlled using PI controllers. The speed boundary area is selected to be between a reference point plus the absolute value of the error and the reference point minus the absolute value of the error. The speed error (e) is the difference between the reference point and the actual measured point of speed. The implementation of equation (4.2.2) to the speed controller is done by assuming that at each point of time the speed lies in the boundary between the reference speed (ω_{rref}) plus error and the reference speed minus error. The rotor speed can be expressed as follows:

$$RES(\omega_r) = \frac{1}{2\pi\iota} \int_{\omega_{rref-e}}^{\omega_{rref+e}} \omega_r \, d\omega. \tag{4.3.1}$$

By solving the above integration, the definition of the controlled speed can be described as:

$$RES(\omega_r) = \mid \frac{\omega_{rref} e}{\pi} \mid . \tag{4.3.2}$$

The speed error is defined according to the forward Euler method to ensure the convergence of the speed to the reference speed which is shown in equation

(4.2.3).

$$\dot{e} = e + c, \tag{4.3.3}$$

$$e = \omega_{rref} - \omega_r. \tag{4.3.4}$$

By solving (4.3.4),

$$\dot{\omega}_{rref} - \dot{\omega}_r = \omega_{rref} - \omega_r + c. \tag{4.3.5}$$

Solving (4.3.5) with respect to the mechanical speed equation (2.1.26) to get the final design equation, which is used to generate the q-axis reference current. Then the design equation is presented in (4.3.6).

$$i_q = \frac{3}{2p\psi_{PM}}[T_m - B\omega_r - \frac{J}{\pi}\omega_{rref} - JK]. \tag{4.3.6}$$

Controller Stability Analysis

The stability of a controller is determined by implementing the forward Euler which ensures the convergence of the operating point to the boundary. The forward Euler is converge strongly when the function is said to be Lipschitz [111, 110]. Assume that wind speeds change from 8 m/s to 10 m/s then the reference speed, which is generated from a MPPT controller, changes from ω_{rref1} to ω_{rref2}. Hence the rate of change of the actual speed is as the following:

$$\dot{\omega}_r = \dot{\omega}_{rref} - \omega_{rref2} + \omega_{r1} - c. \tag{4.3.7}$$

It should be noted that the term $\dot{\omega}_{rref}$ has the highest influence in the controller decision. Furthermore, the change in the actual speed has the same sign of the change of the reference speed. The value of the constant c should ensure the convergence of the system and the stability and it must meet the following Lipschitz condition [112]:

$$c \leq \frac{|\dot{\omega}_r - \dot{\omega}_{rref}|}{|\omega_r - \omega_{rref}|}. \tag{4.3.8}$$

4.3.2 Using Residual Controller for Speed and Currents Loops

In this controller (Controller-II), the speed and dq-axis current controller are designed using the residue theorem. The boundaries are selected to be the reference value plus the error and the reference value minus the error. The linearised dq-axis equations and the final design equations are shown in (4.3.12) [73].

$$V_d = R_s I_d + L\frac{di_d}{dt}, \tag{4.3.9}$$

$$V_q = R_s I_q + L\frac{di_q}{dt}, \tag{4.3.10}$$

$$V_d = R_s I_d + LK, \tag{4.3.11}$$

$$V_q = R_s I_q + \frac{L\,e\,i_{qref}}{\pi} + LK. \tag{4.3.12}$$

Where K is a controller tuning constant which is manually tuned. Actually, an exact value of a rotor position angle is required in order to implement a dq-axis model. Many techniques in estimating the rotor position have been reported [92, 93]. In this controller, a back-EMF observer has been used to estimate the rotor position, since the back-EMF is a function of the rotating speed. The sinusoidal back-EMF equation in the $\alpha - \beta$ co-ordinate can be denoted as follows [73]:

$$e_\alpha = L\frac{d}{dt}i_\alpha + R_s i_\alpha + V_\alpha, \tag{4.3.13}$$

$$e_\beta = L\frac{d}{dt}i_\beta + R_s i_\beta + V_\beta, \tag{4.3.14}$$

where $e_{\alpha\beta}$, $V_{\alpha\beta}$ and $i_{\alpha\beta}$ are the back emf, voltage and current of a PMSG in the $\alpha - \beta$ co-ordinate and L is the PMSG inductance. The rotor position θ can be estimated from (4.3.13) and (4.3.14) as follows [94]:

$$\hat{\theta} = \tan^{-1}\left(\frac{e_\alpha}{e_\beta}\right). \tag{4.3.15}$$

The values of the d-axis and q-axis voltages are used in order to generate a control signal of a pulse width modulation (PWM). These voltages are normalized and compared with a triangular signal with an amplitude of 1 and a frequency of 20 kHz.

4.3.3 Using probability Residual Controllers

Another control approach has been proposed for the speed control loop using residue theorem. In this controller (Controller-III), the implementation of the residue theorem still exists but speed boundary has different definition. The boundary area has been defined between the positive and negative value of the reference speed. Mathematically, the speed boundary area can be double the positive area, which means the integration limits can be from 0 to absolute value of the reference speed. The PMSG mechanical equation can be expressed as follows:

$$\frac{d\omega_r}{dt} = \frac{1}{J}(T_m - T_e - B\omega_r). \tag{4.3.16}$$

In this proposed speed controller, the speed error (e_w), which is the difference between the reference speed and the actual measured rotating speed, is defined as the residue of the actual speed as bellow:

$$e_w = \omega_{rref} - \omega_r, \tag{4.3.17}$$

$$\dot{e_w} = RES(\dot{\omega_r}). \tag{4.3.18}$$

By solving the above equations and setting the integration limits as positive and negative reference speed, the controller design equations can be derived as the following:

$$\dot{e_w} = \frac{1}{2\pi\iota}\int_{-\omega_{rref}}^{\omega_{rref}} \omega_r \, d\omega, \tag{4.3.19}$$

$$\dot{\omega_r} = \sqrt{\frac{\dot{e_w}\omega_{rref}}{2\pi}}\iota, \tag{4.3.20}$$

$$i_{qref} = \frac{J}{1.5p\psi_{PM}}\sqrt{(\frac{B}{J}\omega_r - \frac{1}{J}T_m)^2 - \frac{\dot{e_w}\omega_{rref}}{2\pi}}. \quad (4.3.21)$$

Similarly, in this proposed speed controller the dq-axis current controller are controlled using PI controllers. The control sequence cab be summarised in the following way. The MPPT algorithm generates a maximum power for each measured wind speed which is divided by voltage obtained from the V_{dq} to generate a DC reference current. The generated DC current is compared with a measured output current. The difference between the reference DC current and the actual DC current is normalized using PI compensator then compared with a triangular signal which has an amplitude of 1 and a frequency of 20 kHz. This signal is used to fire the DC/DC converter switch.

Controller Stability Analysis

The stability of a controller is maintained by a introducing an exponential function of the error to ensures the convergence of the operating point to the predetermined speed boundary. The stabiliser term can be shown as follows:

$$Z\mathrm{e}^{-e_w}, \quad (4.3.22)$$

by introducing the stablising term to the speed controller loop equation (4.3.21), the final speed controller equation can be derived as follows:

$$i_{qref} = Z\mathrm{e}^{-e_w} - \frac{J}{1.5p\psi_{PM}}\sqrt{(\frac{B\omega_r - T_m}{J})^2 - \frac{\dot{e_w}\omega_{rref}}{2\pi}}. \quad (4.3.23)$$

4.3.4 Using Residual Controller with Estimated Reference Speed

One of the issues in WPGS control is the measurement of the wind speed. The accuracy of the wind speeds measurement can not be ensured using single anemometer [36]. Also, the data recorded using SCADA system contain noticeable deviations which influence in the power conversion efficiency [113].

In this controller the wind speed is estimated using MPPT algorithm and the reference speed is generated using the estimated data. The wind power model which is expressed in equations (2.1.2) and (2.1.4) can be solved for the wind speed and the (P_m) is assumed to be the output DC power (VI). The estimated wind speed can be shown as the following:

$$V_w = \frac{-D_{21}\omega_r^2 \pm \sqrt{D_{21}^2\omega_r^4 - 4D11\omega_r(D_{31}\omega_r^3 - VI)}}{2D_{11}\omega_r}. \tag{4.3.24}$$

where $D_{11} = 0.0960$, $D_{21} = -0.0098$ and $D_{31} = -0.0040$. The MPPT controller is implemented in the proposed controller-II which is presented in 4.3.2.

4.4 Simulation Results and Analysis

The control diagrams of the two developed MPPT controllers, i.e. controller-I and controller-II are shown in Figs. 4.2 and 4.3 respectively. For both the controllers, the d-axis and q-axis models are obtained and the measurement of wind speed is required. The PMSG voltage and current are measured as well as the rotor position. Figure 4.4 shows the control block diagram of the third proposed controller which is controller-III.

In this research, the wind turbine is modelled as a VAWT unit and the generator is a PMSG. The WPGS model has been simulated under variable wind speeds. The wind speed function starts at 8 m/s then it goes to 10 m/s. The parameters of the PMSG and the VAWT employed in this simulation are illustrated in Table 3.1.

The three controllers have been simulated using MATLAB/SIMULINK. Figure 4.5 shows the speed dynamic boundary of the system. It is clear from the Figure 4.5a, that the speed boundary is decreasing when the PMSG is accelerating. In addition, the integration effect makes the boundary limits changing in a soft manner. It can be noted with the illustration of Figure 4.5b that during transients, the dynamic boundary converges smoothly and

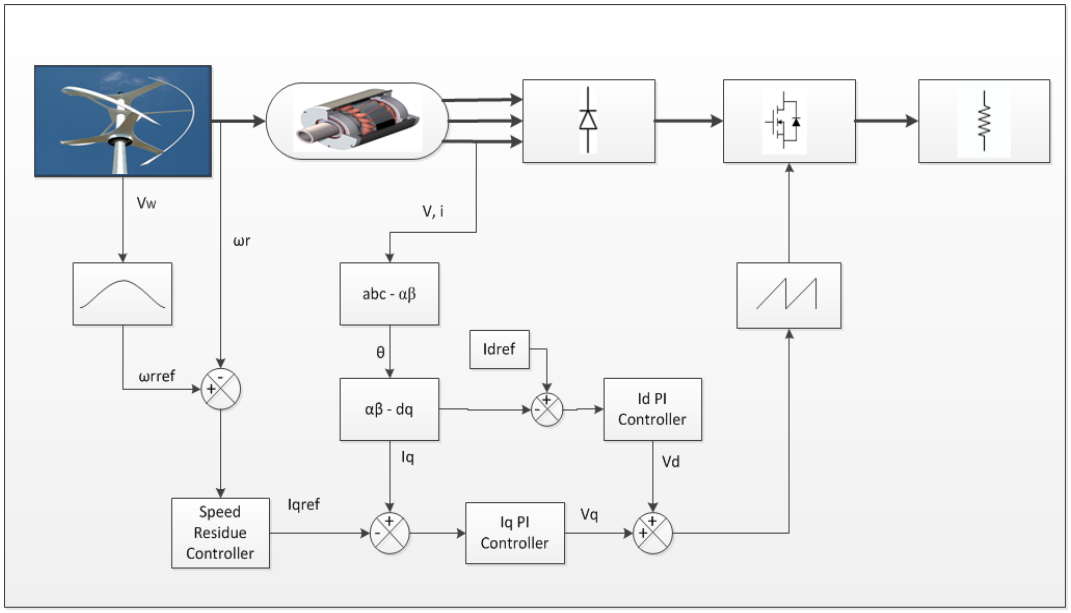

Figure 4.2: The control diagram for controller-I

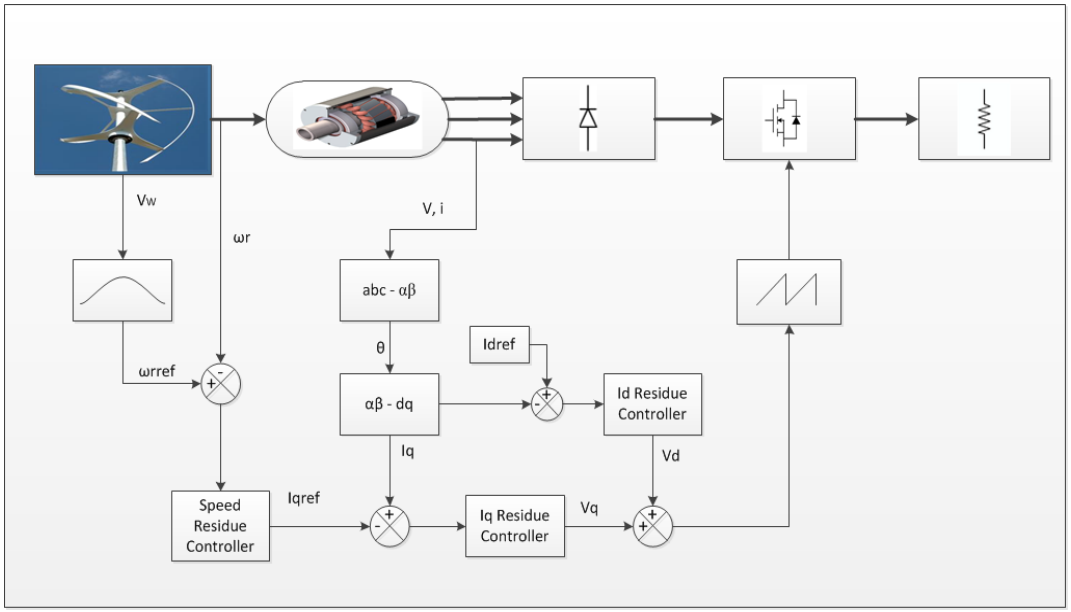

Figure 4.3: The control diagram for controller-II

fast enough to ensure the system robustness. High frequency oscillations are shown in the boundary limits. These oscillations are caused by the switching frequency since the boundary limit are affected by the error and the corrective

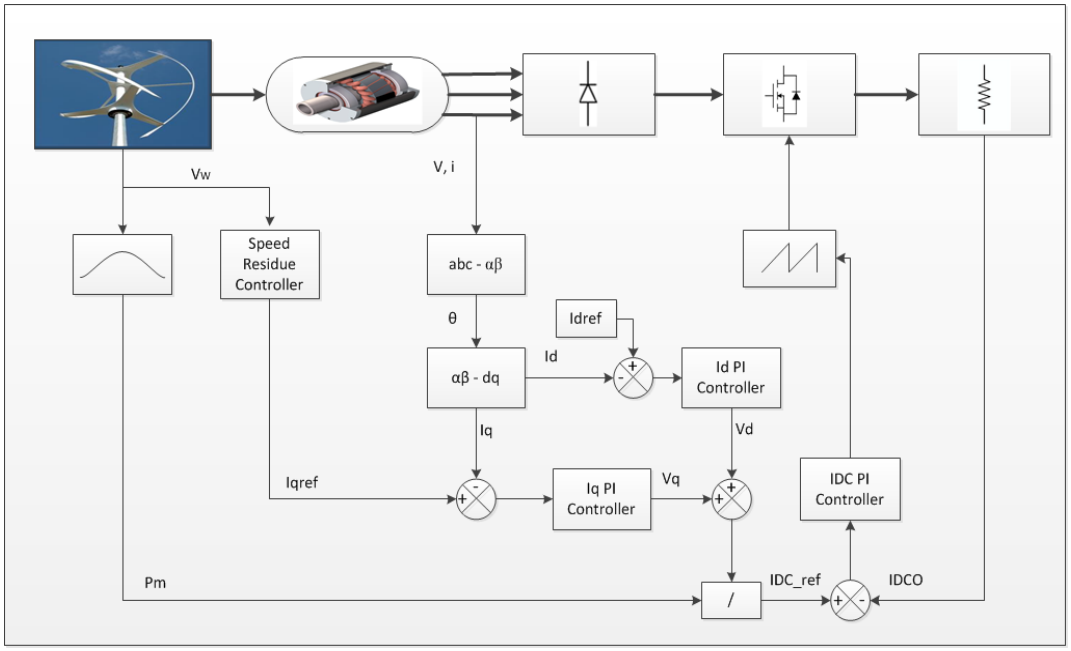

Figure 4.4: The control diagram for controller-III

actions. Figures 4.6 shows the actual speed tracking the reference speed for the first proposed controller (controller-I). It is noticeable that the actual speed accurately tracking the reference speed without any overshoots or steady-state errors. Also, the response speed is very fast and the settling time is at satisfactory level.

Figure 4.8 shows the actual speed tracking the reference speed for the second proposed controller (controller-II). It is noticeable that the actual speed is perfectly tracking the reference speed. There is a small overshoot appears in the speed response, which can be acceptable. The response speed is very fast and the settling time is at satisfactory level.

Figure 4.10 shows the actual speed tracking the reference speed for the third proposed controller (controller-III). Although, the speed response shows no overshoots. The raising time is slower than the previous two controllers. It is clear that the actual rotor speed is perfectly tracks the reference generated speed.

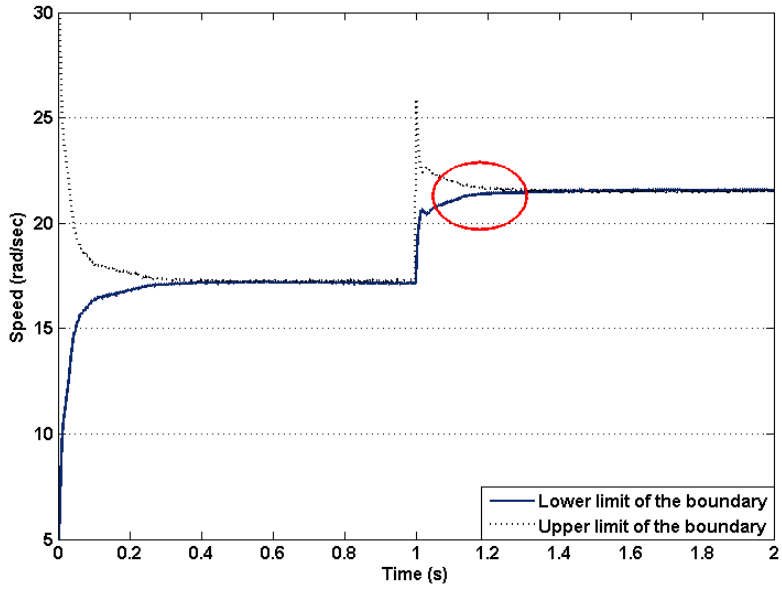

(a) The designed speed control boundary.

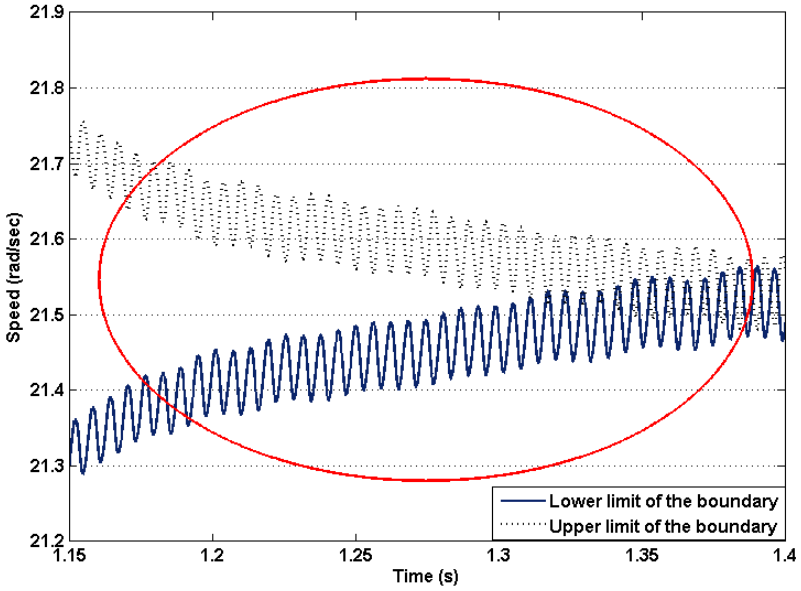

(b) A zoom in the designed speed control boundary.

Figure 4.5: Illustration of the designed speed control boundary.

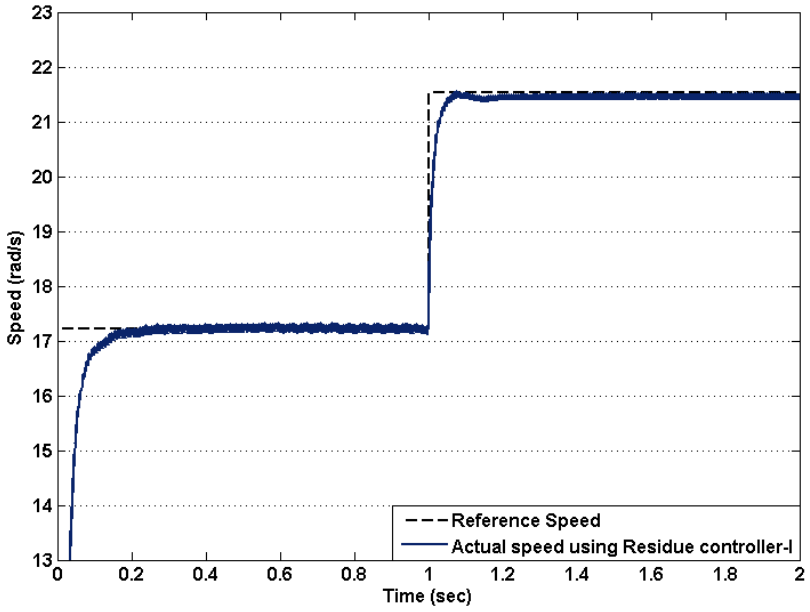

Figure 4.6: Actual speed tracking the reference speed for controller-I (i).

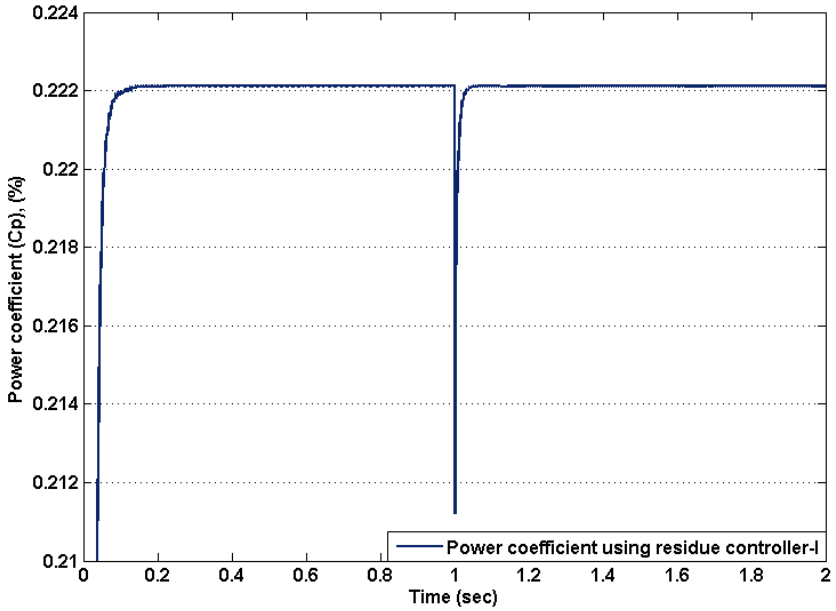

Figure 4.7: C_p under different wind speeds for controller-I (i).

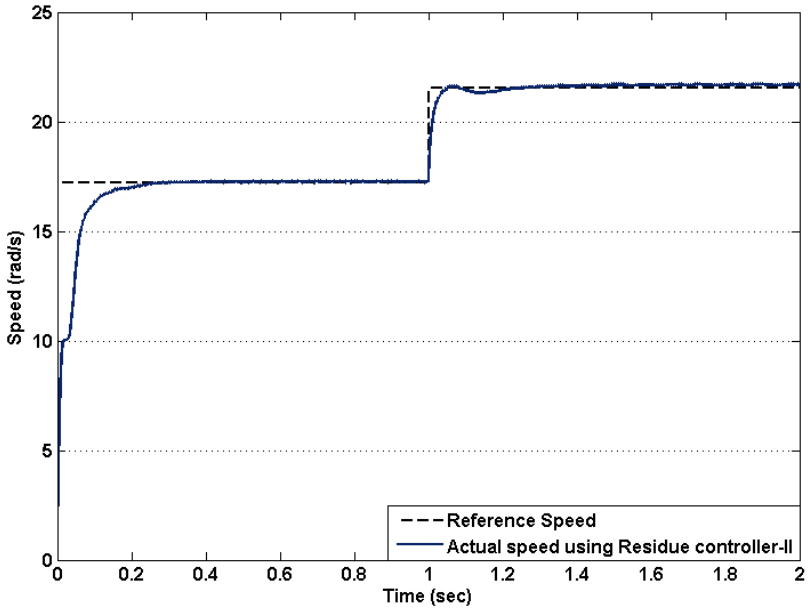

Figure 4.8: Actual speed tracking the optimum speed for controller-II (ii).

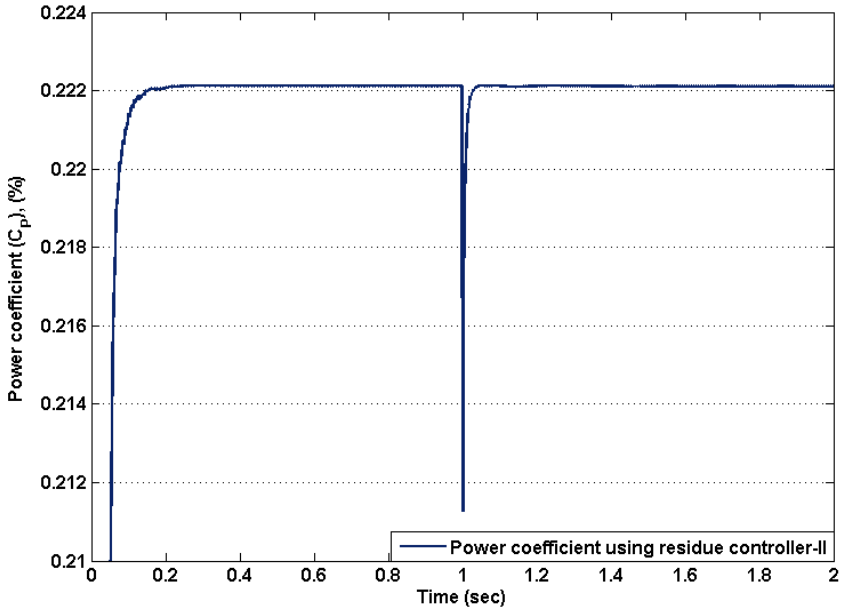

Figure 4.9: C_p under different wind speeds for controller-II (ii).

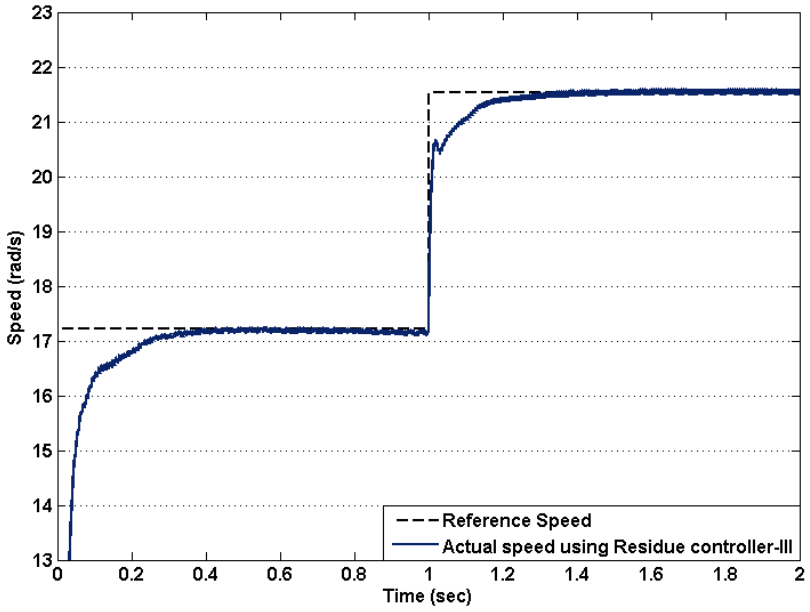

Figure 4.10: Actual speed tracking the reference speed for controller-III (iii).

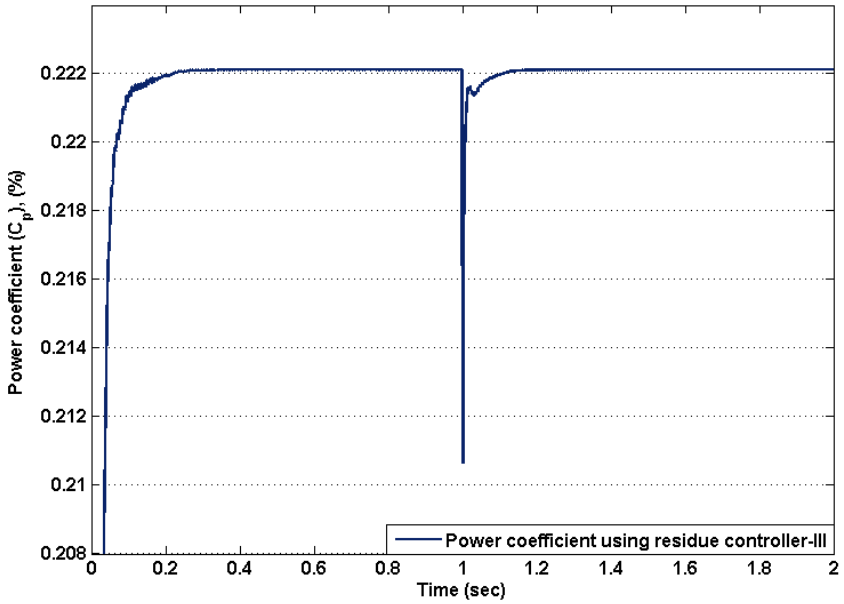

Figure 4.11: C_p under different wind speeds for controller-III (iii).

Table 4.1: Comparison between Residue controllers-I, II and III.

	Residue controllers-I	Residue controllers-II	Residue controllers-III
Rise Time (ms)	52.5	70	60
Settling Time (ms)	210	300	450
Steady-States error (rad\s)	0.01	0.10	0.02
Power coefficient (C_p)	0.2221	0.2221	0.2221

The maximum conversion of power is ensured and clearly shown in Figs. 4.7 , 4.9 and 4.11. The C_p is at its maximum value of 0.22. The improvement in the energy conversion ratio is significant as compared to results obtained in Chapters 3 and 2. The comparison between the three proposed residue controllers have been undertaken and pillustrated in Table 4.1.

The estimated wind speed algorithm has been implemented to residue controller-II. The reference rotation speed has been estimated using the value obtained from wind speed estimation algorithm. Figure 4.12 shows the actual rotor speed tracking the estimated reference speed generated from the MPPT algorithm. Also, the actual reference speed which is obtained from real wind measurement is shown in the figure. It is clearly shown that the estimated reference speed is almost equal to the actual reference speed. The TSR which is optimal at 0.82 can be shown in figure 4.14. Moreover, it is noticeable that the maximum power extraction is achieved and C_p is at its maximum value of 0.22.

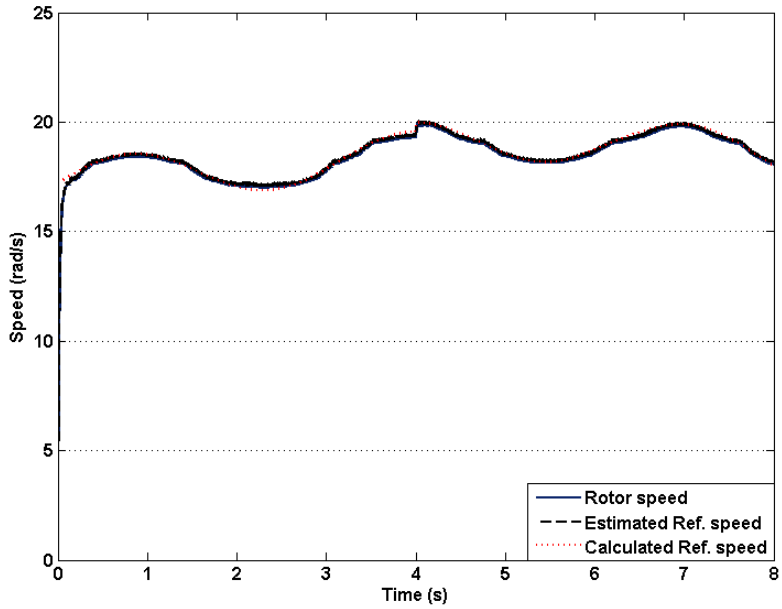

Figure 4.12: Actual speed tracking the estimated reference speed.

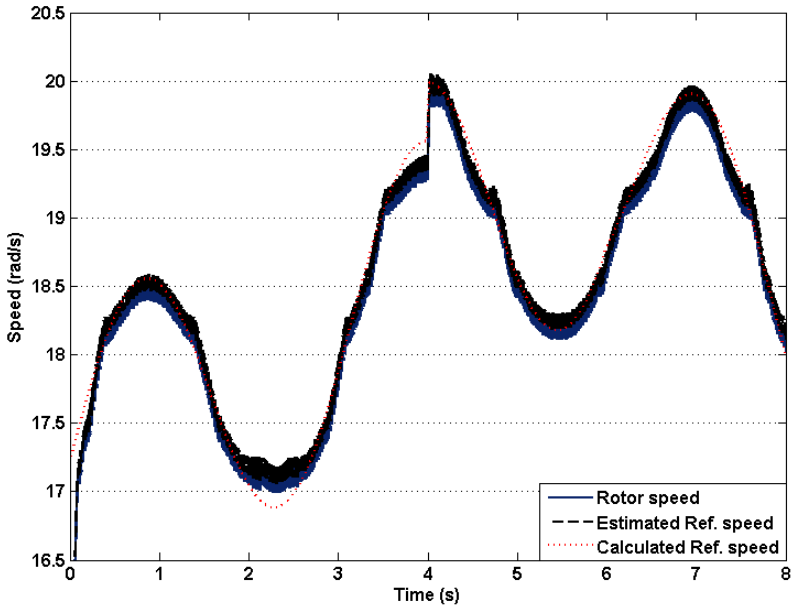

Figure 4.13: A zoom in the actual speed tracking the estimated reference speed.

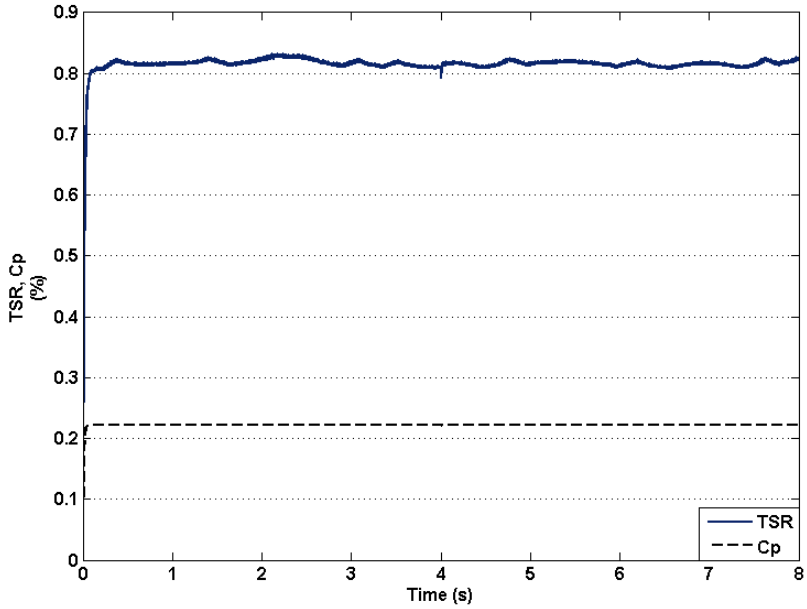

Figure 4.14: TSR and C_p under estimated wind speeds.

4.5 Comparison Analysis Between PI, SMC and Residual Controller

The proposed residual controller-I has been compared to a classical PI controller and a sliding mode controller-I and the comparison results are presented in Table 4.2. The residual controller is better than the PI and SMC in terms of achieving MPP. Figures 4.15 and 4.16 show the speed errors for the both controllers and a zoom in the speed error respectively. It is noticeable that the speed error of the residual controller changing around the zero, which means the rotor speed reaches the reference speed and varies around the designed speed boundary. Although, the speed response when using sliding mode controller reaches the reference speed perfectly. The speed error slide above the zero. Moreover, the dynamic boundary of the residual controller can be clearly shown at high speed.

Table 4.2: Comparision between PI, SMC and Residual control.

	PI	SMC	Residue controller-I
Rise Time (ms)	29	53.7	52.5
Settling Time (ms)	250	230	210
Steady-States error (rad\s)	0.035	0.13	0.01
Low Speed Chattering (rad\s)	0.1	0.117	0.13
High Speed Chattering (rad\s)	0.088	0.098	0.093
Power coefficient (C_p)	0.2166	0.2167	0.2221

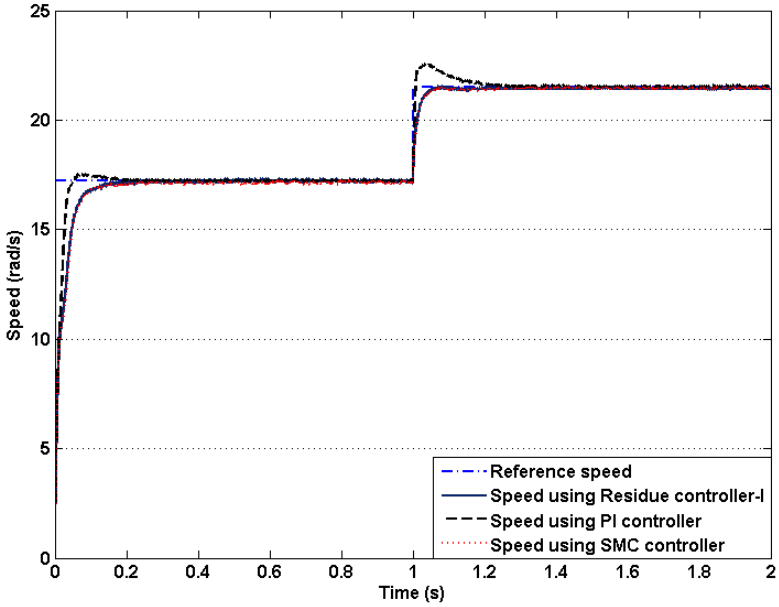

Figure 4.15: Speed response of PI, SM and Residual controllers.

Figure 4.17 shows the speed response of the three controllers for time analysis. It is clearly shown that the controllers actions are fast enough. The residual controller rises slightly faster than the SMC but slower than PI. Also, the settling time for the residual controller is less than that of the PI and SMC. It is worth to note that the residual controller has the highest power coefficient

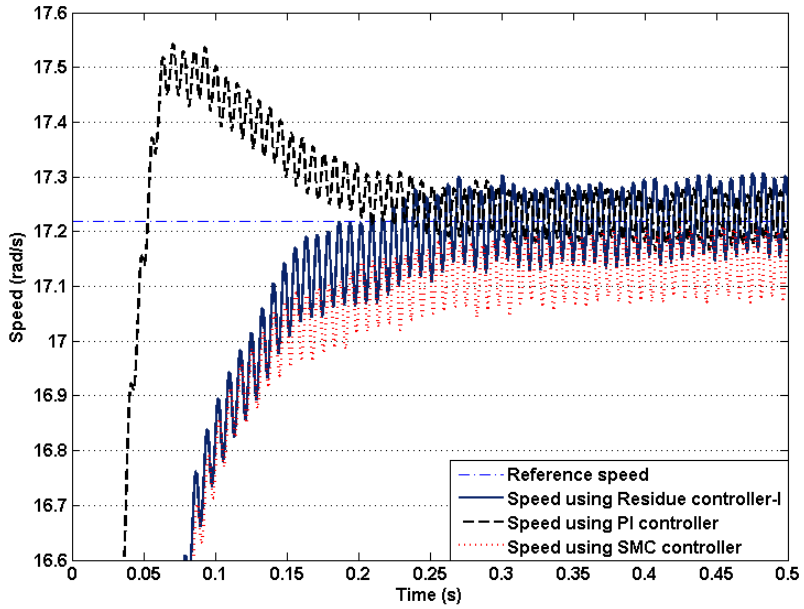

Figure 4.16: Zoom in the speed response of PI, SM and Residual controllers.

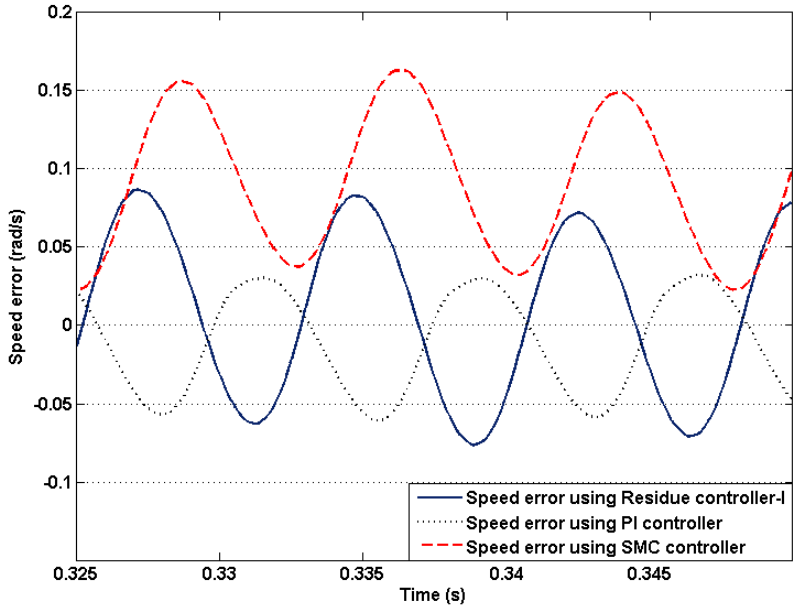

Figure 4.17: Speed error of PI, SM and Residual controllers.

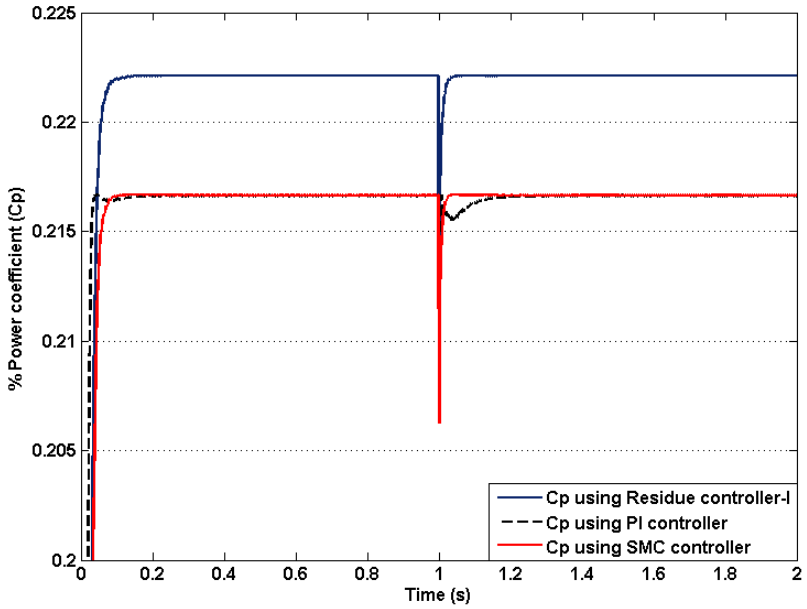

Figure 4.18: Achieved C_p of PI, SM and Residual controllers.

over other controllers. The power extracted when using residual controller is 2.5% than when using SMC. The reason is that the rotor speed under residual controller slightly varies around the zero, which can be an advantage of introducing the dynamic boundary.

According to Table 4.2, the chattering effect of SMC at low speed is less than that of the residual controller. However at high speed, the chattering effect reduces in the residual controller and increases in the SMC. It can be concluded that the residual controller has significant advantages over both PI and SMC, i.e. more power efficient, better dynamic performance, simple structure and implementation.

4.6 Experimental verifications

The experimental tests have been conducted using a WPGS test bench. The WPGS test bench consists of PMSG coupled with a 3-phase induction

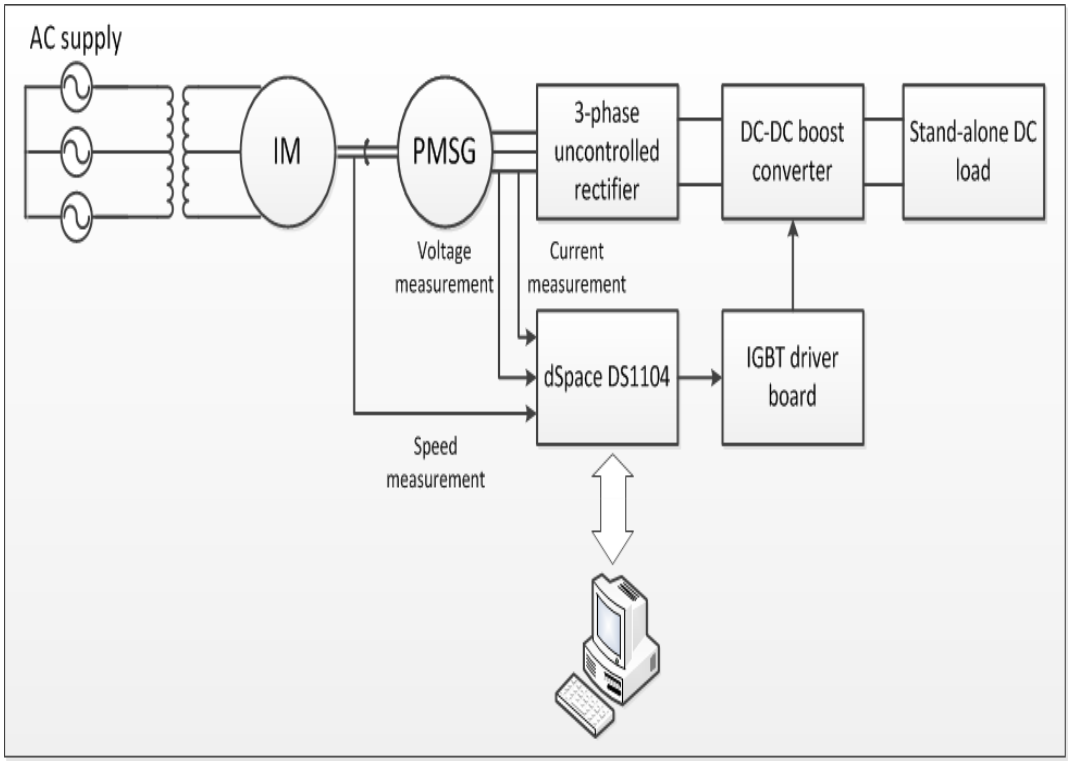

Figure 4.19: Block diagram of WPGS experimental configuration.

motor, which approximate the wind speeds in terms of mechanical torque. The 3-phase outputs of the PMSG are connected to a DC-DC boost converter to supply a resistive load. The measurements and control system are sampled and implemented by dSPACE DS1104 controller. Voltage and current transducers are used for measurement where an encoder is used for speed measurements. The experimental tests have been performed under two level of wind speeds 8 m/s and 10 m/s focusing in the transients response. The wind speed estimator was tested and implemented in the controller. The block diagram showing the experiment set up configuration is illustrated in Figure 4.19.

4.6.1 Hardware and Experimental Set Up

The wind turbine generator emulator shown in figure 4.20 consist of three main stages. The first stage is the electric machinery. This stage made up of

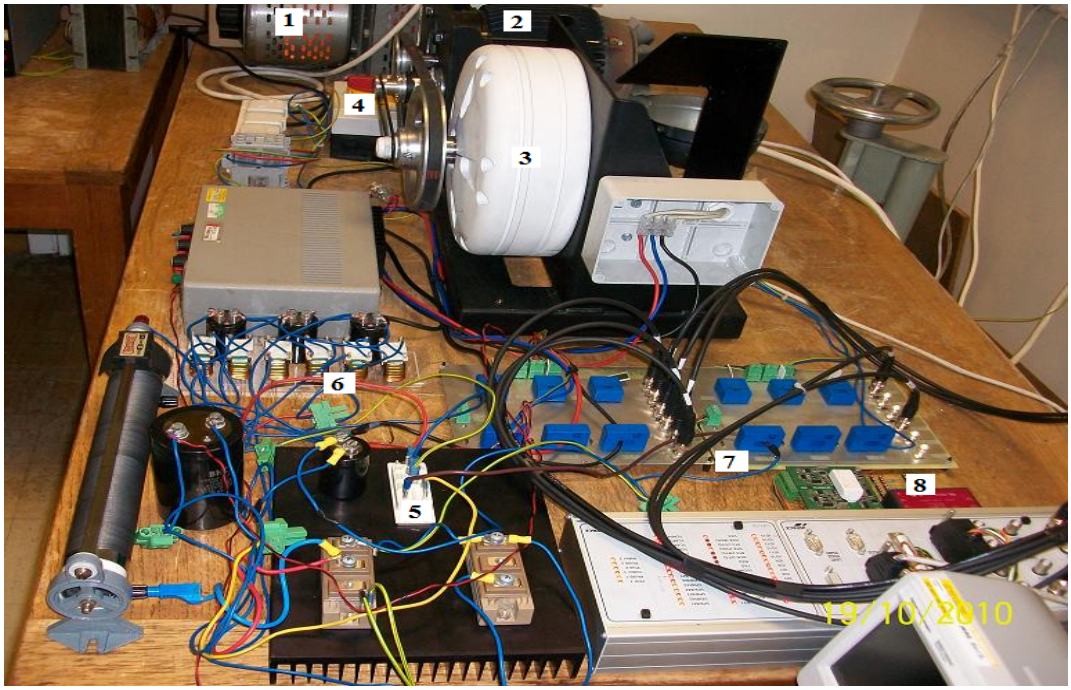

Figure 4.20: WPGS emulator system.

auto-transformer (1), three phase induction motor (2) and permanent magnet synchronous generator (3). The three-phase induction motor (prime mover) is connected to the power source via a three-phase main switch (4). The main is automatically disconnected when the input DC current of the boost converter becomes greater than 25 A. The auto-transformer is to provide a variable isolated three-phase voltage to the prime mover. By varying the input voltage of the prime mover, the mechanical speed of the induction motor is controlled to simulate the wind turbine power. The second stage is the power electronics switches and the load. It consists of DC-DC boost converter (5), which consists of three-phase six-pulse uncontrolled rectifier and two IGBTs for the boost converter. The first IGBT works as a power switch and its gate is triggered via PWM from the dSPACE. The second IGBT acts as a diode. The driver board (8) of the power switch is used to provide the required voltage level to fire the switch. The three-phase boost inductors (6) without the three-

phase capacitors are filter stage. In order to improve the waveform of the three-phase generator currents (decreasing THD), the three-phase capacitors must be connected to make LCL filters. The first inductor is the phase inductor of the generator and the second inductor is the boost inductor. The load is a variable DC resistance. The third stage is the measurement and control of the emulator which includes the voltage and current sensors board (7). It is important noting that the high voltages must be connected through connectors and the low voltages are measured from BNCs. The dSPACE controller kit which provides the control signals to and from the MATLAB/SIMULINK. The measurements of speed, currents and voltages are processed in the PC and the control action signal is send to the IGBT through the dSPACE controller. Details about the size and capacity of the hardware used in experiment are illustrated in Tables 4.3 and 4.4.

4.6.2 Experimental Results and Analysis

The PMSG-based WPGS experimental analysis have been carried out based on residue controller-II. Two control techniques have been implemented, i.e. using a mechanical speed sensor and estimated reference speed method. The experimental test have been done to verify the proposed control strategy based on residue theorem.

Figure 4.21 shows the actual speed tracking the reference speed at wind speed of 8 m/s. It can be shown in the figure that the proposed controller perfectly tracks the reference value. Errors in the speed measurements and motor vibration increases the chattering in the measurements and that appears in all the measured variables. The analysis of the residue controller-II with estimated reference speed is shown in Figure 4.22. The proposed wind speed estimator results are illustrated in 4.24. The estimated wind speed exactly matches the approximated value of the wind generated from the motor torque.

Table 4.3: Specifications of the hardware used in experiment [73].

Parameters	Value
Power Supply and Transformer	
Main Power Supply Voltage	400 V
Main Power Supply Frequency	50 Hz
Auto Transformer Voltage	30-110 V
Three-Phase Induction Motor	
Induction Motor Type	AEG-783471
Rated Output Power	1500 Watts
Number of Poles	4
Power Factor	0.8
Winding Connection	Δ/ Y
Voltage	220 V/ 380 V
Current	6.4 A/ 3.7 A
Frequency	50 Hz
Rated Rotor Speed	1440 rpm
Stator Phase Resistance	3.3 Ω
Rated Torque	9.95 N.m
PMSG	
Type	GL-PMG-500A
Rated Power	500 W
Rated Speed	450 rpm
Stator Winding Resistance	0.35 Ω
Moment of Inertia	0.066 $Kg.m^2$
Open Circuit DC Voltage	46 V
Rated Mechanical Power	15.5 N.m

Table 4.4: Specifications of the power electronics components used in experiment [73].

Parameters	Value
Three-Phase Diode Bridge Rectifier	1200 V, 50 A
DC-DC Converter Switch	IGBT
Capacitor	2.2 μ F
Inductor	0.4 mH
Variable Resistance Load	1-100 Ω
Voltage Transducer Model	LV25-p
Current Transducer Model	DS1104
dSPACE Model	LA55-p

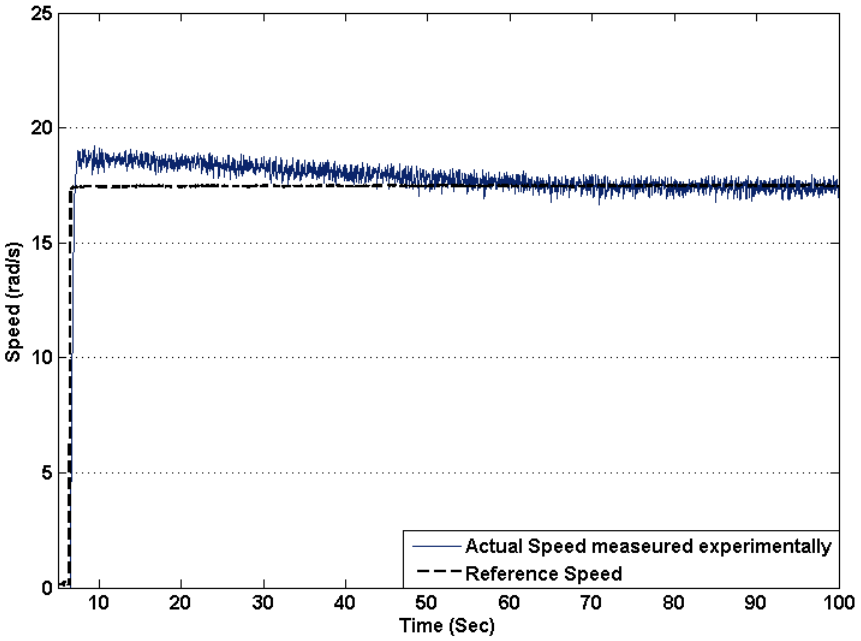

Figure 4.21: Actual speed tracking reference speed using wind speed measurements.

The estimator has been implemented in the control system and the results are presented in Figure 4.22a. It can be shown in the figure that the actual PMSG tracks the estimated reference speed perfectly. The zoom in the figure is illustrated in Figure 4.22b which shows the speed performance clearly.

The power coefficient, which is illustrated in Figure 4.26a clearly indicates a maximum power conversion ability of 0.216, where the theoretical maximum value of C_p is 0.22. The power coefficient value can be shown clearly in the zoomed in figure which is illustrated in Figure 4.26b. The tip speed ratio which is illustrated in Figure 4.25a indicated the achievement of the optimal value at 0.82. The details on the TSR value is illustrated in figure 4.25b.

It is clearly shown that the performance of the WPGS was enhanced when using wind speed estimator in terms of settling time and overshoots. The transients response is shown in Figure 4.27a. The figure shows actual speed tracking the reference speed during a step change in wind speed from 8 to $10m/s$. It was clearly shown that the controller perfectly reacts with the change in the reference signal and maintains the desired action in fast and smooth manner. Further details on the speed performance is illustrated in Figure 4.27b. For evaluating the simulations, a comparison between the simulation PMSG speed response and the experimental PMSG speed response has been shown in Figure 4.28. The analysis has been undertaken at wind speed value of 8 m/s. It can be clearly shown that the simulation results matches the obtained experimental results and the simulations have been validated.

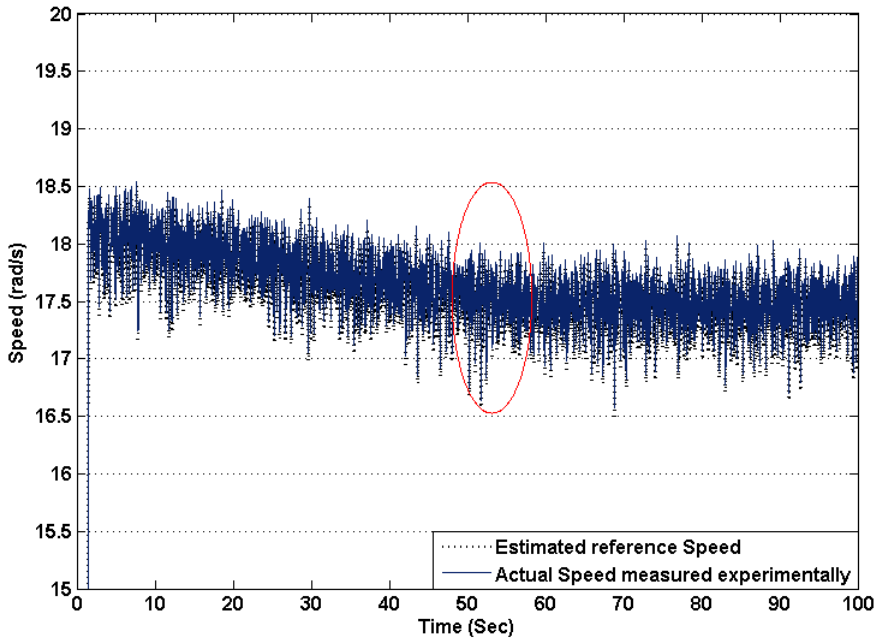

(a) Actual speed tracking reference speed using wind speed estimator.

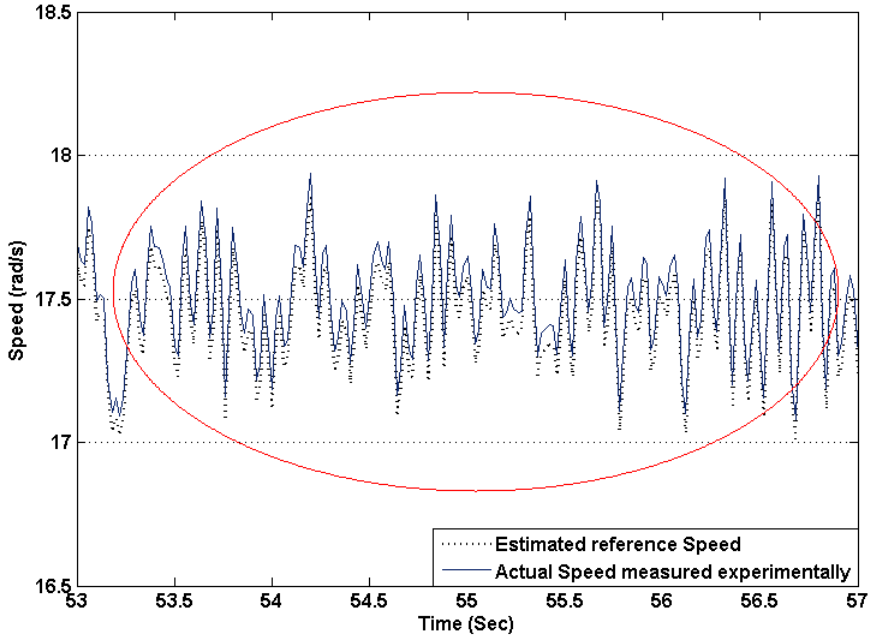

(b) Zoom in the actual speed tracking reference speed using wind speed estimator.

Figure 4.22: Experimental test analysis of residue controller-II.

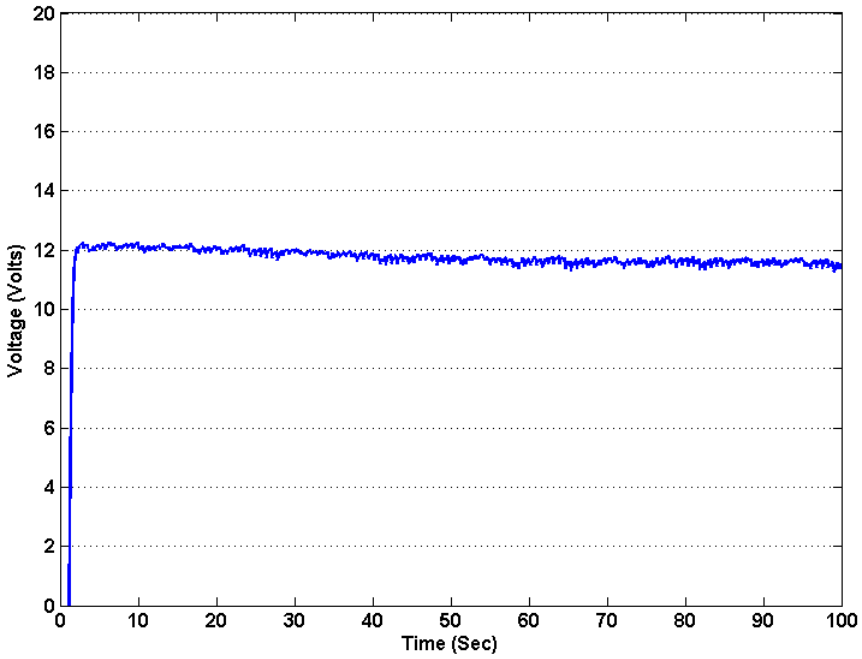

Figure 4.23: Output DC voltage measured experimentally.

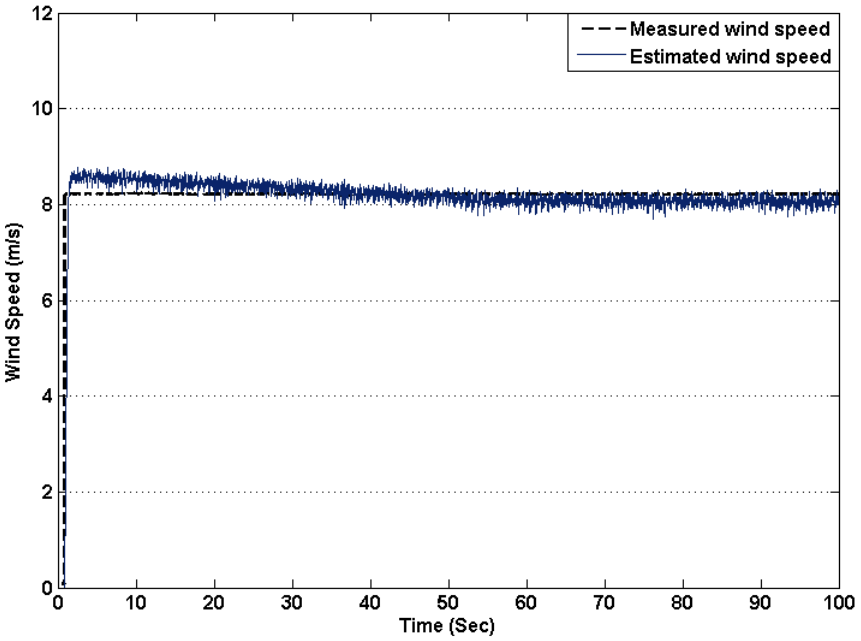

Figure 4.24: Measured wind speed versus estimated wind speed.

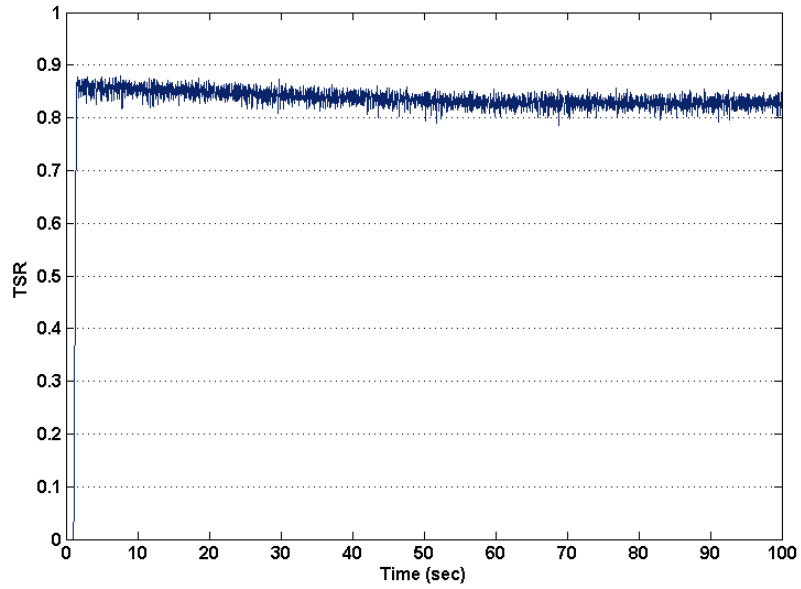

(a) Tip speed ratio λ.

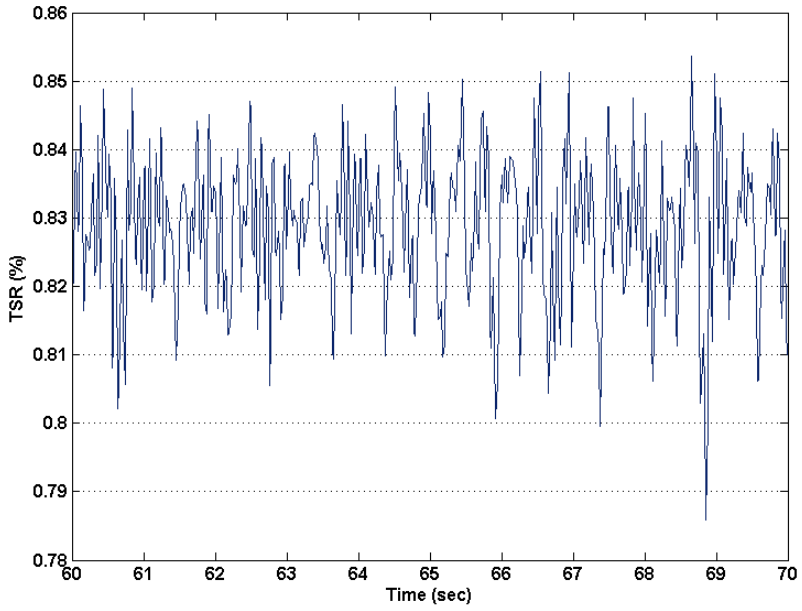

(b) A zoom in the tip speed ratio λ.

Figure 4.25: Experimental test analysis of residue controller-II TSR.

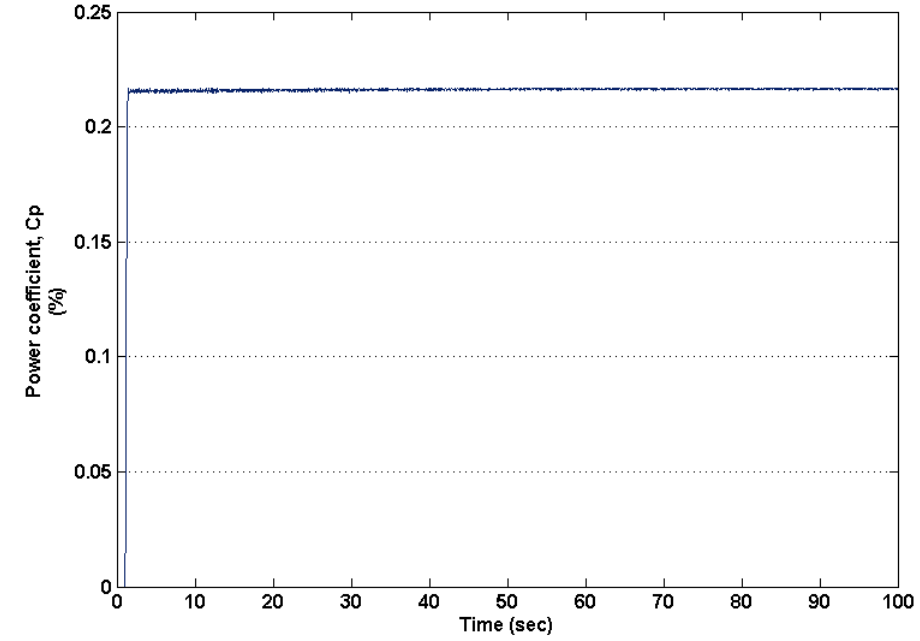

(a) Power coefficient C_p.

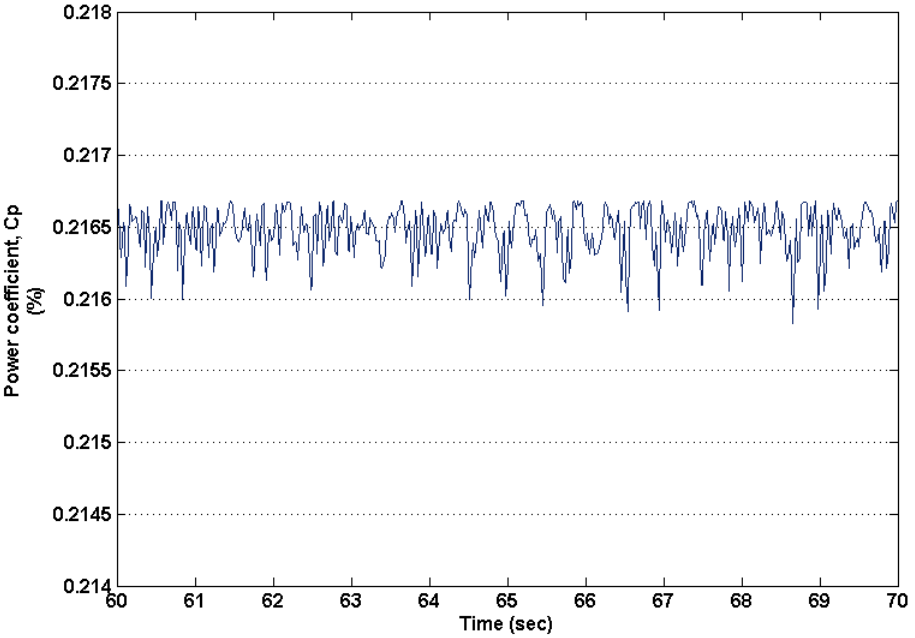

(b) A zoom in the power coefficient C_p.

Figure 4.26: Experimental test analysis of residue controller-II C_p.

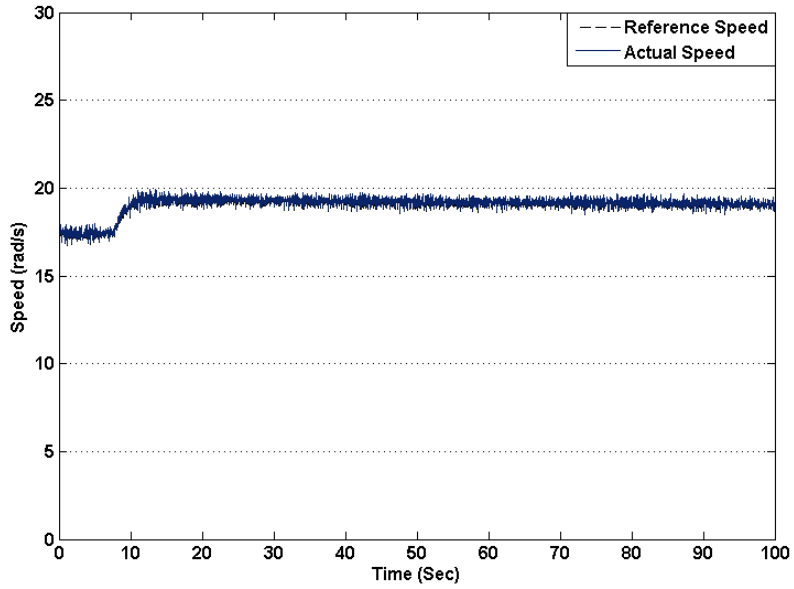

(a) Actual speed tracking reference speed during a step change in wind speed from 8 to 10 m/s.

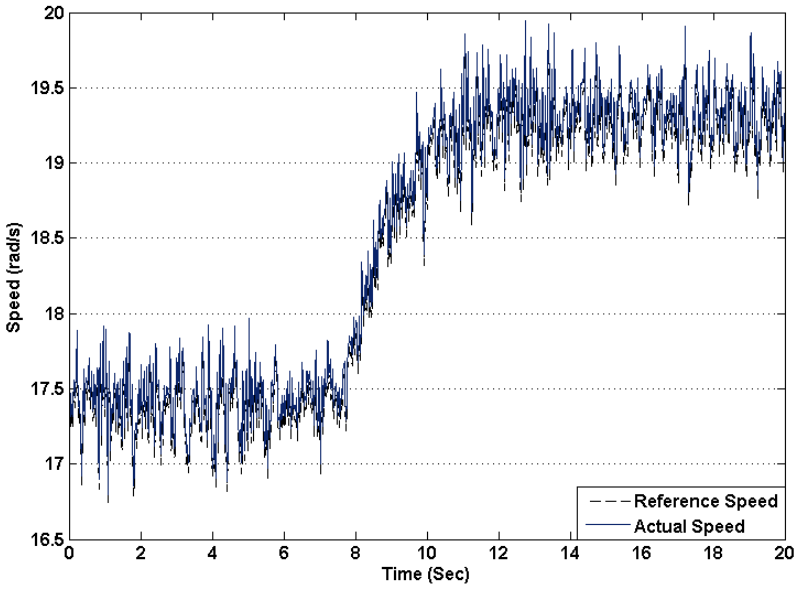

(b) A zoom in the actual speed tracking reference speed during a step change in wind speed from 8 to 10 m/s.

Figure 4.27: Experimental test analysis of speed transient response based on residue controller-II.

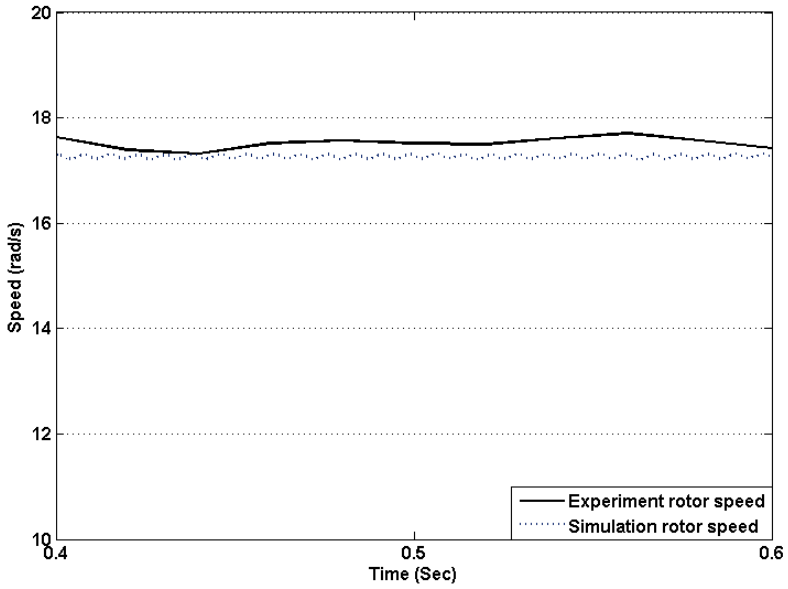

Figure 4.28: Comparison between the simulation and the experimental PMSG speed response at 8 m/s wind speed.

4.7 Conclusion

In this chapter, a new control method has been developed based on the residue theorem for WPGS. The idea is to create a soft boundary around a reference point and to force control variables to lie inside the boundary. Three types of controllers have been designed. For the first two controllers, the convergence of the manipulating variable to the set point is ensured by using the forward Euler method, where the exponential function ensures the convergence for the third controller. The three proposed controllers have been simulated and compared to each other. Based on the dynamic performance residue controller-I have a better and faster response. Also, a wind speed estimation algorithm has been introduced in this chapter. It can be concluded that the dynamic performance of the system and the energy conversion ratio have been improved when using estimated value of the wind speed.

Experimental test has been conducted based on residue controller-II and residue controller-II with estimated reference speed to validate the control scheme. The soft control strategy developed provides a stable operation which can be partially lost when changing the discontinuity behavior of SMC. The overshoot is completely absent and the response speed is fast and soft enough. It can be concluded that using the residue control method with combination of PI controller improves the dynamics performance for the PMAS based WPGS. In addition, a comparative study between PI, SMC and residual controllers has been provided in this chapter. Based on the comparison, the residual controller shows improved dynamic performance and higher energy conversion ratio than both PI and SMC. At this point, It can be noted that the tuning of the residue gain have been done manually since there is no straight forward technique for tuning.

Chapter 5

Sensorless Maximum Power Point Tracking Controller for Wind Power Generation System Based on Residual Control

This chapter proposes a direct sensorless Maximum Power Point Tracking Tip Speed Ratio (TSR) control based on wind speed and rotor speed estimation for wind power generation system with direct driven permanent magnetic synchronous generators. An improved back-EMF observer using residual theorem is designed to estimate the mechanical rotor speed of the PMSG using the stator current and voltage measurements. The wind speed is estimated using the calculated power obtained from the PMSG voltage and current measurements as well as the estimated rotor speed. Based on the wind and rotor speeds, the TSR is calculated and compared to its optimal value. The proposed controller uses only the stator currents and voltages measurements to control the WPGS.

5.1 Introduction

The amount of extracted power from wind depends on the wind and the control strategy of WPGS. For small-scale low-cost applications it is recommended to use PMSG with variable speed operation [95]. One advantage of the variable speed operation is the ability to keep a maximum conversion of power exists under different wind speeds. The MPPT algorithm objective is to maintain TSR at its optimal value, which insures the maximum capture of power under different conditions.

In this chapter, the rotor speed is estimated using improved back-EMF observer. The improved back-EMF observer use the residual value of the back-EMF rather than the calculated value. The idea is to create boundary around the exact calculated value and the residual value lies under this boundary. The calculated value is then compared with previous residual value. In addition, the wind speed is estimated using the wind power model and the calculated AC power. The MPPT controller generate a reference speed corresponds to an optimal TSR which insures the maximum power conversion. The residual value of the TSR is compared to the optimal value of TSR and the error is used to generate a PWM signal to control the switching of the DC-DC boost converter.

The investigated WPGS, which is shown in Fig. 5.1, consists of a vertical axial wind turbine (VAWT) coupled directly to a PMSG. The output of the PMSG is connected to an uncontrolled AC/DC rectifier. The DC output of the rectifier is connected to a DC/DC boost converter. The boost converter is operating in the continuous conduction mode.

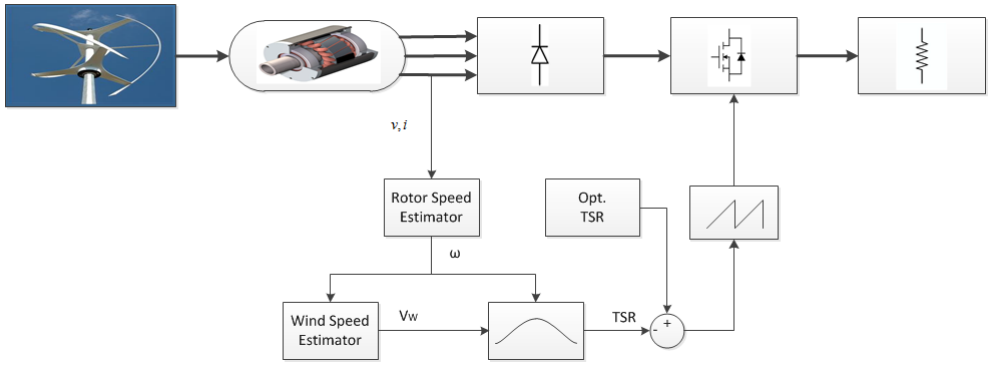

Figure 5.1: Wind generator system description and control

5.2 Improved Back-EMF Observer Based on Residue Theorem

Many techniques in estimating the rotor position have been reported [92, 93]. In this chapter, an improved back-EMF observer has been proposed to estimate rotor speed using the residual value of the back-EMF instead, since the back-EMF is a function of the rotating speed. The sinusoidal back-EMF equation in the $\alpha - \beta$ co-ordinate can be presented as follows [73]:

$$e_\alpha = L\frac{d}{dt}i_\alpha + R_a i_\alpha + V_\alpha, \tag{5.2.1}$$

$$e_\beta = L\frac{d}{dt}i_\beta + R_a i_\beta + V_\beta, \tag{5.2.2}$$

where $e_{\alpha\beta}$, $V_{\alpha\beta}$ and $i_{\alpha\beta}$ are the back-EMF, voltage and current of a PMSG in the $\alpha - \beta$ co-ordinate and L is the PMSG inductance. In classical back-EMF observer the rotor position θ can be estimated from (5.2.1) and (5.2.2) as, $\hat{\theta} = \tan^{-1}\left(\frac{e_\alpha}{e_\beta}\right)$ [94]. The implementation of the residue theorem in the back-EMF observer can be done following two stages. The first stage is to define the error according the forward Euler equation (4.2.3). The error e is the deference between the actual back-EMF minus the previous value of the back-EMF. The new error e_e equation can be defined as follows, where c is a

constant:

$$\dot{e_e} = e + c, \tag{5.2.3}$$

$$e_e = \int e + c, \tag{5.2.4}$$

$$e_e = \frac{e^2}{2} + ce. \tag{5.2.5}$$

The second stage is to define the boundary in which the back-EMF lies on. The proposed improved back-EMF observer has been developed in such a way that the back-EMF value is bounded by its value plus and minus the error. The proposed improved back-EMF observer can be shown as the following:

$$\hat{e}_{\alpha\beta} = RES(e_{\alpha\beta}), \tag{5.2.6}$$

$$\hat{e}_{\alpha\beta} = \frac{1}{2\pi} \int_{e_{\alpha\beta}-e_e}^{e_{\alpha\beta}+e_e} e_{\alpha\beta}, \tag{5.2.7}$$

$$\hat{e}_{\alpha\beta} = \frac{e_{\alpha\beta} e_e}{\pi}, \tag{5.2.8}$$

where $\hat{e}_{\alpha\beta}$ is the residual value of the back-EMF, a low-pass filter is introduced in the back-EMF observer with a time constant of $200\mu s$. This value has been selected according to the switching frequency and fined by simulations.

5.3 Maximum Power Point Tracking Tip Speed Ratio Control Using Improved Back-EMF Observer

The MPPT can be achieved by controlling the TSR to its optimum value λ_{opt} which is 0.82. The estimated values of the rotor speed and wind speed, which is presented in 4.3.4, are used to calculate TSR. The TSR is then compared to the optimum value and the error is defined using the residue theorem. The MPPT algorithm using the residue theorem can be express as below:

$$\lambda = \frac{\omega_r R}{V_w}, \qquad \lambda_{opt} = 0.82, \tag{5.3.1}$$

$$e_\lambda = \lambda_{opt} - \lambda, \qquad \dot{e}_k = e_\lambda + k, \tag{5.3.2}$$

$$\hat{\lambda} = \frac{1}{2\pi} \int_{\lambda_{opt}-e_k}^{\lambda_{opt}+e_k} \lambda, \tag{5.3.3}$$

$$\hat{\lambda} = \frac{\lambda_{opt} e_k}{\pi}, \tag{5.3.4}$$

where e_λ and e_k are the TSR error and the new TSR which is defined by the forward Euler method respectively. k is a constant.

The control diagrams of the developed MPPT controllers is shown in Fig. 5.1. For the proposed MPPT controller the stator voltages and currents are measured then the power is calculated. The measured data is used to estimate the rotation speed using an improved back-EMF observer by implementing the residue theorem. The estimated rotating speed as well as the calculated power is used to estimate the wind speeds. Both the estimated speeds are used to obtain a MPPT operation by calculating the TSR and compare the results to the optimum TSR and the error signal is used for controlling the PWM boost DC-DC converter operation.

In this research, the wind turbine is modelled as a vertical axial (VAWT) unit and the generator is a PMSG. The WPGS model has been simulated under variable wind speeds. The wind speed function fluctuates between 8 m/s and 10 m/s which simulate an actual wind profile. The parameters of the PMSG and the VAWT employed in this simulation are illustrated in Table 3.1.

The MPPT controller has been simulated using MATLAB/SIMULINK. The integration effect, which appears in the residue equation, makes the boundary limits changing in a soft manner. Figures 5.2a and 5.2b show the estimated speed tracking the estimated reference speed, which is generated from the MPPT algorithm. It is noticeable that the estimated speed accurately tracking the reference speed without any overshoots or steady-state errors. Also, the response speed is very fast and the settling time is at satisfactory level.

Figures 5.3a and 5.3a show the actual measured rotor speed tracking the estimated speed. It is clearly shown that the estimated rotor speed is very

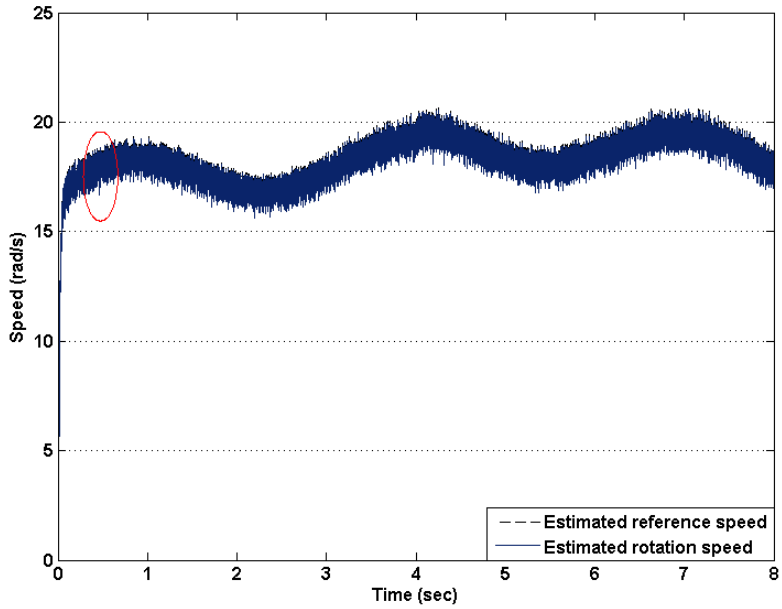

(a) Estimated speed tracking the Estimated reference speed.

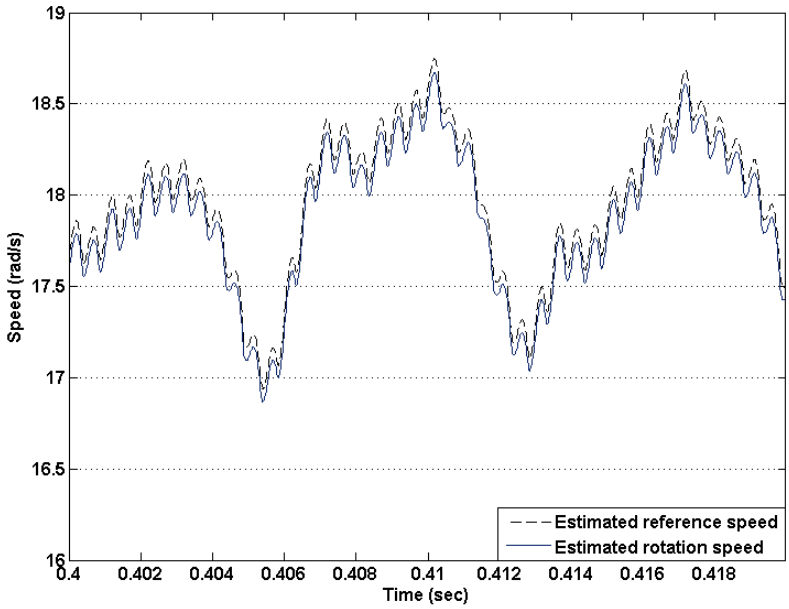

(b) A zoom in the estimated speed tracking the Estimated reference speed.

Figure 5.2: Dynamic performance analysis of the TSR control.

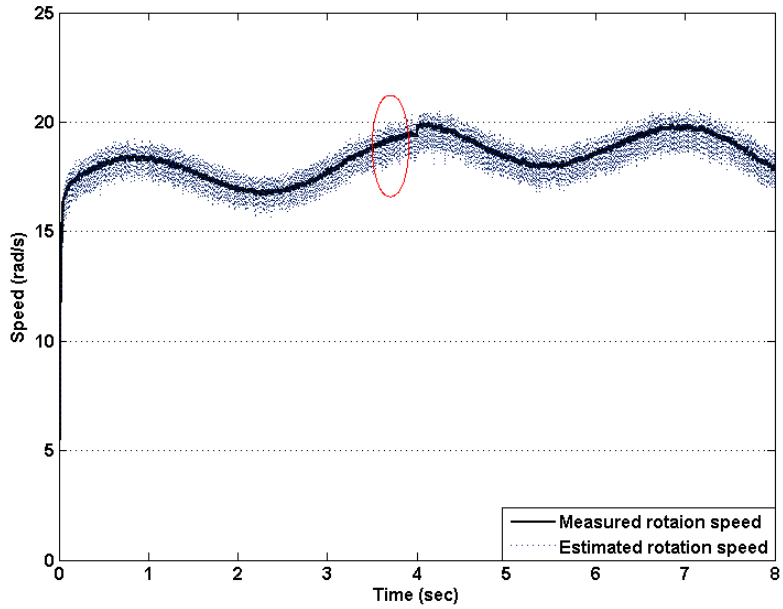

(a) Comparison between measured and estimated rotor speeds.

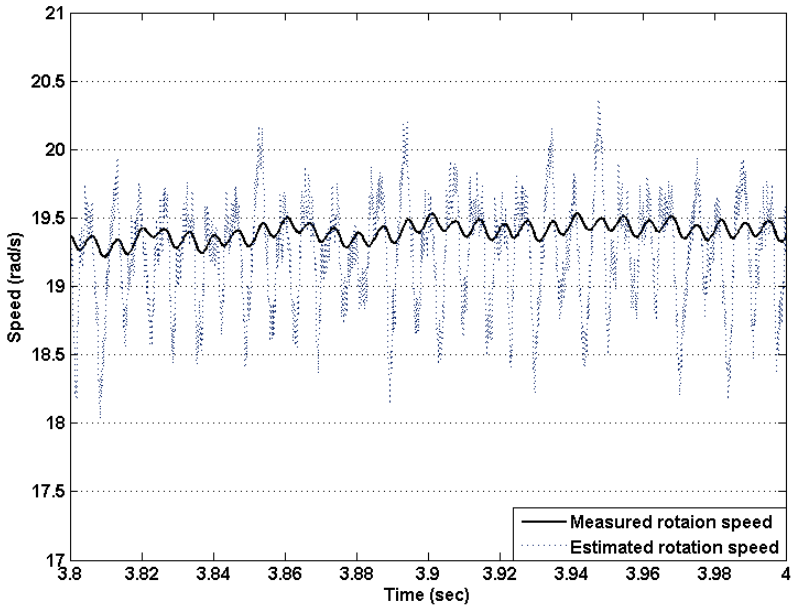

(b) A zoom in the comparison between measured and estimated rotor speeds.

Figure 5.3: Evaluation of the improved back-EMF observer.

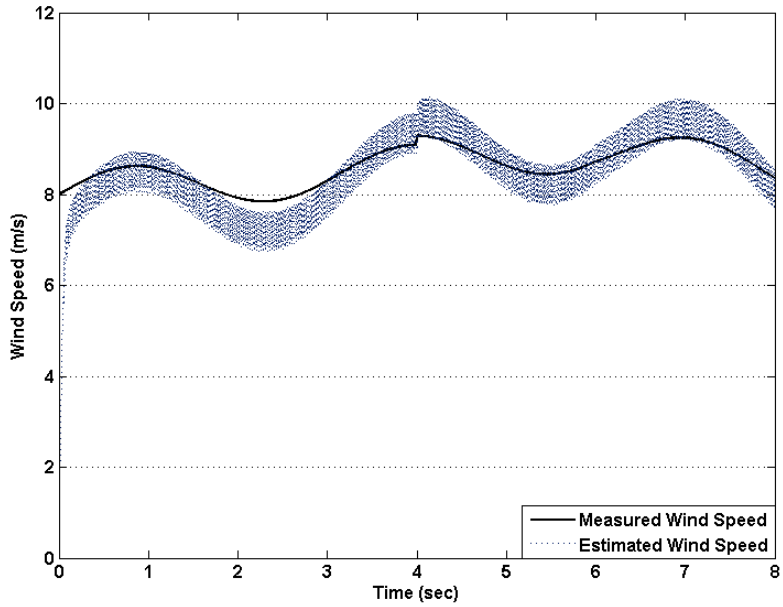

Figure 5.4: Comparison between Measured and estimated wind speeds.

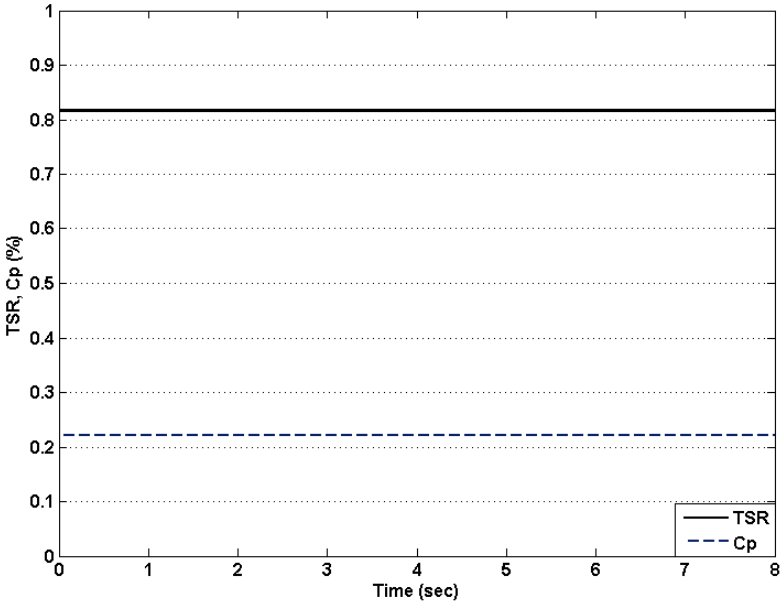

Figure 5.5: TSR and C_p using proposed TSR controller.

close to the measured rotor speed. According to the fact that the back-EMF observer has a poor performance at low speeds, the results shows an acceptable performance for the improved back-EMF observer at low speed. Moreover it can be noted that the estimated speed varies quickly and smoothly when the wind speed is changing.

Figure 5.4 shows a comparison between the measured wind speed and estimated wind speed. It is clear from the figure that the estimated wind speed accurately matches the measured wind speed. Also, the response speed is very fast and the settling time is at satisfactory level. The TSR and C_p shown in Fig.5.5 indicate their optimal values at 0.82 and 0.221 respectively.

5.4 Maximum Power Point Tracking Controller for Wind Generation System Based on Hill Climbing Technique

A hill climbing technique is one of the widely used algorithms in searching for the optimal operating point. In this research the objective of the proposed algorithm is to generate a reference speed signal based on the generated power. This reference speed is in fact the optimal speed at which MPP operation occurs. The algorithm has been designed in such a way that it observes the change in power with respect to speed. The mechanical speed has been initiated at 8 rad/s and the power threshold to 25 Watts. Moreover, to avoid the oscillation around the reference point a variable step size has been developed. The step size depend on the deviation size in power, i.e. for high difference in power the step size is bigger and it goes to a smaller step as the power difference in power decreases. Also, having such a variable step size decreases the searching time and the dynamic speed response become faster [114]. The following steps describe the hill climbing algorithm.

Step1: Calculate the change in electrical power.

Step2: Initiate the power threshold and the rotation speed, then define the speed step size.

Step3: If the power deviation is small use small step size in speed otherwise user bigger step size.

Step4: If the change in power is negative, calculate the change in speed.

Step5: For positive change in speed decrease the optimum speed, else increase the optimum speed by the step size.

Step6: If the change in power is positive, calculate the change in speed.

Step7: For positive change in speed increase the optimum speed, else decrease the optimum speed by the step size.

Step8: The optimum speed is the reference speed to controller for MPPT operation.

In this research, the d-axis and q-axis currents are controlled to their reference using SMC controllers while the mechanical speed is controlled to its reference using PI controller. Two models have been simulated one uses a speed measurement where the second is independent of the speed measurement and the speed is being estimated using classical back-EMF observer. The transients response have been analysed to investigate the control robustness. Figure 5.6 shows the speed response using classical back-EMF observer. It can be shown that the chattering effect appears in the speed as well as overshoot. However, the controller forces the speed to track its reference and MPPT operations are achieved. The TSR and the power coefficient are illustrated in Figure 5.7. It is clearly shown from the figure that the TSR and the power coefficient are at their maximum which indicates the achievement of MPPT successfully.

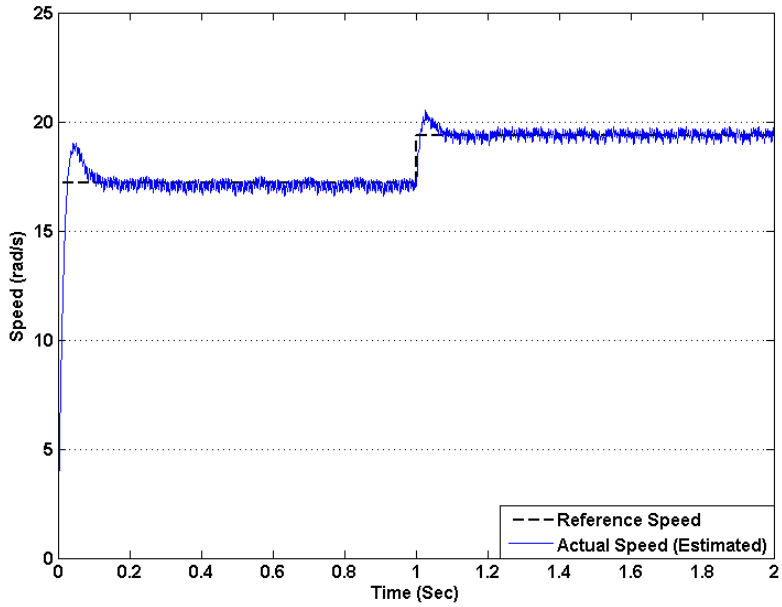

Figure 5.6: Actual speed tracking reference speed using classical back-EMF observer.

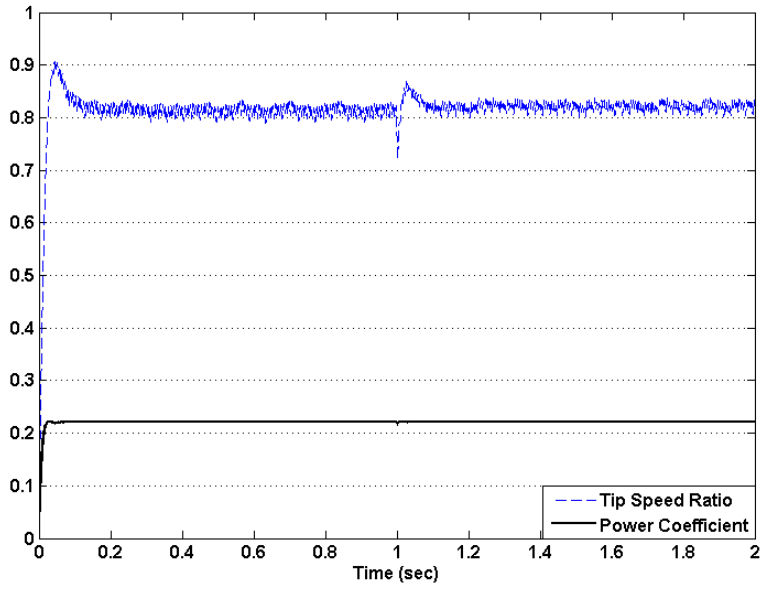

Figure 5.7: TSR and C_p using classical back-EMF observer.

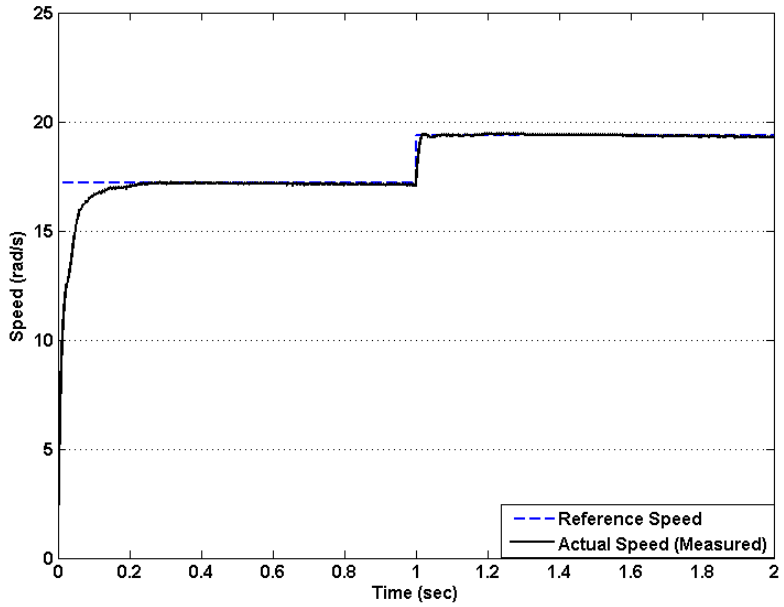

Figure 5.8: Actual speed tracking reference speed using speed measurements.

Figure 5.8 shows the speed response of the WPGS using mechanical speed measurements. It is clearly shown that the overshoots are eliminated and the chattering is at minimum. The TSR and the power coefficient are presented in Figure 5.9 which indicates MPPT operation and maximum power coefficient achieved. TSR is at its optimum value and the maximum energy conversion is achieved.

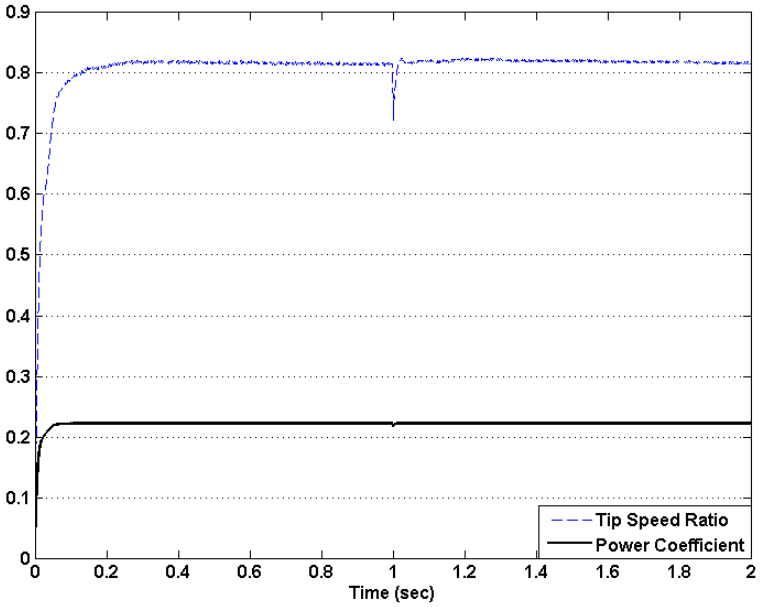

Figure 5.9: TSR and C_p using speed measurements.

5.5 Comparison Between Proposed TSR and Hill Climbing Controllers

The proposed MPPT TSR controller has been compared with the proposed sensorless MPPT controller based on hill climbing. The comparison has been done on the electrical power conversion ratio. Figure 5.10 shows the achieved C_p for the two proposed controllers. Both controllers have satisfactory dynamic performance and able to track and operate at maximum operation points. However, the proposed TSR controller based on the improved back-EMF observer has a slightly better performance and less chattering in the power coefficient ratio. Also, in terms of optimal TSR achievement, which is illustrated in Figure 5.11, the TSR based on the improved back-EMF observer shows a better performance.

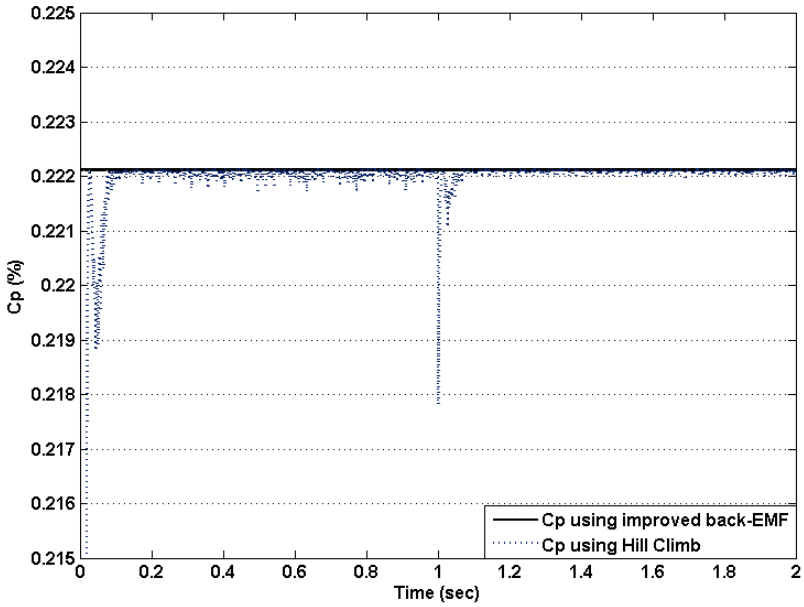

Figure 5.10: C_p comparison of the proposed controllers.

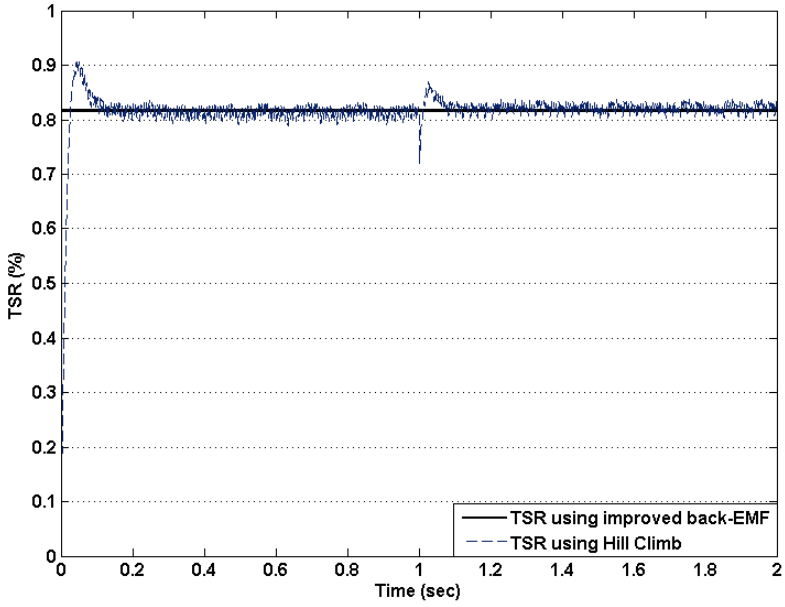

Figure 5.11: TSR comparison of the proposed controllers.

5.6 Rotor and Wind Speed Estimations

This section aims to develop estimators for wind speed and mechanical rotor speed for a Wind power generator system. Knowing the exact wind speed is a key factor in achieving a high performance control system. In order to overcome the problem of having a specific sensor to measure the wind speed, many sensorless techniques have been developed. In this section an exact and accurate estimation of wind and rotor speeds have been achieved by using a fuzzy inference system technique (FIS).

In fact, PMSG has been investigated in order to derive a set of indices that depend on the wind speed. These indices should be independent of the load variations. The fuzzy inference system has been proposed in such a way that it employs three indices to predict the wind speed. Also in this section, a back-EMF rotor speed observer has been proposed and compared to the FIS rotor speed estimator for the same WPGS.

5.6.1 Fuzzy Inference System

Fuzzy logic is a variation of crisp logic, where knowledge representation and inference mechanisms are closer to the way humans think. Variables in the crisp logic domain have undoubted values such as either 1 or 0, true or false, white or black. When humans handle variables, they do not think in terms of black and white; rather, they think in different shades of gray adding some uncertainty to the values [115, 116]. In the classical set theory, an element either belongs or does not belong to a specific set. On the other hand, the transition of an object being an element of a fuzzy set or another occurs gradually. Therefore, an element may belong to more than one fuzzy set at a time with different degrees of membership. The fuzzy inference system (FIS) is a popular soft-computing framework based on the concepts of fuzzy set theory, fuzzy if-then rules, and fuzzy reasoning. A FIS is essentially composed of three main components:

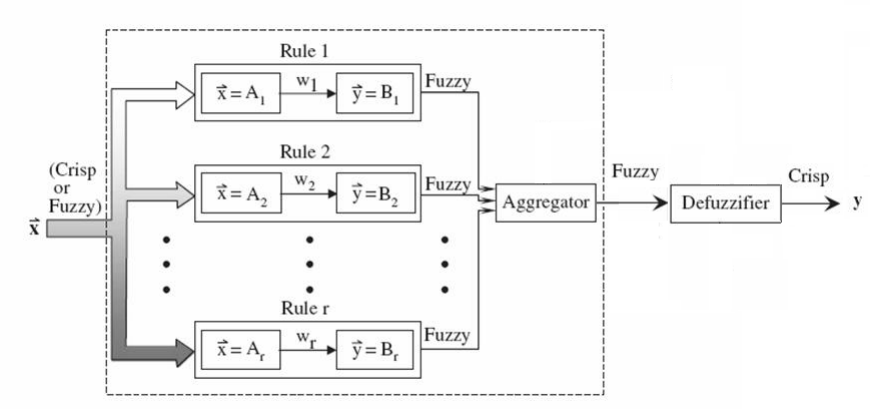

Figure 5.12: Block diagram of a FIS.

a database containing the parameters of every membership function (MF) of an input or output variable, a rule base including a set of fuzzy rules upon which the reasoning process is based, and a reasoning mechanism performing the inference procedures to derive an output or draw a conclusion. Since FIS processes fuzzy variables only, it should be equipped with a fuzzifier to translate crisp inputs into fuzzy entries [115, 116]. When crisp outputs are sought, a defuzzifier should follow the FIS in order to convert its fuzzy outputs into crisp figures. A block diagram representation of a FIS is shown in Fig. 5.12.

The back-EMF estimation as a speed observer is widely applied in modern control algorithms, since it can be applied to both sinusoidal and non-sinusoidal back-EMF machines [117]. However, additional filtering algorithms are required when applied to non-sinusoidal back-EMF machines in order to eliminate harmonic components [118, 119, 117]. The disadvantage of the back-EMF estimation is the poor performance at standstill and low speed operations [120]. In this section a back-EMF estimator is compared to the proposed FIS speed estimator.

Table 5.1: Variation of the indices at different wind speeds.

Wind speed	First Index	Second Index	Third Index
7.0	6.1	6.8	12.2
9.0	10.4	11.6	20.8
11.0	15.8	17.6	31.6
13.0	22.3	24.9	44.6
15.0	30.0	33.4	60.0

5.6.2 Wind Speed Estimation Using Fuzzy Inference System

A WPGS has been investigated at different wind speeds and different load values in order to figure out specific indices to predict the wind speed and to estimate the mechanical rotor speed. In the simulation of the PMSG, it is noticeable that the shape of the q-axis current in terms of harmonics distortion is varied under different wind speeds, but on the other hand the amount of loading had no significant effect on it. By applying the Fourier analysis based on the switching frequency to the q-axis current, there were significant variations on three main harmonic components. These components are with orders 0, 3rd and 5th. Figure 5.13 shows the variation of the indices at low, rated and high wind speeds at 100 Ω. Figure 5.14 shows and validate the independency of the indices from the load variation, where the indices are shown at 1000 Ω. The exact similarity between the two figures proves that the amount of the load does not affect the amplitude of the indices and they are only affected by wind speed variations. The simulation has been done at different wind speeds and the amplitudes of the indices are shown in Table 5.1.

A FIS has been designed with three inputs and one output and using the Mamdani model, which is widely used and simpler than Sugeno model, with

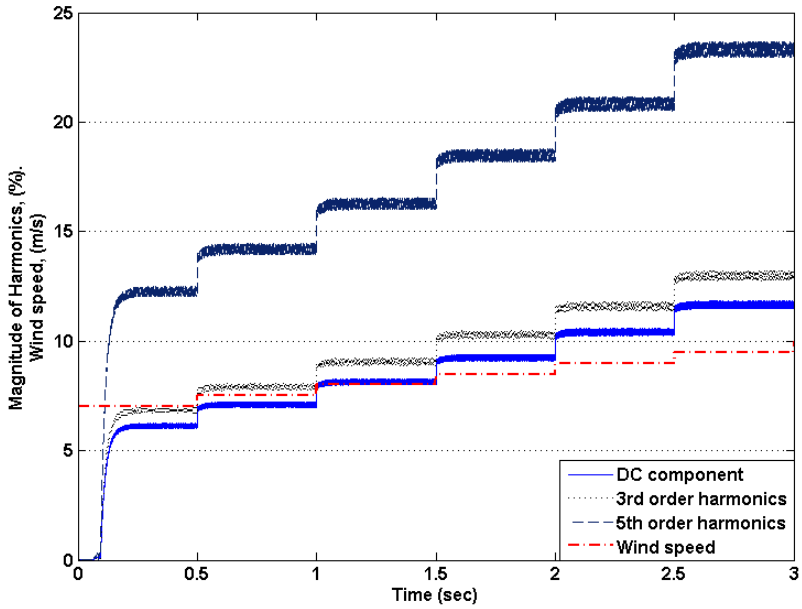

Figure 5.13: Variation of the indices at different wind speeds with 100 Ω.

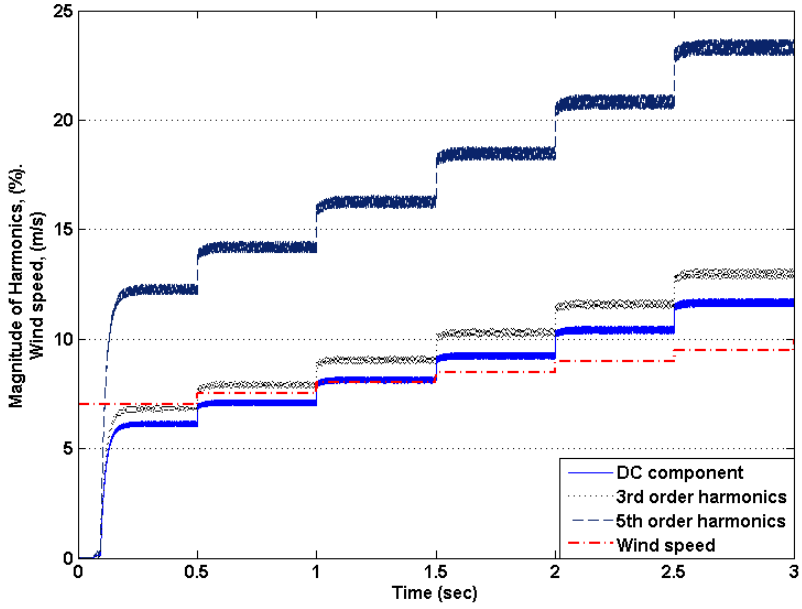

Figure 5.14: Variation of the indices at different wind speeds with 1000 Ω.

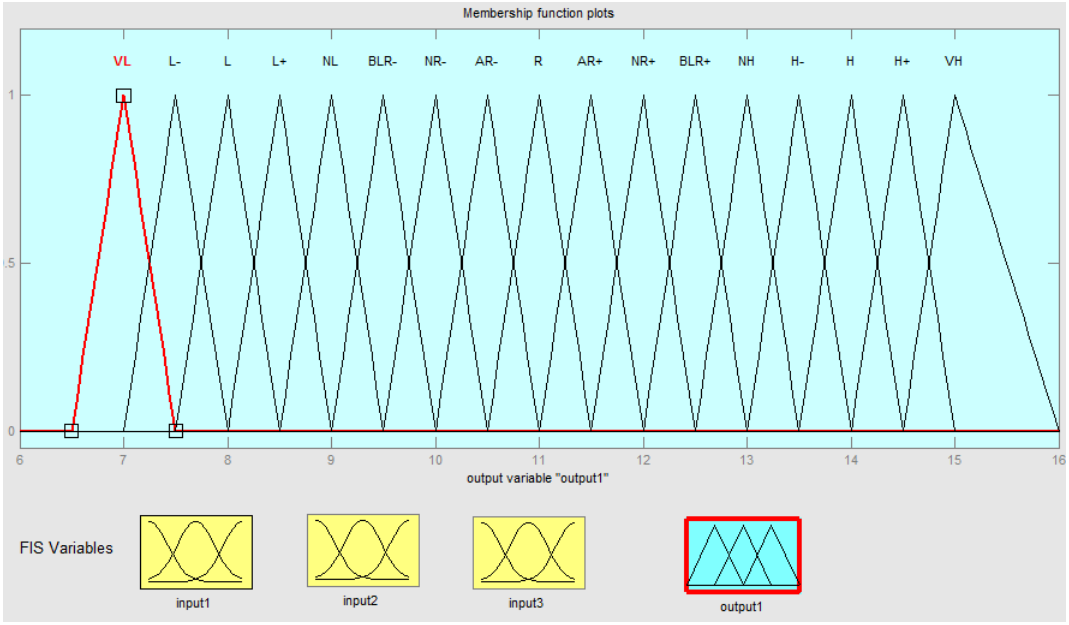

Figure 5.15: Output membership functions for the designed wind speed estimator using FIS.

the centroid deffizfication method [121]. The designed FIS has 17 membership functions for each input and output. These membership functions define the range of wind speed operations. Figure 5.15 shows the membership functions for the output, where the membership functions are defined in Table 5.2.

The proposed wind speed estimator using FIS has been tested using MATLAB/SIMULINK and it gives satisfactory outputs at different wind speeds. These outputs can be used in generating a reference speed for a maximum power point tracking (MPPT) controller. Figure 5.16 shows the online process of wind speed estimator. It can be shown from the figure the variations of the inputs of the FIS and the aggregation to a crisp output using Mamadani model.

Figure 5.17 shows the output of the proposed wind speed estimator using FIS compared with the actual wind speed in order to evaluate the estimator performance. It illustrates that the proposed wind speed estimator can accu-

Table 5.2: Definitions of the membership functions.

Wind speed range	Label	Description
6.5-7.5	VL	Very low wind speed
7.0-8.0	L-	Just below low wind speed
7.5-8.5	L	Low wind speed
8.0-9.0	L+	Just above low wind speed
8.5-9.5	NL	Normally low wind speed
9.0-10.0	BLR-	Below rated wind speed
9.5-10.5	NR-	Normally below rated wind speed
10.0-11.0	AR-	Below just about rated wind speed
10.5-11.5	R	Rated wind speed
11.0-12.0	AR+	Above just about rated wind speed
11.5-12.5	NR+	Normally above rated wind speed
12.0-13.0	BLR+	Above rated wind speed
12.5-13.5	NH	Normally high wind speed
13.0-14.0	H-	Just below high wind speed
13.5-14.5	H	High wind speed
14.0-15.0	H+	Just above high wind speed
14.5-16.0	VH	Very high wind speed

rately predict the wind speed and the response time is fast enough to maintain the stability and robustness of the system. The chattering of the output is very small indicating acceptable value. In fact, these chattering is caused by the crisp output of the FIS, however it might be a reasonable solution if the membership functions is increased. Increasing the membership functions reduces the size of the boundary of each crisp value. Figure 5.18 shows the test result of the proposed wind speed estimator under sinusoidal wind variations.

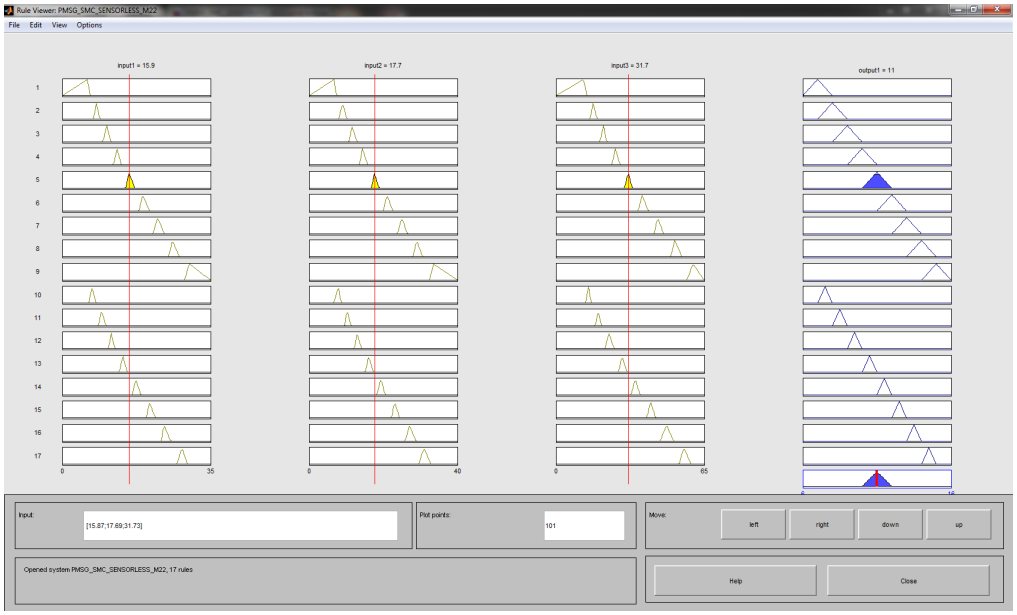

Figure 5.16: Online process of wind speed estimator.

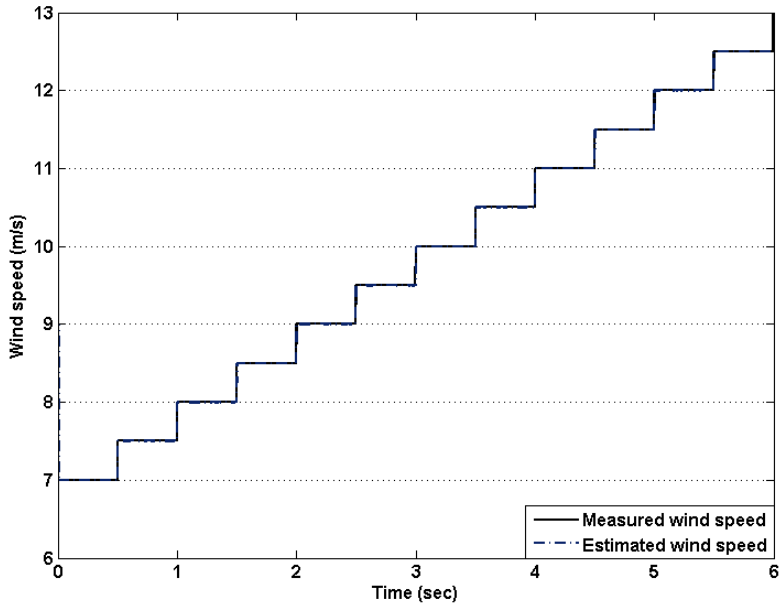

Figure 5.17: Estimated wind speeds versus actual wind speeds under step variation.

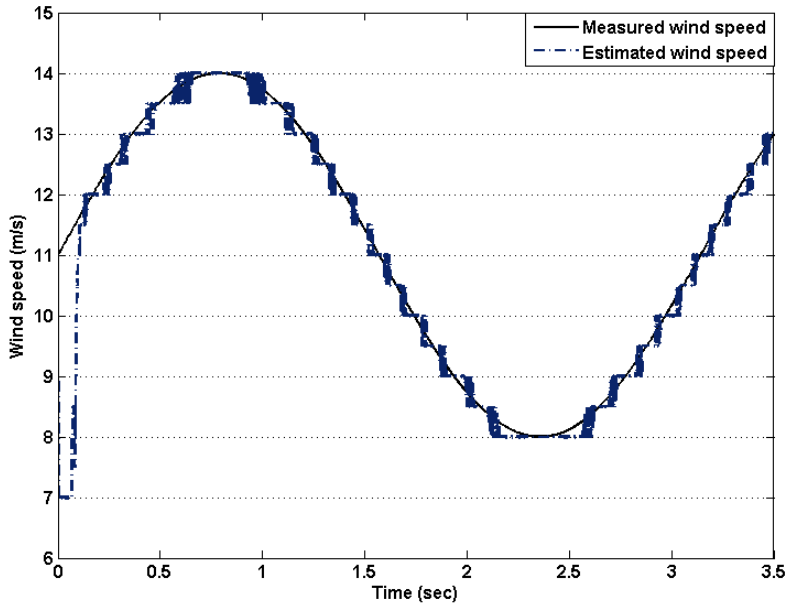

Figure 5.18: Estimated wind speeds versus actual wind speeds under sinusoidal variation.

5.6.3 Rotor Speed Estimator Using Fuzzy Inference System

The system has been analysed in similar way of the proposed wind speed estimator using FIS, which is presented in 5.6.2. The indices are the fundamental, the third harmonic and the fifth harmonic. The rotor speed estimator using FIS has been designed for three inputs and one output using the Mamdani model with the centroid deffuzfication method. The designed FIS has 22 membership functions per input and 22 membership functions per output. These membership functions define the range of rotating speeds.

The proposed rotor speed observer using FIS has been tested and it gives a satisfactory output at various rotation speeds. Figure 5.19 shows the output of the proposed rotor speed estimator with the actual rotating speed in order to evaluate the the proposed estimator. It is noticeable that the proposed

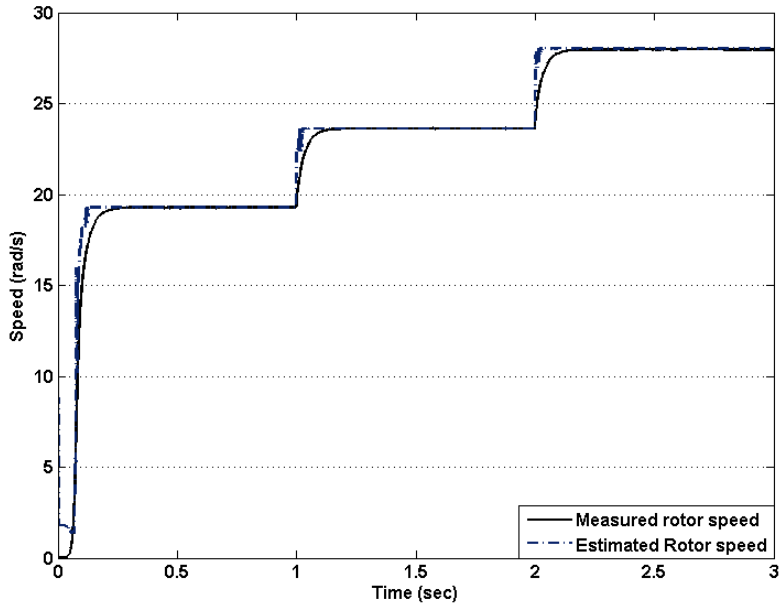

Figure 5.19: Estimated rotor speeds versus actual rotor speeds under step variation.

estimator can accurately estimate the rotating speed and the response time is fast enough to maintain the stability and robustness of the system. Figure 5.20 presents the test result of the proposed rotor speed estimator under non-uniform reference speed variations.

5.6.4 Comparison Between Improved Back-EMF, Classical Back-EMF and FIS Rotor Speed Observers

The developed classical back-EMF speed observer has been simulated. Figure 5.21 shows the estimated speed versus the measured rotor speed under step wind speed variations. The results shows chattering on the estimated speed which is in fact caused by the poor performance of the classical back-EMF observer at low speeds operations. Figure 5.22 shows the estimated speed versus the measured rotor speed under non-uniform wind speed variations. The

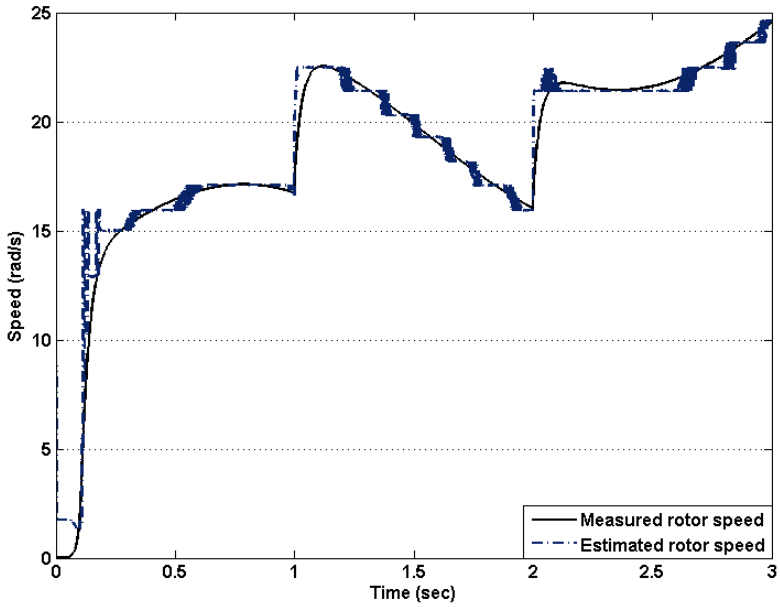

Figure 5.20: Estimated rotor speeds versus actual rotor speeds under non-uniform variation.

results also shows a high chattering effect and a mismatch to the actual speed.

The proposed improved back-EMF speed observer has been compared to FIS rotor speed estimator and back-EMF observer. Figure 5.23 shows the three rotor speed estimators response tracking reference speed during non-uniform wind speed variations. The results show that the improved back-EMF observer has an improved response with less chattering and accurate estimation over both FIS and classical back-EMF. Another advantage of the improved back-EMF over fuzzy back-EMF observer is simplicity of implementation.

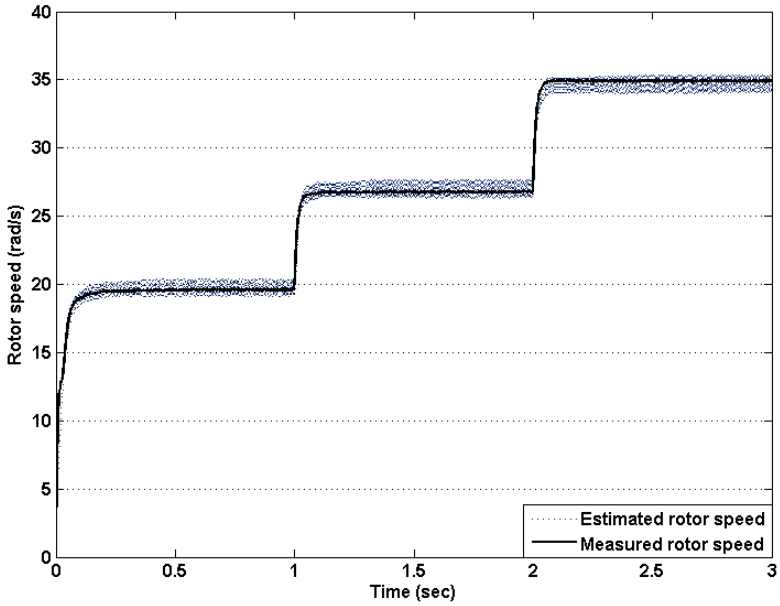

Figure 5.21: Estimated rotor speeds versus actual rotor speeds under step variation using back-EMF observer.

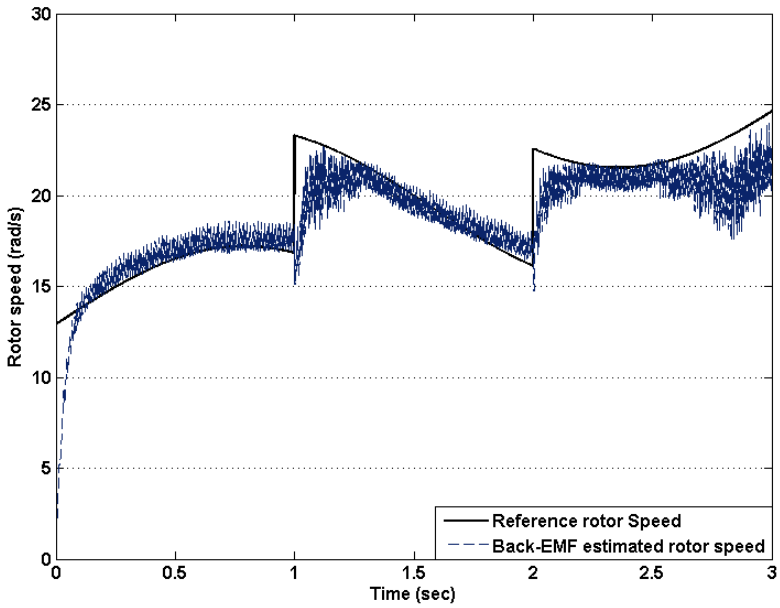

Figure 5.22: Estimated rotor speeds versus actual rotor speeds under non-uniform variation using back-EMF observer.

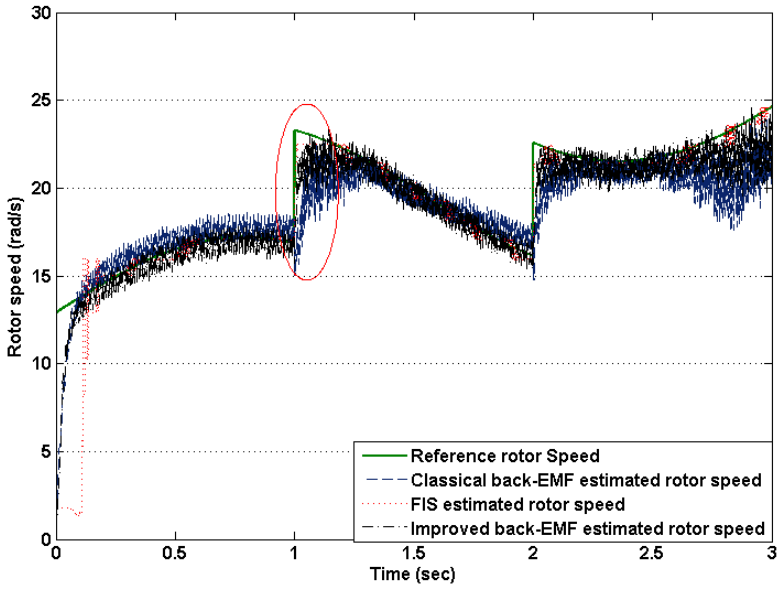

(a) Rotor speed observers under non-uniform wind speed variations.

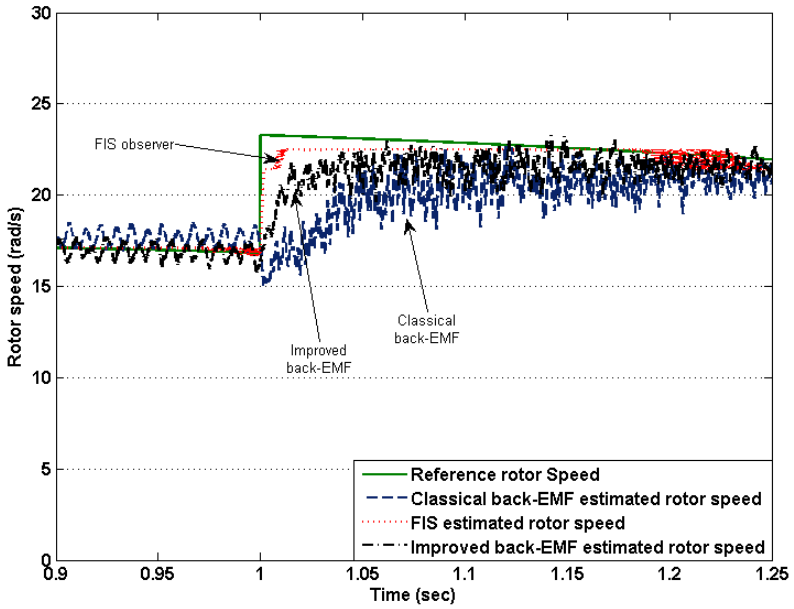

(b) Zoom in rotor speed observers under non-uniform wind speed variations.

Figure 5.23: Comparison between FIS, classical back-EMF and Improved back-EMF rotor speed observers under non-uniform wind speed variations.

5.7 Conclusion

In this chapter, a new sensorless MPPT controller based on the residue theorem has been developed. The idea is to create a soft boundary around a reference point and to force control variables to lie in a point inside the created boundary. The convergence of the manipulating variable is ensured by using the forward Euler method. The proposed controller has been tested using simulation and the results show satisfactory responses. The overshoot is completely absent and the response speed is very fast. it can be concluded that using the residual value of the back-EMF gives a better observer performance. Also, it can be concluded that a sensorless TSR control gives satisfactory dynamics to the WPGS. Also, it can be concluded that the proposed residue controller gives a satisfactory response and efficiency for wind speed estimation algorithm.

Moreover, a MPPT controller has been developed using hill climb technique. The PMSG has been controlled using SMC for the speed control loop and PI control for the d-axis and q-axis currents. The system has been analysed using speed estimation and speed measurement. The results shows better response when speed measurements are employed. However, both the controllers show satisfactory dynamics.

In addition, a comparison between the improved back-EMF, classical back-EMF and FIS speed estimators have been undertaken. The results clearly validate the accuracy of the improved back-EMF based on residue theorem.

Chapter 6

Maximum Power Point Tracking Controllers for Photovoltaic Energy Conversion System Using Sliding Mode Control

This chapter proposes a Maximum Power Point Tracking controller for photovoltaic system using sliding mode control scheme in stand-alone configuration. Two applications have been studied, i.e. using DC-DC boost converter and single-ended primary-inductor converter. The aim of this controllers is to achieve an optimum MPP operation without the need of atmospheric conditions measurements and to enhance the efficiency of the PV power system. The proposed controllers overcomes the power oscillation around the operating point which appears in most implemented MPPT techniques. Both proposed MPPT controllers have been developed in such a way that the sliding surface is set to be the MPP condition, so that the operating points converge to the optimum operating point. For DC-DC boost converter application, an adaptive SMC gain has been designed and implemented in the proposed controller

to allow the compensation of the uncertainty of ambient conditions. The results show a satisfactory operation of a PV power system and a better MPP achievement of the operating point to the optimal operating point.

As MPPT controller is necessary for PV power system to improve the energy conversion efficiency, the MPPT can be achieved by regulating the input voltage of the PV system. One of the power electronics converters objectives in PV system is to perform the MPP operation. There are several topologies of DC-DC converters. In the second application single-ended primary-inductor converter topology has been implemented and analysed. The complicity in controlling SEPIC has been simplified. The MPPT controller has been proposed using sliding mode control. The results show simple design and satisfactory operation with perfect MPP achievement.

6.1 Introduction

Photovoltaic energy which is one of the most promising sources of renewable energy, has received many attentions especially when the semiconductors and power electronics technology grown up. Recently, solar energy or photovoltaic energy applications are growing up mostly in stand-alone configuration. However, the poor efficiency and the non-linearity of the output characteristics limit the of PV power system applications. Variations on solar irradiance levels, ambient temperatures and dust accumulation on the surface of the PV panel affect the output of the PV system [122]. In addition, it has been noted, when assuming fixed cell efficiency there are three factors affect the maximum power extracted from the PV power system, i.e. ambient temperature, insolation and load impedance [123]. Due to these limitations, it becomes necessary to implement MPPT techniques to improve the efficiency which leads to a reduction in PV power system cost.

The aim of MPPT technique is to automatically obtain an optimal MPP

operation under variable atmospheric conditions. Several MPPT techniques have been developed for PV system. Incremental condition (IC) and perturbation and observation (P&O) algorithms were widely used in MPPT controller. The idea of those algorithms is quite similar. In P&O, the perturbation is made in the operating point till maximum power achieved. Where in IC, the P-V curve slope of the PV system is checked till it reaches zero at which MPP operation is achieved [122]. One other MPPT technique used for PV system is the constant voltage algorithm, in which the MPP operation achieved by keeping the ratio between the PV voltage at the maximum power and the open circuit voltage constant [124].

Although, the above discussed MPPT methods are widely used because of the ease of implementation and the independent of the atmospheric measurements, they still have some disadvantages. One of them is the power oscillation and around MPP which is caused by fixed perturbation step size. Another disadvantage is the confusion in the direction of tracking which is caused by rapidly changing in atmospheric conditions [125, 9]. [114] provides a solution of the fixed iteration size by introducing a variable iteration size varies according to the operating point.

One important stage of a PV power system is the DC-DC converter. There are several converter topologies, i.e. buck converter which step the voltage down, boost converter in which the voltage is stepped up and buck-boost converter which step up and down the voltage. A part from stepping the voltage up and down, DC-DC converter perfumes the MPP operation by regulating the input voltage to its MPP value. The SEPIC is one of the topologies which can perform both stepping up and down operations. Moreover, it benefits from a switch failure protection by providing a capacitive isolation [126]. In fact, as the input current ripple decreases the PV power system efficiency increases. The input current drawn by SEPIC has a minimum ripple since it uses a capacitor as main energy storage. Due to the construction of SEPIC, the polarity

of the input and output voltages are the same. SEPIC is preferred for battery charging system since the diode is placed at the output which can prevent the battery current going to PV source [126].

Recently, sliding mode control has received many attentions because of its benefits of a quick response and robustness [127]. SMC can be defined as a variable structure control strategy based on feedback and high frequency switching control [28]. SMC has many advantages such as insensitivity to system parameter changes, disturbance and load variations [29]. Achieving the design of a stable sliding surface and obtaining an optimum design of a control low, which forces the operating points to reach a predetermined surface in finite time, are the two main stages of SMC design [85]. Sliding mode controller requires maintaining a constant gain so that a robust and finite time convergence of the sliding boundary is achieved. Despite of those advantages, the uncertainty of state variable could not be compensated when using a constant gain, which might introduce a steady-state error [64, 65, 127].

Although SMC has been implemented to PV power systems [128, 129, 130], there may be a lack of robustness due to the use of reference current. Similar approach has been reported in [131] where the sliding surface has been selected to follow the incremental condition. However, the SMC gain was set to be a constant which may lead to steady-state errors and may reduce the energy conversion efficiency.

6.2 PV Power System and Characteristics

6.2.1 PV Power System

The PV power system implemented in this research consist of PV panel, with a rated power of 85 W at ambient temperature of 25 C and a solar irradiance of $1000W/m^2$, connected to a stand-alone load through DC-DC boost

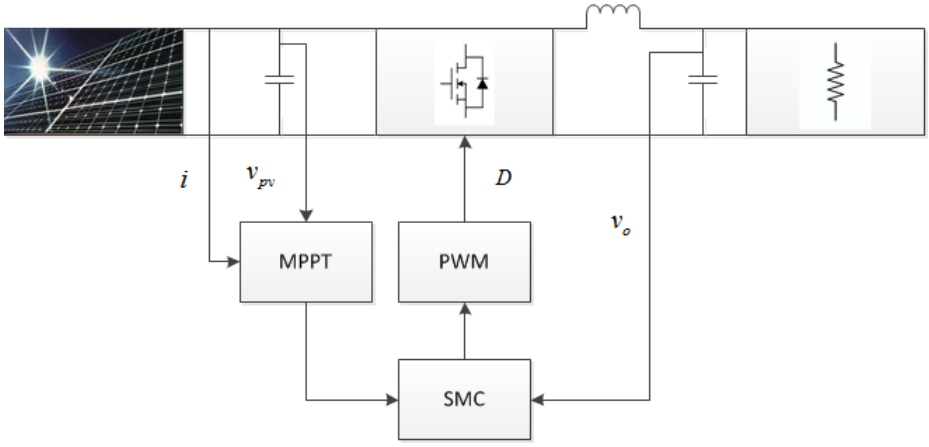

Figure 6.1: Implemented PV system and control diagram using boost converter.

converter. The boost converter has been designed to operate at continuous conduction mode. Figure 6.1 illustrates the implemented PV power system and the control diagram.

6.2.2 PV Characteristics

A PV module is a combination of series and parallel solar cells which generate voltage and currents. In darkness, PV cell only generates currents as it becomes a p-n junction diode [122]. In order to simulate the behavior of PV system a mathematical model has been developed based on the equivalent circuit of a solar cell. Figure 6.2 illustrates the equivalent circuit of a solar cell, where I_{ph} is the photocurrent of the cell, V_{pv} and I_{pv} are the PV voltage and current respectively.

The series resistance (R_s), which is very small, and the shunt resistance (R_{sh}), which is very large, both can be neglected to simplify the model [132, 133]. The PV Panel can be described as the following [134, 133]:

$$I_{pv} = I_{ph} - I_{sat}\left[\frac{q(V_{pv} + I_{pv}R_s)}{AkT - 1}\right], \tag{6.2.1}$$

$$I_{ph} = \frac{\lambda}{1000}\left[I_{sc} + K_I(T - 25)\right], \tag{6.2.2}$$

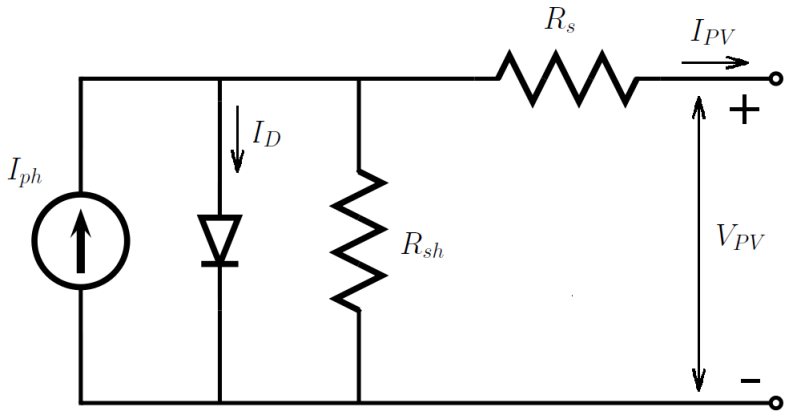

Figure 6.2: Equivalent circuit of a solar cell

where q is the charge of an electron ($1.602 \times 10^{-19}C$), λ is solar irradiance, A is the idealist factor of a p-n junction (1 or 2), k is the Boltzmans factor ($1.381 \times 10^{-23}J/K$), T is the temperature of the cell array and I_{sc} and K_I are the short-circuit current and the short-circuit current temperature respectively. The output power voltage characteristics of the PV panel as functions of solar irradiance is shown in Figure 6.3. The P-V curve illustrates the effect of the solar irradiace on the PV panel operation. It is also shown that the maximum power can be achieved at fixed voltage of approximately 17 volts. Another important characteristics analysis is the current-voltage curve of the PV panel which is shown in Figure 6.4. The I-V curve indicates the capability of the PV panel at different atmospheric conditions, i.e. solar irradiance. Also, the curve shows that the fixed voltage operation can ensure a maximum power conversion operation under different solar irradiance.

From the P-V and I-V characteristics curves, it can be concluded that in order to achieve a maximum power operation at different solar irradiance the operated voltage must be constant. This can be a simple solution for PV panel control. In terms of high efficiency operation the voltage can be varied slightly according to the solar irradiance to improve the efficiency.

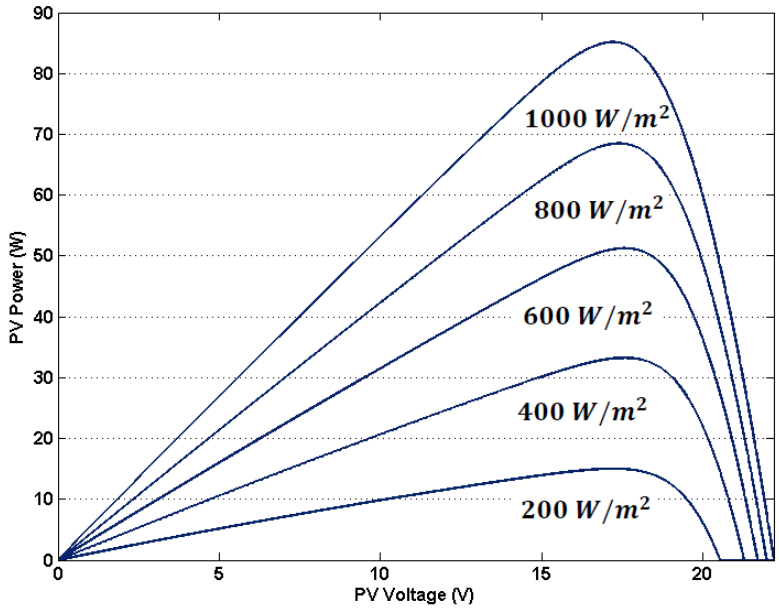

Figure 6.3: Power-Voltage curve of the PV panel.

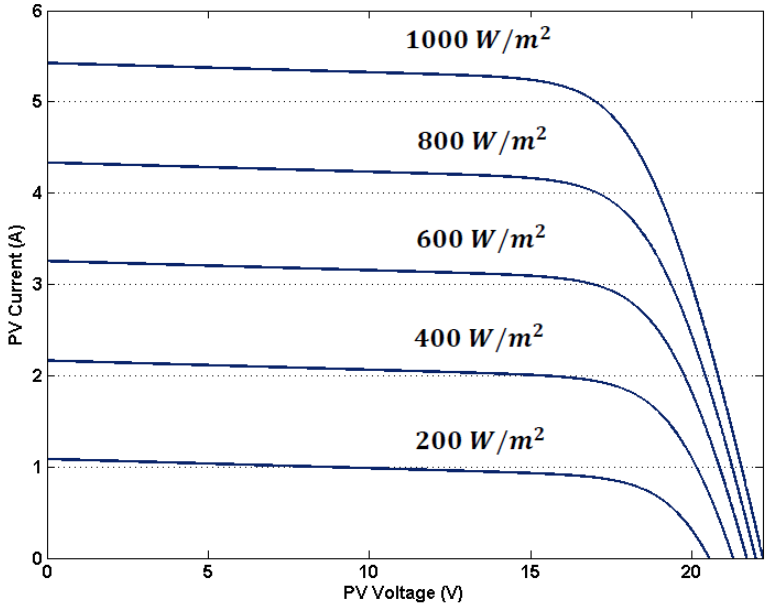

Figure 6.4: Current-Voltage curve of the PV panel.

6.3 Sliding Mode MPPT Controller Using DC-DC Boost Converter

6.3.1 DC-DC Boost Converter

DC-DC boost converter is a type of converters used in applications that require an output voltage to be higher than input voltage. The DC-DC boost converter consists of an IGBT switch, a diode and passive components that are capacitor (C), Inductor (L) and resistance (R). The boost converter operation consists of two states: ON state in which the IGBT switch is fired and OFF state in which the switch is turned off. The following equations describe the DC-DC boost converter operations [122]:

ON STATE

$$L\frac{di_L}{dt} = V_{pv}, \tag{6.3.1}$$

$$C\frac{dv_o}{dt} + \frac{V_o}{R} = 0. \tag{6.3.2}$$

OFF STATE

$$L\frac{di_L}{dt} + V_o = V_{pv}, \tag{6.3.3}$$

$$i_L - C\frac{dv_o}{dt} - \frac{V_o}{R} = 0, \tag{6.3.4}$$

The ratio of the ON and OFF times to the operation time can be modulated using several techniques and called pulse width modulation (PWM). The duty ratio (D) which is the control signal is compared to a triangular pulse. In fact, the control of boost type DC-DC converter is more difficult than the Buck type DC-DC converter. The difficulties come from the appearance of the control input in both voltage and current equations [135].

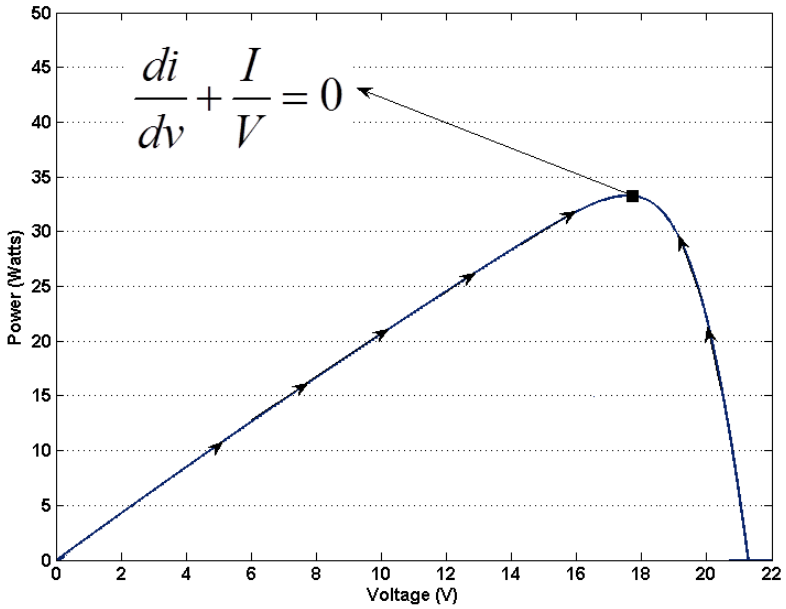

Figure 6.5: Condition of maximum power, illustration based on solar irradiance of $400W/m^2$.

6.3.2 Controller Design

MPP operation is important for PV power system to accumulate the poor efficiency of the energy conversion. The principle of the proposed MPPT controller can be illustrated in Fig.6.5. The SMC controller will force the operating point to lie in a point at the top of the curve where the condition of maximum power is achieved.

The sliding surface has been selected to be the condition at which the MPP occurs and the controller design equations can be shown as the following:

$$s = e \qquad \dot{s} = 0, \tag{6.3.5}$$

$$e = \frac{di}{dv} + \frac{I}{V}, \tag{6.3.6}$$

$$\dot{s} = \frac{d^2i}{dv^2} + \frac{di}{dv}. \tag{6.3.7}$$

By solving the DC-DC boost converter equations 6.3.1 and 6.3.3 with respect to the ON and OFF states, the rate of change of inductor current (I_L) and the output voltage (V_o) can be shown as follows:

$$\frac{di_L}{dt} = \frac{V_{in} - (1-D)V_o}{L}, \tag{6.3.8}$$

$$\frac{dv_o}{dt} = \frac{(1-D)I_L}{C} - \frac{V_C}{RC}. \tag{6.3.9}$$

The rate of change of inductor current with respect to the output voltage can be calculated by dividing the above two equations as bellow:

$$\frac{di_L}{dv_o} = \frac{C}{L}\left[\frac{V_{in} + RI_L(1-D)^2}{(1-D)I_L} - \frac{V_o}{I_L} - \frac{RV_{in}}{V_o}\right]. \tag{6.3.10}$$

Rearranging (6.3.10), the equivalent part of the SM controller can be represented in (6.3.11).

$$u_{eq} = D^{eq} = \left[\frac{L}{RC}\frac{d^2i}{dv^2} - \frac{L}{C}\frac{V_{in}}{V_o} + 1\right]. \tag{6.3.11}$$

From (3.2.6) and (3.2.8) the proposed MPPT SM controller design can be demonstrated in (6.3.11) as follows:

$$u = \left[\frac{L}{RC}\frac{d^2i}{dv^2} - \frac{L}{C}\frac{V_{in}}{V_o} + 1\right] - k_a sgn(e). \tag{6.3.12}$$

The SMC gain (k_a), which is designed to be adaptive, is an important factor to insure the SMC stability. Since the capability of the PV panel strongly depend on the atmospheric conditions, the SMC gain has been designed to be dependent on the capability of the PV current. The variation of k_a follow a fourth order polynomial function which is presented below:

$$k_a = P_1x^4 + P_2x^3 + P_3x^2 + P_4x + P_5, \tag{6.3.13}$$

where $P_{1..4}$ are the polynomial coefficients, that are obtained using curve-fitting and are defined in Table 3.1, and x is the inductor current. Figure 6.6 demonstrate the SMC adaptive gain varies as the solar irradiance vary from 1000 to $400W/m^2$.

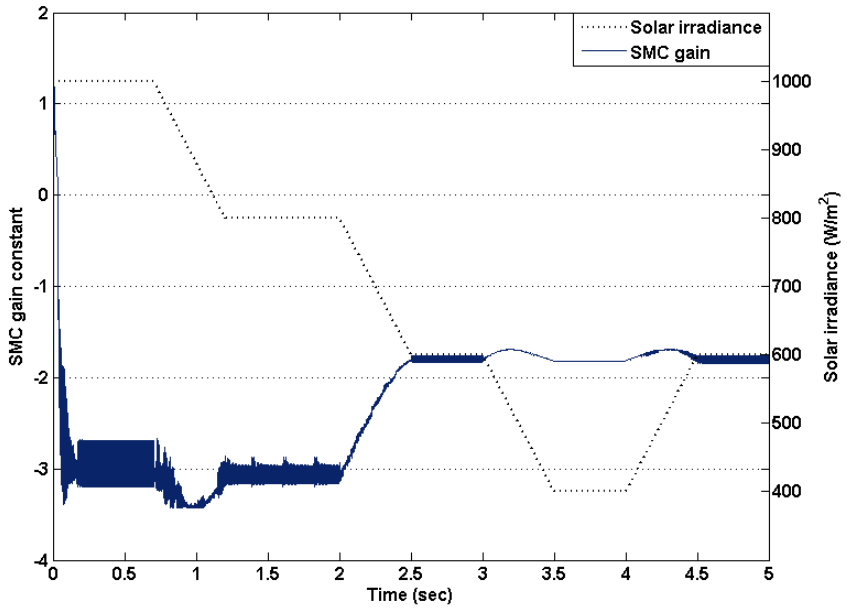

Figure 6.6: Variation of SMC adaptive gain over a range of solar irradiance

The stability of a sliding mode controller can be verified by the Lyapunove equation which is illustrated in 6.3.14. This condition ensures the convergence of the operating point to the sliding surface [88].

$$s.\dot{s} \prec 0. \tag{6.3.14}$$

For the PV system to be stable, k_a should meet the following condition [90].

$$\left[\frac{L}{RC}\frac{d^2i}{dv^2} - \frac{L}{C}\frac{V_{in}}{V_o} + 1\right] > k_a. \tag{6.3.15}$$

By analyise the above equation, the second order differentiation term can be neglected. Since the voltage ratio term is equal to $(1 - D)$, equation 6.3.15 can be as follows:

$$-\frac{L}{C}(1 - D) + 1 > k_a. \tag{6.3.16}$$

By substituting the values of the passive components and assuming the worst case condition, which occurs when D is zero, the stability and MPP achievement are ensured when $0.787 > k_a$. Figure 6.6 verify the SMC stability and

Table 6.1: PV Panel Specifications and Polynomial Coefficients

Description	Symbol	Value	Unit
PV Panel Specifications			
Maximum Power	P_{max}	85.2	W
Voltage at MPP	V_{mpp}	17.2	V
Current at MPP	I_{mpp}	4.95	A
Open circuit voltage	V_{oc}	22.2	V
Short circuit current	I_{sc}	5.45	A
Solar irradiance	–	1000	W/m^2
Ambient temperature	T	25	$°C$
Polynomial Coefficients			
Polynomial Coefficient 1	P_1	0.2629	-
Polynomial Coefficient 2	P_2	-3.049	-
Polynomial Coefficient 3	P_3	12.35	-
Polynomial Coefficient 4	P_4	-20.96	-
Polynomial Coefficient 5	P_5	10.89	-

shows that the SMC gain satisfy the stability condition during the variation of the atmospheric conditions.

6.3.3 Simulation Results and Analysis

The control diagram of the proposed MPPT SM controller for PV power system is shown in Fig.6.1. The measurements are the PV voltage and current as well as the output voltage. The PV power system has been modelled and simulated using MATLAB/SIMULINK and the PV panel specifications are shown in Table 6.1. The model has been simulated at different solar irradiance (from 1000 to $400W/m^2$).

Figure 6.7 shows the maximum power extracted from the PV power system.

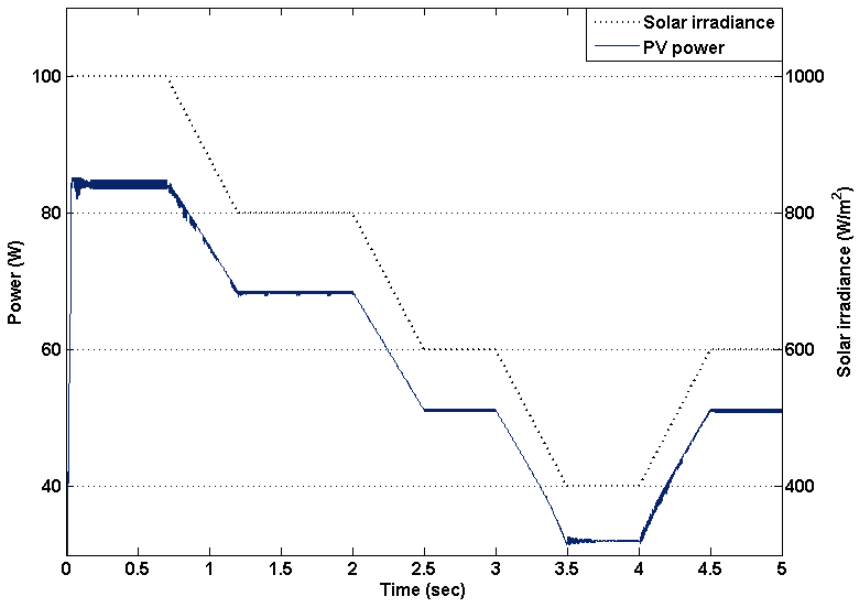

Figure 6.7: Output PV power using SMC over a range of solar irradiance.

It is clearly shown that the power is at maximum with no overshoot. The response time is fast enough and the chattering is at minimum. For all the range of solar irradiance the proposed SM controller forces the operating point to lie on maximum possible point of the curve.

The PV voltage, which is illustrated in Fig.6.8, shows a perfectly constant operation during different atmospheric conditions. It is noticeable from the figure that the value of the PV voltage matches the PV specification value which clearly indicate a MPP operation.

Figure 6.9 shows the PV current. Although, the effect of atmospheric variation is clearly shown in the PV current, the SM controller forces the system to draw maximum possible current to achieve a MPP operation. The chattering effect is at minimum and reduces as the solar irradiance decreases.

In order of evaluating the proposed MPPT controller based on SMC, a comparison analysis with classical incremental condition (IC) has been undertaken. Figure 6.10 illustrates the PV output power during variations of solar

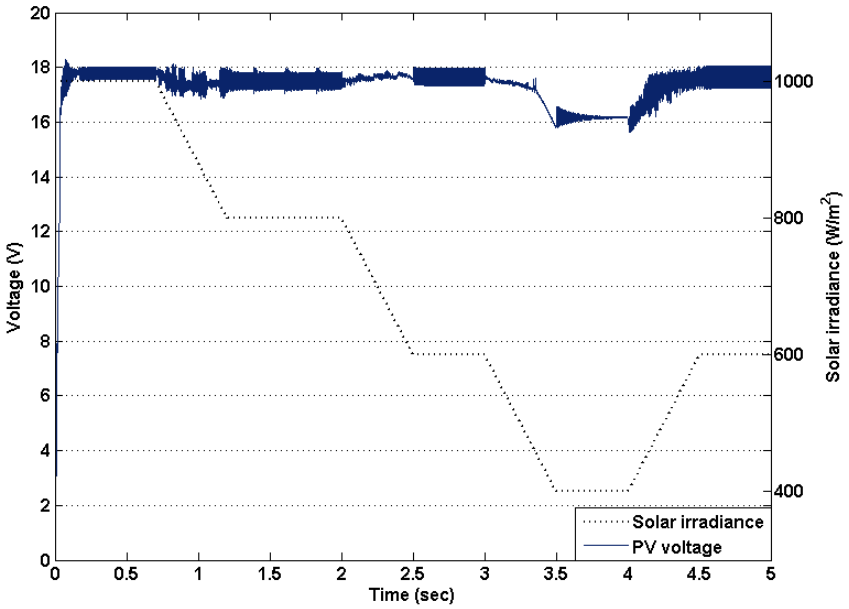

Figure 6.8: PV voltage using SMC over a range of solar irradiance.

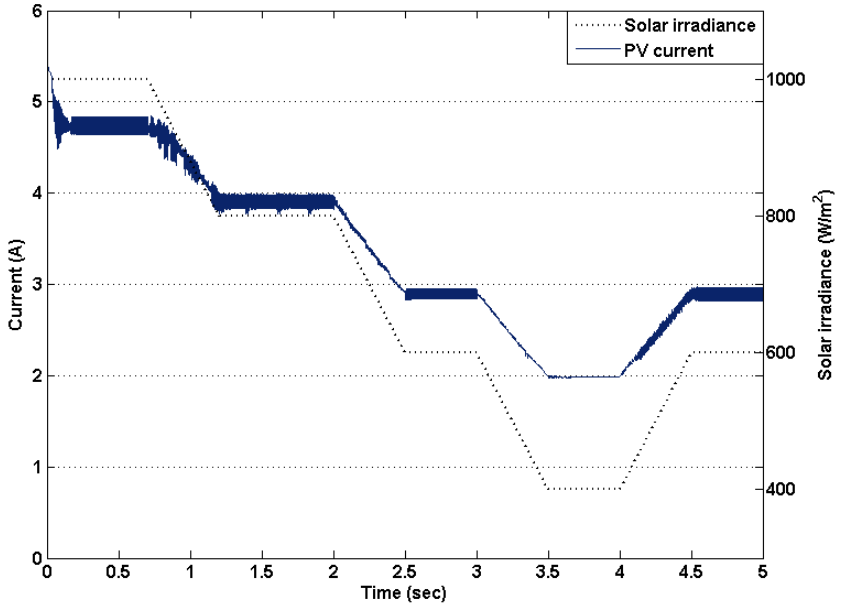

Figure 6.9: PV current using SMC over a range of solar irradiance.

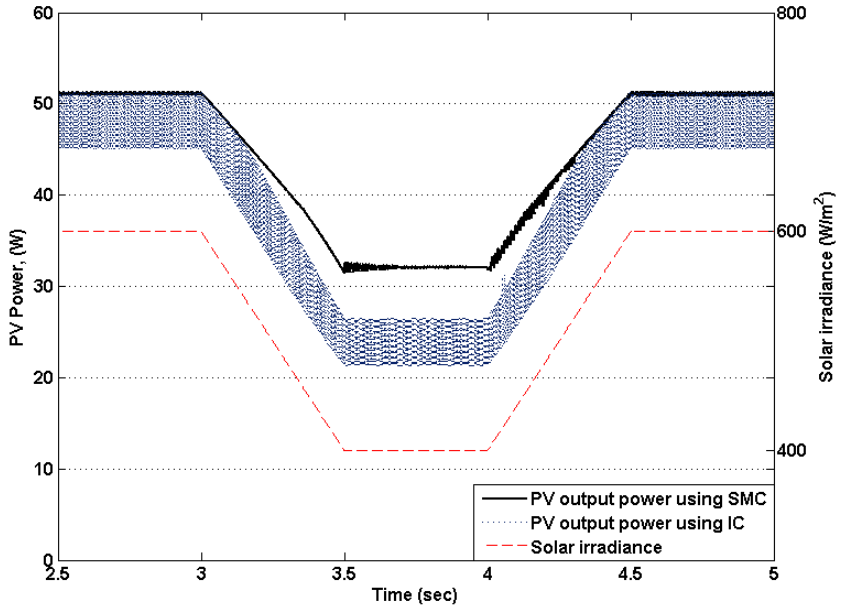

Figure 6.10: Comparison between proposed SMC and incremental condition algorithm.

irradiance. The high oscillations around the reference point are clearly shown in the output power using IC. The improvement in the PV output power is significant when using the proposed SMC.

6.4 Sliding Mode MPPT Controller Using Single Ended Primary Inductor Converter

6.4.1 Single Ended Primary Inductor Converter Analysis

The single-ended primary-inductor converter (SEPIC) is able to perform both buck and boost converters operations without reversing the output voltage polarity, and with minimum input current ripple which improves the aver-

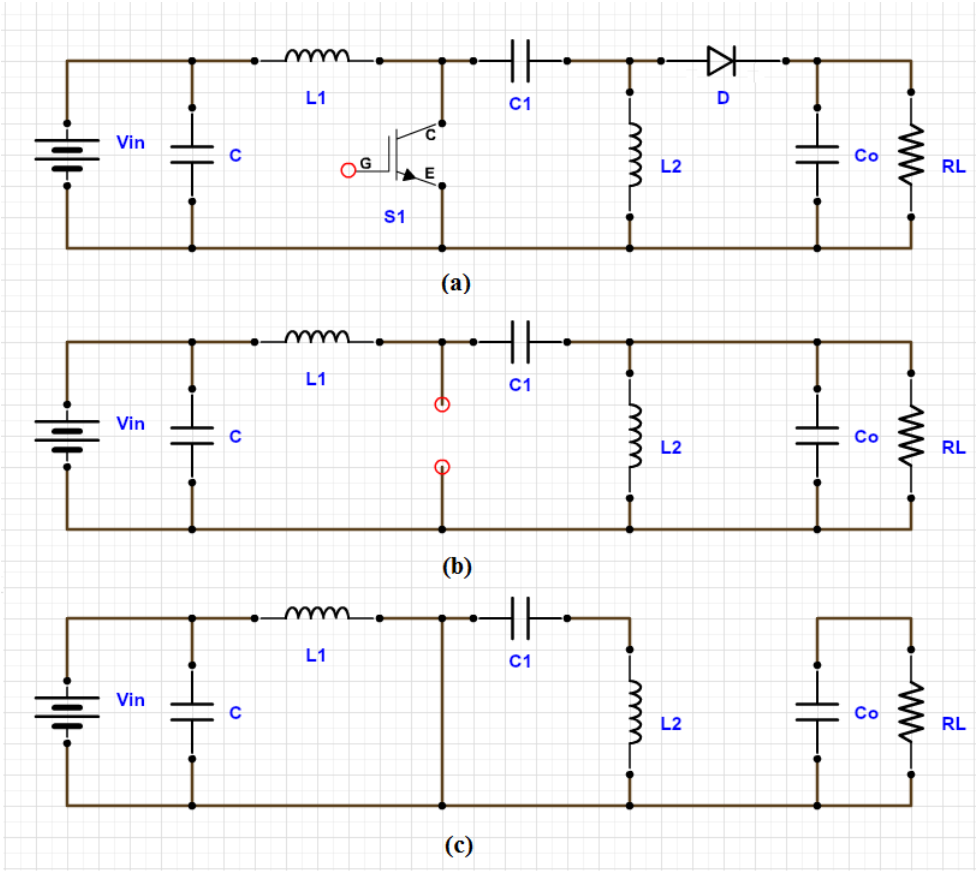

Figure 6.11: (a) SEPIC configuration, (b) Switch is OFF and (c) Switch is ON.

age value of voltage and current. SEPIC consists of an IGBT switch (S_1) and a diode (D) which is placed in the output stage, two capacitors (C_1 and C_o) and two inductors (L_1 and L_2). The energy is exchanged between the inductors and capacitors to allow the SEPIC to convert the voltage from one level to another. The coupling capacitor (C_1), which is connected in series, must have a voltage rating higher than the input voltage to allow the energy transfer from input to output [136]. The construction of the SEPIC is illustrated in Fig.6.11 including the two stages of operation that are when the switch is OFF (b) and ON (c). The state space representation of SEPIC can be as the following:

ON STATE

$$L_1 \frac{di_1}{dt} = V_{in}, \tag{6.4.1}$$

$$C_2 \frac{dv_o}{dt} + \frac{V_o}{R} = 0, \tag{6.4.2}$$

OFF STATE

$$L_1 \frac{di_1}{dt} + V_{c1} + V_o = V_{in}, \tag{6.4.3}$$

$$i_1 - i_2 - C_2 \frac{dv_o}{dt} - \frac{V_o}{R} = 0. \tag{6.4.4}$$

By averaging the two states and introducing PV panel as input source and D is the duty cycle, the averaged state space equations can be demonstrated as follows:

$$L_1 \frac{di_1}{dt} = V_{in} - \left[(V_{c1} + V_o) \left(\frac{(1-D)}{D} \right) \right], \tag{6.4.5}$$

$$C_o \frac{dv_o}{dt} = (i_1 - i_2) \left(\frac{D}{(1-D)} \right) - \frac{V_o}{R}. \tag{6.4.6}$$

It is worth to note that the issue with SEPIC construction is that the two inductors and coupling capacitor are forming a resonant circuit. So, to stand voltage to be twice the input voltage which is undesired for such application, a series resistance is connected. To overcome that is to design a SEPIC that has the inductors coupled. So we got two windings coupled to the same core. Hence, the SEPIC is restricted with the fact that the two inductors must be at a same value.

6.4.2 Controller Design

As discussed previously, the MPPT operation is important for PV power system in order to overcome and enhance the poor energy conversion efficiency. The proposed MPPT controller controls the SEPIC duty ratio so that the

optimum operating condition is achieved. The sliding surface has been selected to be the condition at which the MPP achieved and it is illustrated in Fig. 6.5.

The proposed MPPT controller design equations can be shown as the following:

$$s = e \quad \Rightarrow \quad \dot{s} = 0, \tag{6.4.7}$$

$$e = \frac{di}{dv} + \frac{I}{V} \quad \Rightarrow \quad \dot{s} = \frac{d^2i}{dv^2} + \frac{di}{dv}, \tag{6.4.8}$$

By solving the averaged SEPIC equations (6.4.5) and (6.4.6), the rate of change of inductor current with respect to the PV voltage can be shown as below:

$$\frac{di}{dv} = \left[\frac{1-D}{D}\right]^2 \left[\frac{C(V_C+V_o)}{L(I_1-I_2)}\right] + \left[\frac{1-D}{D}\right] \left[\frac{CV_{in}}{L(I_1-I_2)} + \frac{RC(V_C+1)}{L}\right] - \left[\frac{RCV_{in}+1}{V_o}\right], \tag{6.4.9}$$

From the above equation, the term $\left[\frac{1-D}{D}\right]^2 \left[\frac{C(V_C+V_o)}{L(I_1-I_2)}\right]$ consists of two parts. The first part is very small and squared. For the second part, during transients the rate of change of the inductor current is high so that I_2 can be much greater than I_1. This fact means the second part is tends to have a very small value during transients. Hence, this term has no significant effect and can be neglected. By rewriting (6.4.9), the rate of change of the inductor current with respect to PV voltage can be shown as follows:

$$\frac{di}{dv} = \left[\frac{1-D}{D}\right] \left[\frac{CV_{in}}{L(I_1-I_2)} + \frac{RC(V_C+1)}{L}\right] - \left[\frac{RCV_{in}+1}{V_o}\right], \tag{6.4.10}$$

By substituting (6.4.10) to (6.4.8),

$$\dot{S} = \frac{d^2i}{dv^2} + \left[\frac{1-D}{D}\right] \left[\frac{CV_{in}}{L(I_1-I_2)} + \frac{RC(V_C+1)}{L}\right] - \left[\frac{RCV_{in}+1}{V_o}\right], \tag{6.4.11}$$

The equivalent part of the controller can be shown as the following:

$$U_{eq} = \left[\frac{D}{1-D}\right]^{eq} = -\frac{d^2v}{di^2} \frac{C\left(V_{in} + RV_C(I_1-I_2)\right)}{L(I_1-I_2)}, \tag{6.4.12}$$

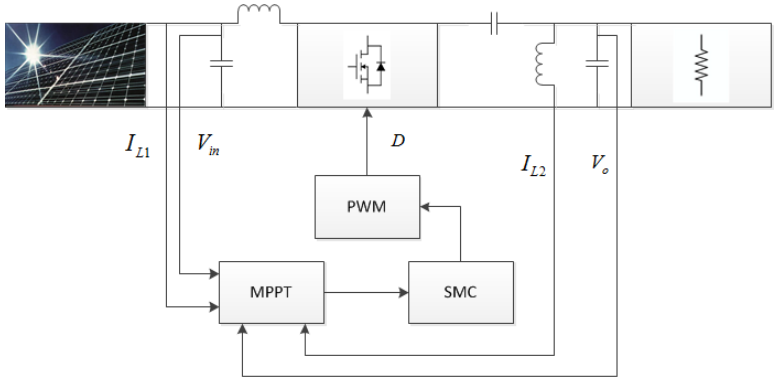

Figure 6.12: The investigated PV power system with the control block diagram.

The structure of the proposed SM MPPT controller can be achieved by substituting (6.4.12) to (3.2.6) and can be represented in (6.4.13).

$$\frac{D}{1-D} = -\frac{d^2v}{di^2}\frac{C\left(V_{in} + RV_C(I_1 - I_2)\right)}{L(I_1 - I_2)} + Ksgn(e). \tag{6.4.13}$$

6.4.3 Simulation Results and Analysis

The Investigated PV power system consists of the followings: a PV panel which has a rated power of $85W$ at an ambient temperature of $25\,^{\circ}\mathrm{C}$ and a solar irradiance of $1000W/m^2$, DC-DC SEPIC and a stand-alone resistive load. Figure 6.12 demonstrates the investigated PV power system and the control block diagram.

The specifications of the PV panel are shown in Table 6.1 where, the SEPIC components values are illustrated in Table 6.2. The PV power system has been modelled and simulated using MATLAB/SIMULINK under a range of solar irradiances (from 1000 to $400W/m^2$).

Figure 6.13 illustrates the PV output power. The amount of extracted power indicates the achievement of maximum power operation. The effect of SEPIC operation, i.e. minimum ripple current, improves the PV power system efficiency which leads to approach a maximum possible energy conversion. It

Table 6.2: SEPIC components values.

Description	Symbol	Value	Unit
SEPIC Components Values			
Inductors	L_1, L_2	250	mH
Capacitors	C_1, C_o	47	μF
Resistance	R_L	100	Ω
Switching frequency	f	20	kHz

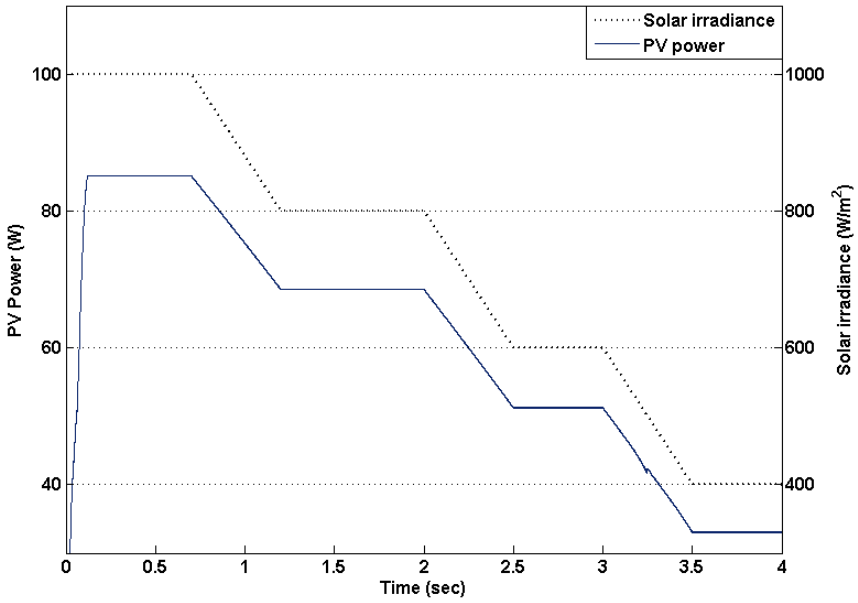

Figure 6.13: PV output power during solar irradiance variations.

is clearly shown that the output power is smooth and the respond time is fast enough.

The constant voltage operation is demonstrated in Fig. 6.14. It is noticeable that the voltage fluctuates around the maximum rated voltage and slightly increases as the solar irradiance decreases since the current capability of the PV panel decreases as the solar irradiance decreases. Hence, the operation

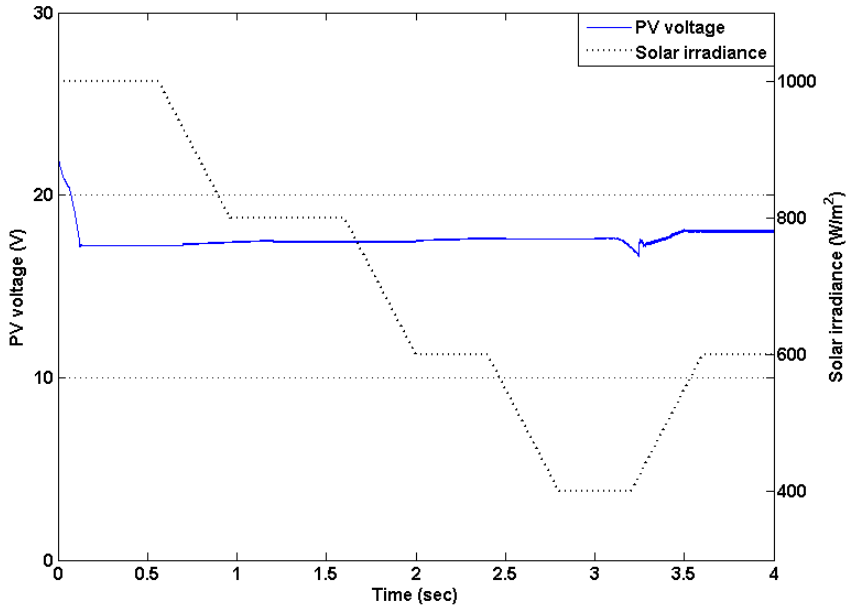

Figure 6.14: PV voltage during variations of solar irradiance.

indicates a stable operation and a perfect achievement of MPP operation. It is clearly shown that the voltage level changes from the open circuit voltage level to rated MPP voltage in perfect time. Also, a stable operation is indicated during atmospheric conditions changes.

The inductor current which is illustrated in Fig. 6.15 shows a smooth and almost ripple-free operation. The current level changes when a solar irradiance changes as the current is dependent on the atmospheric conditions. The stability of the PV system is noticeable as well as the achievement of MPP operation.

The analysis of the operating points is shown in Fig. 6.16. The figure indicates the achievement of the proposed controller to the MPP operation. It clearly shows the location of the operating point on the P-V characteristics of the PV module.

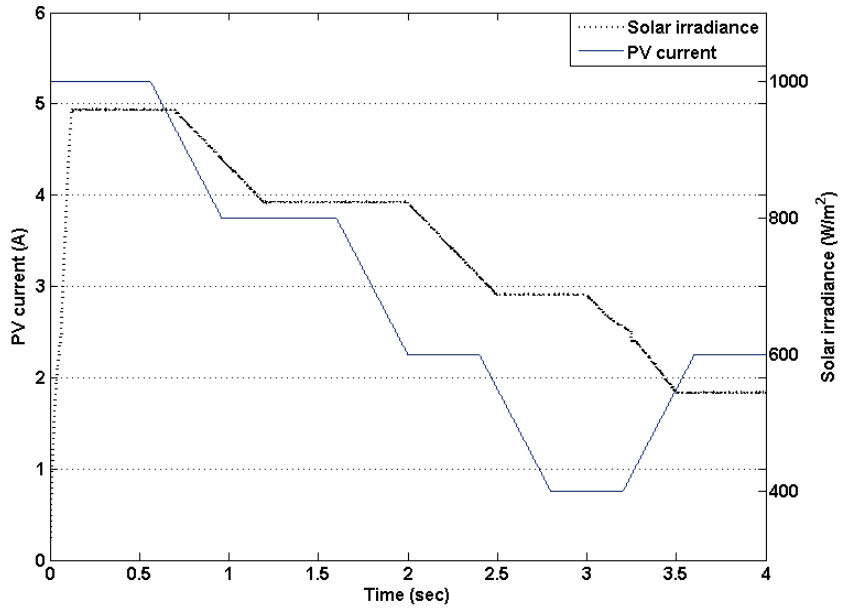

Figure 6.15: The drawn current from the PV power system during variant solar irradiances.

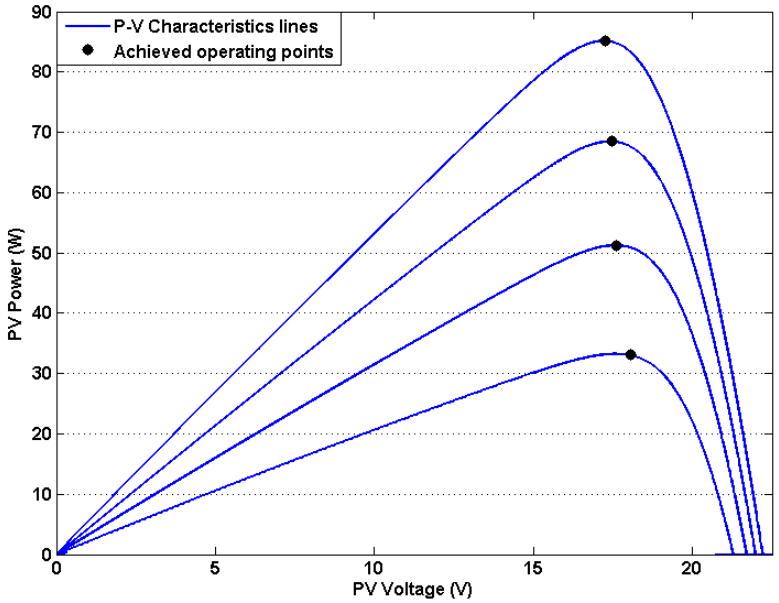

Figure 6.16: The achieved operating point of the proposed controller.

6.5 Comparison Analysis between Boost converter and SEPIC

The single-ended primary-inductance converter is a DC/DC-converter topology that provides a positive regulated output voltage from an input voltage that varies from above to below the output voltage. But in terms of circuit construction, the DC-DC boost converter is much simple in design and uses less passive component which makes the size smaller. The PV power output are shown in Figure 6.17. It can be clearly shown that the output power when using SEPIC converter is a bit higher and with less distortion. Figure 6.18 demonstrate the PV voltages using the two different power converter topologies. It can be shown that for both topologies the constant voltage operation have been achieved. The drawn PV currents are illustrated in Figure 6.19. It can be noted that the SEPIC has drawn a ripple free current. However, the output PV current using boost converter is still in range. Overall, it is worth to deduced that the performance and the electrical conversion efficiency of PV system can be improved using SEPIC.

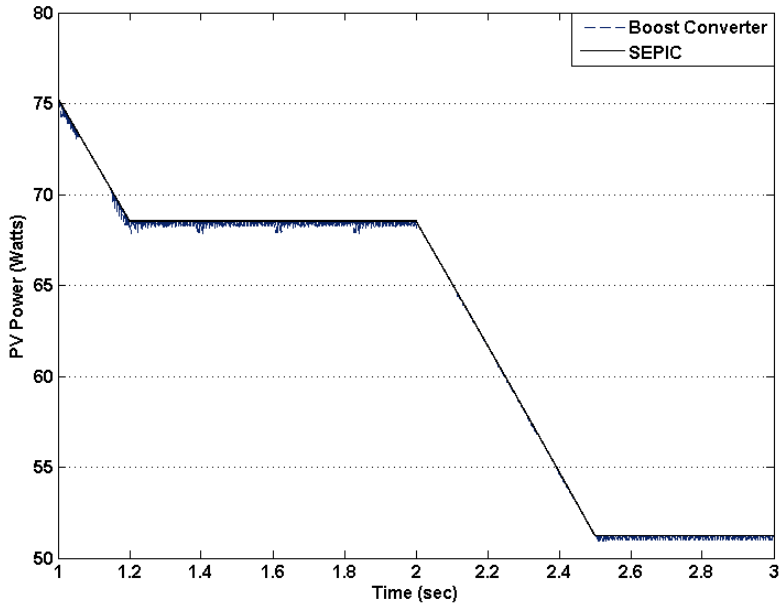

Figure 6.17: The PV power using Boost converter and SEPIC.

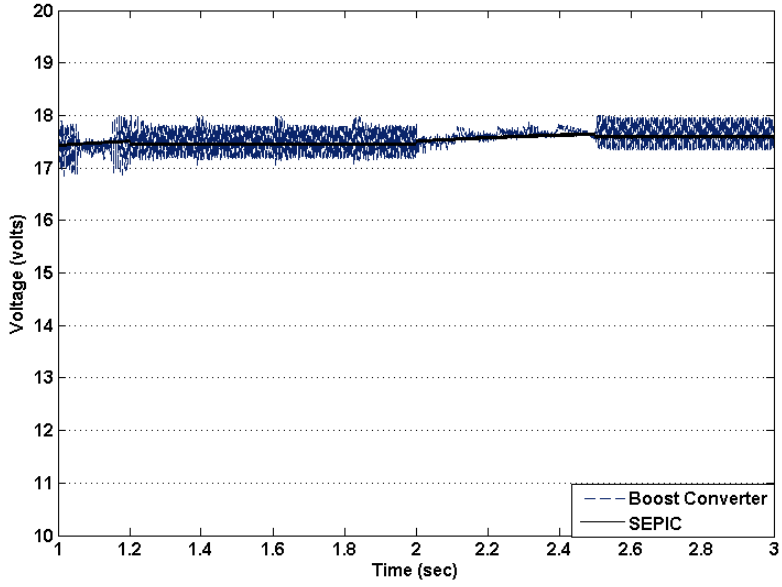

Figure 6.18: The PV voltage using Boost converter and SEPIC.

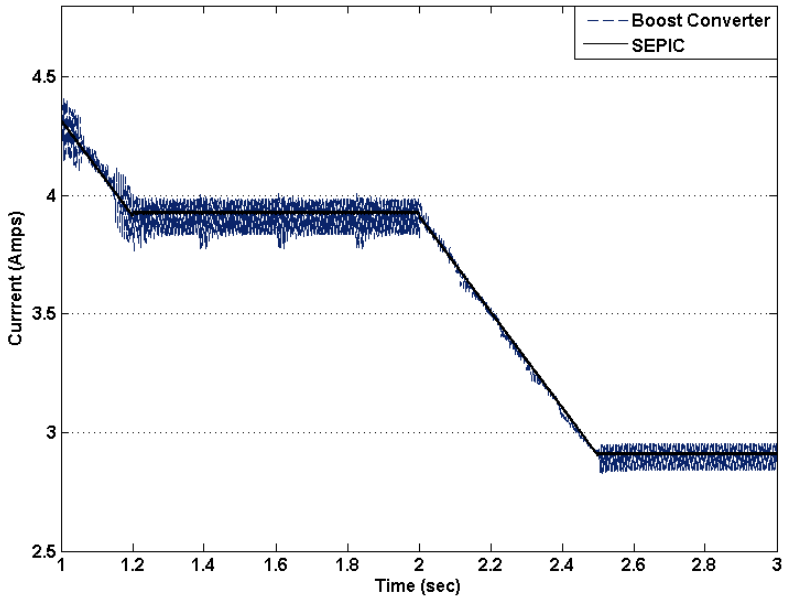

Figure 6.19: The PV current using Boost converter and SEPIC.

6.6 Conclusion

In this chapter, a PV panel which is connected to a stand-alone DC load through a PWM controlled DC-DC converter has been employed to investigate the responses of SMC controllers. The MPPT controllers have been designed, simulated and tested based on SMC scheme. The objective of the controller is to force the operating point to be at maximum during the variation of the atmospheric conditions. The proposed controllers have been designed to follow an incremental condition so that the controller searches for the optimal operating point automatically which means the proposed controllers are independent of the atmospheric condition measurements.

Two applications have been studied in this chapter with different DC-DC converter topologies, that are DC-DC boost converter and SEPIC. Both of them have been implemented, analysed and tested. DC-DC boost converter which is commonly used in such application has been controlled using SMC.

The SMC gain set to be adaptive so its value vary as the atmospheric conditions changes. The simulation results shows perfect achievement of the operating point to MPP operation with satisfactory constant voltage operation. It can be concluded that MPPT controller using SMC for PV power system improves the extracting power efficiency and overcomes the poor efficiency and the mismatching of the widely used MPPT algorithms. Moreover, it can be deduced that using an adaptive gain for a SM controller can improve the behavior and response of the PV power system compared with that using a constant gain.

Moreover in this chapter, the implementation of a SEPIC in PV power system has been investigated. Also, a MPPT controller has been developed using sliding mode control. The sliding surface of the proposed controller has been selected to be the incremental condition so that there is no requirement of a reference current. It can be deduced that SEPIC improves the operation of the PV power system because of the ability of the converter to draw a ripple free current. The SEPIC controller has been optimized and simplified for ease of implementation. It can be concluded that using a SMC for MPPT SEPIC controller improves the efficiency of PV power system and ensures the achievement of the operating point to the MPP operation without the need of atmospheric measurements.

Finally, the two applications have been compared and the comparison prove that using SEPIC converter can increase the conversion efficiency. On the other hand the boost converter is a cost effective. According to the literature review provided in this chapter, it can be deduced that the issues of implementing SEPIC converter to PV system have been solved using SMC.

Chapter 7

Conclusions and Future Work

In this chapter, the findings described in this thesis are summarised, and, some future research directions are suggested.

7.1 Summary

In this thesis, the PMSG-based WPGS were modeled. The power in the wind was studied and the PMSG presented in the *abc* stationary reference frame. The electrical model was discussed in both the $\alpha - \beta$ reference frame and the $d-q$ rotating reference frame, implementing Clarke and Park transformations. The mechanical model of the PMSG was studied and the linearised PMSG model illustrated. In addition, the classical control of PMSG-based WPGS was discussed. The dynamic performance of the PMSG-based WPGS was simulated and analysed using classical PI controllers. The cross coupling between the d-axis and q-axis was removed by adding decoupling voltages. The poor performance of the PMSG-based WPGS using PI controllers was discussed. The results indicated low energy conversion ratio and high overshoot errors. The study found it is necessary to use a more advanced control system to improve the energy conversion ratio and the dynamic performance of small-scale PMSG-based WPGS.

Sliding mode control theory was explained and implemented in WPGS. Different MPPT controllers were proposed using SMC, i.e. direct and indirect speed controllers. The dynamic performance of the WPGS using sliding mode control has shown improved dynamic performance, overshoot errors elimination and higher energy conversion ratio, compared to the widely implemented PI control. The steady state errors and the ability of SMC gain to compensate the uncertainty during rapid wind variations, were argued in the literature review. The study found that, the limitation is overcome by introducing an adaptive gain for sliding mode MPPT controllers. Also, the indirect speed controller based on SMC was found to be a cost efficient solution for small-scale PMSG-based WPGS.

A new MPPT control approach has been developed for PMSG-based WPGS. The developed control approach can be adapted to non-linear systems since it can compensate these system uncertainties. The idea is to generate a soft dynamic controlled boundary implementing the mathematical residue theorem and to control the operating point to lie on a point inside the controlled boundary. The operating point represents the reference maximum power operation point. The developed soft dynamic boundary control approach overcame some major drawbacks of the commonly used control strategies, in terms of handling uncertainties, eliminating overshoot and steady states errors and robustness. The experimental verification was provided and the control approach validated. According to the obtained results, the study found an improvement in the energy conversion ratio of 2.5%. The study also demonstrated improvement in the small-scale PMSG-based WPGS dynamic performance when using the proposed control strategy.

Based on the new control approach, an improved back-EMF observer was proposed. The observer has been developed using the residual value of the back-EMF. As the investigated WPGS operates at low speed, it was argued in the literature that the classical back-EMF observer has poor performance

at low speed operation. The obtained result from the study shows that the performance of the back-EMF observer using residual back-EMF values was improved. A better performance and more accurate speed estimation were achieved than with the classical back-EMF observer, especially at low speed. By using the developed improved back-EMF observer, a sensorless MPPT TSR controller was developed. Also, a direct wind speed estimation using the generated power was proposed and implemented, which is a solution for wind speed measurement issues. The result illustrated improved sensorless operations, with simple MPPT control design, which are cost efficient controllers for small-scale WPGS.

In this thesis, rotor and wind speed estimations were proposed using a fuzzy inference system. The developed fuzzy estimators can provide accurate estimations for the rotor speed at low-speed operations and can perfectly estimate the instantaneous value of the wind speed. The fuzzy inference system estimators were developed using the torque component of the permanent magnet synchronous generator current. The performance of the fuzzy rotor speed estimator was compared to the classical and the improved back-EMF observers. The study found that the improved back-EMF speed observer had a better and more accurate performance, as well as evedencing that the improved back-EMF is simply structured and easy to implement.

Finally, a photovoltaic power conversion system was investigated. Sliding mode control was implemented in the MPPT controller for the PV power system. According to the argued issues in implementing MPPT algorithms and atmospheric condition measurement, covered in chapter 1, a dynamic sliding surface was proposed to overcome the argued drawbacks. This surface ensures the maximum power operating point and does not require atmospheric condition measurements. Additionally, a new application of single-ended primary inductor converter in PV power systems was investigated. The difficulties of the controller design were simplified using sliding mode control with a dy-

namic sliding surface. A comparison between the boost converter and SEPIC applications was undertaken. The study found an improvement in the energy conversion ratio when employing SEPIC.

7.2 Future Research Work

The recommendations for further investigation arising from this thesis can be listed as below:

- Implementation of the proposed sliding mode controllers to a real PMSG-based WPGS, so that, a comparison between the results obtained in this thesis and results from a real WPGS can be undertaken.
- The adaptive sliding mode gains can be further investigated and implemented in a real WPGS. The aim is to improve the system dynamic performance without changing the discontinuity nature of SMC, so that the ultimate robust behavior of SMC is ensured.
- The new control strategy needs further investigation and implementation in a real WPGS. The results from real WPGS can be compared with results provided by this study, which have been obtained experimentally.
- Further investigation of the system dynamic performance using the proposed residue control when connecting to the national grid instead of the employed stand-alone load.
- The new residual controller can be implemented in a photovoltaic power generation system and used to control SEPIC to further simplify the SEPIC control system.
- The SEPIC can be tested in a real photovoltaic power system using the proposed SMC.

- The SEPIC topology can be applied to a small-scale PMSG-based WPGS to reduce the current ripples, thereby further improving the system's power efficiency.

Bibliography

[1] International Energy Agency. *Renewables Information 2014*. International Energy Agency, OECD, 2014.

[2] Rajesh Karki, Po Hu, and Roy Billinton. A simplified wind power generation model for reliability evaluation. *Energy conversion, IEEE Transactions on*, 21(2):533–540, 2006.

[3] Ashraf Ahmed, Li Ran, and Jim R Bumby. New constant electrical power soft-stalling control for small-scale vawts. *Energy Conversion, IEEE Transactions on*, 25(4):1152–1161, 2010.

[4] European Wind Energy Association et al. Eastern winds, emerging european wind power markets, 2013.

[5] Thomas B Johansson and Laurie Burnham. *Renewable energy: sources for fuels and electricity*. Island press, 1993.

[6] Ion Bostan, Adrian V Gheorghe, Valeriu Dulgheru, Ion Sobor, Viorel Bostan, and Anatolie Sochirean. *Resilient Energy Systems: Renewables: Wind, Solar, Hydro*, volume 19. Springer Science & Business Media, 2012.

[7] Russell H Plante. *Solar Energy, Photovoltaics, and Domestic Hot Water: A Technical and Economic Guide for Project Planners, Builders, and Property Owners*. Academic Press, 2014.

[8] Mao-Lin Chiang, Chih-Chiang Hua, and Jong-Rong Lin. Direct power control for distributed pv power system. In *Power Conversion Conference, 2002. PCC-Osaka 2002. Proceedings of the*, volume 1, pages 311–315. IEEE, 2002.

[9] KH Hussein, I Muta, T Hoshino, and Ml Osakada. Maximum photovoltaic power tracking: an algorithm for rapidly changing atmospheric conditions. *IEE Proceedings-Generation, Transmission and Distribution*, 142(1):59–64, 1995.

[10] Fumio Harashima, Hiroshi Inaba, Seiji Kondo, and Nobukazu Takashima. Microprocessor-controlled sit inverter for solar energy system. *Industrial Electronics, IEEE Transactions on*, (1):50–55, 1987.

[11] Tony Burton, Nick Jenkins, David Sharpe, and Ervin Bossanyi. *Wind energy handbook*. John Wiley & Sons, 2011.

[12] KH Bergey. The lanchester-betz limit (energy conversion efficiency factor for windmills). *Journal of Energy*, 3(6):382–384, 1979.

[13] ML Ray, AL Rogers, and JG McGowan. Analysis of wind shear models and trends in different terrains. *University of Massachusetts, Department of Mechanical and Industrial Engineering, Renewable Energy Research Laboratory*, 2006.

[14] Robert Howell, Ning Qin, Jonathan Edwards, and Naveed Durrani. Wind tunnel and numerical study of a small vertical axis wind turbine. *Renewable energy*, 35(2):412–422, 2010.

[15] Joanne Hui. An adaptive control algorithm for maximum power point tracking for wind energy conversion systems. 2008.

[16] Muhammad H. Rashid. *Power Electronics Handbook, Third Edition*. Elsevier, 2011.

[17] S Singh, TS Bhatti, and DP Kothari. A new vertical axis wind rotor using convergent nozzles. *International Journal of Power and Energy Systems*, 25(3):174, 2005.

[18] Wikimedia Commons. Off-shore wind farm turbine. `http://commons.wikimedia.org/wiki/File:Off-shore_Wind_Farm_Turbine.jpg`, 2006. [Online; accessed 12-March-2015].

[19] Wikimedia Commonse. wind turbine, royal botanic garden edinburgh, west gate, arboretum place, john hope gatewayl.

http://http://commons.wikimedia.org/wiki/File:20140728_xl_7329-wind_turbine-Royal_Botanic_Garden-Edinburgh-West_Gate-Arboretum_Place_John_Hope_Gateway.JPG. [Online; accessed 12-March-2015.

[20] AJ Mahdi, WH Tang, L Jiang, and QH Wu. A comparative study on variable-speed operations of a wind generation system using vector control. In *International conference on Renewable Energy and Power Quality (ICREPQ)*, 2010.

[21] Ali M Eltamaly, AI Alolah, and Hassan M Farh. *Maximum Power Extraction from Utility-Interfaced Wind Turbines*. INTECH Open Access Publisher, 2013.

[22] JG Slootweg, SWH De Haan, H Polinder, and WL Kling. General model for representing variable speed wind turbines in power system dynamics simulations. *Power Systems, IEEE Transactions on*, 18(1):144–151, 2003.

[23] Donald S Zinger and Eduard Muljadi. Annualized wind energy improvement using variable speeds. *Industry Applications, IEEE Transactions on*, 33(6):1444–1447, 1997.

[24] J Marques, H Pinheiro, HA Gründling, JR Pinheiro, and HL Hey. A survey on variable-speed wind turbine system. *network*, 24:26, 2003.

[25] YD Song, B Dhinakaran, and XY Bao. Variable speed control of wind turbines using nonlinear and adaptive algorithms. *Journal of Wind Engineering and Industrial Aerodynamics*, 85(3):293–308, 2000.

[26] Quincy Wang and Liuchen Chang. An intelligent maximum power extraction algorithm for inverter-based variable speed wind turbine systems. *Power Electronics, IEEE Transactions on*, 19(5):1242–1249, 2004.

[27] Janardan Gupta, Ashwani Kumar, et al. Fixed pitch wind turbine-based permanent magnet synchronous machine model for wind energy conversion systems. *Journal of Engineering and Technology*, 2(1):52, 2012.

[28] Rajib Datta and VT Ranganathan. A method of tracking the peak power points for a variable speed wind energy conversion system. *Energy conversion, ieee transactions on*, 18(1):163–168, 2003.

[29] Krešimir Vrdoljak, Nedjeljko Perić, and Ivan Petrović. Sliding mode based load-frequency control in power systems. *Electric power systems research*, 80(5):514–527, 2010.

[30] Joshua Yen and Noor Ahmed. Improving safety and performance of small-scale vertical axis wind turbines. *Procedia Engineering*, 49:99–106, 2012.

[31] Iulian Munteanu, Antoneta Iuliana Bratcu, Nicolaos-Antonio Cutululis, and Emil Ceanga. *Optimal control of wind energy systems: towards a global approach*. Springer Science & Business Media, 2008.

[32] C Ghiţă, AI Chirilă, ID Deaconu, and ID Ilina. Wind turbine permanent magnet synchronous generator magnetic field study. In *International Conference of Renewable Energy and Power Quality (ICREPQ'08), Santander, Spain*, 2008.

[33] A. Grauers. *Design of Direct-driven Permanent-magnet Generators for Wind Turbines*. PhD thesis, University of Technology, may 1996.

[34] Yoshikazu Higuchi, Naoki Yamamura, Muneaki Ishida, and Takamasa Hori. An improvement of performance for small-scaled wind power generating system with permanent magnet type synchronous generator. In *Industrial Electronics Society, 2000. IECON 2000. 26th Annual Confjerence of the IEEE*, volume 2, pages 1037–1043. IEEE, 2000.

[35] M Kesraoui, O Bencherouda, and Z Mesbahi. Power control of a pmsg based wind turbine system above rated wind speed. In *International Renewable Energy Congress*, 2010.

[36] Salma El Aimani. Modeling and control structures for variable speed wind turbine. In *Multimedia Computing and Systems (ICMCS), 2011 International Conference on*, pages 1–5. IEEE, 2011.

[37] Torbjorn Thiringer and Jan Linders. Control by variable rotor speed of a fixed-pitch wind turbine operating in a wide speed range. *Energy Conversion, IEEE Transactions on*, 8(3):520–526, 1993.

[38] GD Moor and HJ Beukes. Maximum power point trackers for wind turbines. In *Power Electronics Specialists Conference, 2004. PESC 04. 2004 IEEE 35th Annual*, volume 3, pages 2044–2049. IEEE, 2004.

[39] Andrew Miller, Edward Muljadi, and Donald S Zinger. A variable speed wind turbine power control. *IEEE Transactions on Energy Conversion*, 12(2), 1997.

[40] B Neammanee, S Sirisumranukul, and S Chatratana. Control performance analysis of feedforward and maximum peak power tracking for small-and medium-sized fixed pitch wind turbines. In *Control, Automation, Robotics and Vision, 2006. ICARCV'06. 9th International Conference on*, pages 1–7. IEEE, 2006.

[41] Kendouci Khadija, Mazari Benyounes, Bouserhane Ismain Khalil, and Benhadria Mohamed Rachid. A simple and robust speed tracking control of pmsm. *Przeglad Elektrotechniczny*, 87(7):202–207, 2011.

[42] Georges M El-Murr, Damian Giaouris, and John W Finch. Sensorless speed estimation of pmsm near zero speed using online short time fourier transform ridges. In *World Congress on Engineering*, pages 481–485, 2007.

[43] Ji-Hoon Jang, Seung-Ki Sul, Jung-Ik Ha, Kozo Ide, and Mitsujiro Sawamura. Sensorless drive of surface-mounted permanent-magnet motor by high-frequency signal injection based on magnetic saliency. *Industry Applications, IEEE Transactions on*, 39(4):1031–1039, 2003.

[44] Yu-seok Jeong, Robert D Lorenz, Thomas M Jahns, and Seung-Ki Sul. Initial rotor position estimation of an interior permanent-magnet synchronous machine using carrier-frequency injection methods. *Industry Applications, IEEE Transactions on*, 41(1):38–45, 2005.

[45] Wei Qiao, Xu Yang, and Xiang Gong. Wind speed and rotor position sensorless control for direct-drive pmg wind turbines. *Industry Applications, IEEE Transactions on*, 48(1):3–11, 2012.

[46] Hye-Su Shin, Chengde Xu, Joon-Min Lee, Jae-Du La, and Young-Seok Kim. Mppt control technique for a pmsg wind generation system by

the estimation of the wind speed. In *Electrical Machines and Systems (ICEMS), 2012 15th International Conference on*, pages 1–6. IEEE, 2012.

[47] Paul P Acarnley and John F Watson. Review of position-sensorless operation of brushless permanent-magnet machines. *Industrial Electronics, IEEE Transactions on*, 53(2):352–362, 2006.

[48] Aakanksha Girolkar and G Bhuvaneswari. Control of pmbldc motor using back emf sensing with adaptive filtering. In *Computer Communication and Informatics (ICCCI), 2013 International Conference on*, pages 1–5. IEEE, 2013.

[49] Joanne Hui and Alireza Bakhshai. A new adaptive control algorithm for maximum power point tracking for wind energy conversion systems. In *Power Electronics Specialists Conference, 2008. PESC 2008. IEEE*, pages 4003–4007. IEEE, 2008.

[50] Syed Muhammad Raza Kazmi, Hiroki Goto, Hai-Jiao Guo, and Osamu Ichinokura. A novel algorithm for fast and efficient speed-sensorless maximum power point tracking in wind energy conversion systems. *Industrial Electronics, IEEE Transactions on*, 58(1):29–36, 2011.

[51] AJ Mahdi, WH Tang, and QH Wu. Estimation of tip speed ratio using an adaptive perturbation and observation method for wind turbine generator systems. In *Renewable Power Generation (RPG 2011), IET Conference on*, pages 1–6. IET, 2011.

[52] Kathryn E Johnson, Lucy Y Pao, Mark J Balas, and Lee J Fingersh. Control of variable-speed wind turbines: standard and adaptive techniques for maximizing energy capture. *Control Systems, IEEE*, 26(3):70–81, 2006.

[53] Liuying Li, Yaxing Ren, Lin Jiang, Joseph Brindley, and Victor Bellido-Gonzalez. Hardware implementation of smooth region switching for wind turbine control using pdf controller. In *Renewable Energy Research and Applications (ICRERA), 2013 International Conference on*, pages 115–120. IEEE, 2013.

[54] Lucy Y Pao and Kathryn E Johnson. A tutorial on the dynamics and control of wind turbines and wind farms. In *American Control Conference, 2009. ACC'09.*, pages 2076–2089. IEEE, 2009.

[55] EA Bossanyi. The design of closed loop controllers for wind turbines. *Wind energy*, 3(3):149–163, 2000.

[56] Vladimir Lazarov, Daniel Roye, Dimitar Spirov, and Zahari Zarkov. New control strategy for variable speed wind turbine with dc-dc converters. In *Power Electronics and Motion Control Conference (EPE/PEMC), 2010 14th International*, pages T12–120. IEEE, 2010.

[57] Bongsob Song and J Karl Hedrick. *Dynamic surface control of uncertain nonlinear systems: an LMI approach*. Springer Science & Business Media, 2011.

[58] L. Jiang. *NONLINEAR ADAPTIVE CONTROL AND APPLICATIONS IN POWER SYSTEMS*. PhD thesis, University of Liverpool, March 2001.

[59] Farzad Esfandiari and Hassan K Khalil. Output feedback stabilization of fully linearizable systems. *International Journal of Control*, 56(5):1007–1037, 1992.

[60] Randy A Freeman and Petar V Kokotovic. *Robust nonlinear control design: state-space and Lyapunov techniques*. Springer Science & Business Media, 2008.

[61] Arie Levant. Sliding order and sliding accuracy in sliding mode control. *International journal of control*, 58(6):1247–1263, 1993.

[62] Leonid Fridman and Arie Levant. Higher order sliding modes. *Sliding mode control in engineering*, 11:53–102, 2002.

[63] F Valenciaga and PF Puleston. High-order sliding control for a wind energy conversion system based on a permanent magnet synchronous generator. *Energy Conversion, IEEE Transactions on*, 23(3):860–867, 2008.

[64] Tenoch Gonzalez, Jaime A Moreno, and Leonid Fridman. Variable gain super-twisting sliding mode control. *Automatic Control, IEEE Transactions on*, 57(8):2100–2105, 2012.

[65] Arie Levant. Principles of 2-sliding mode design. *Automatica*, 43(4):576–586, 2007.

[66] Kamal Youcef-Toumi and S-T Wu. Input/output linearization using time delay control. *Journal of dynamic systems, measurement, and control*, 114(1):10–19, 1992.

[67] Kamal Youcef-Toumi and Osamu Ito. A time delay controller for systems with unknown dynamics. *Journal of dynamic systems, measurement, and control*, 112(1):133–142, 1990.

[68] Li-Xia Sun, Zhe Wang, Feng-Ling Han, and Feng Yong. A chattering-free terminal sliding mode control of direct-drive pmsg for wind generation system. In *Cyber Technology in Automation, Control, and Intelligent Systems (CYBER), 2014 IEEE 4th Annual International Conference on*, pages 296–301. IEEE, 2014.

[69] Ming Yin, Gengyin Li, Ming Zhou, and Chengyong Zhao. Modeling of the wind turbine with a permanent magnet synchronous generator for integration. In *Power Engineering Society General Meeting, 2007. IEEE*, pages 1–6. IEEE, 2007.

[70] Shigeo Morimoto, Tomohiko Nakamura, and Yoji Takeda. Power maximization control of variable speed wind generation system using permanent magnet synchronous generator. *IEEJ Transactions on Power and Energy*, 123:1573–1579, 2003.

[71] Md E Haque, Michael Negnevitsky, and Kashem M Muttaqi. A novel control strategy for a variable-speed wind turbine with a permanent-magnet synchronous generator. *Industry Applications, IEEE Transactions on*, 46(1):331–339, 2010.

[72] Bin Wu, Yongqiang Lang, Navid Zargari, and Samir Kouro. Wind generators and modeling. *Power Conversion and Control of Wind Energy Systems*, pages 49–85, 2011.

[73] Ali Jafer Mahdi. *Development of novel sensorless maximum power point tracking controllers for wind turbine generator systems*. PhD thesis, University of Liverpool, Liverpool, may 2011.

[74] Simin Jiang, Jiangang Liang, Ya-dong Liu, Kazuo Yamazaki, and Makoto Fujishima. Modeling and cosimulation of fpga-based svpwm control for pmsm. In *Industrial Electronics Society, 2005. IECON 2005. 31st Annual Conference of IEEE*, pages 6–pp. IEEE, 2005.

[75] András Zentai and Tamás Dabóczi. Improving motor current control using decoupling technique. In *Computer as a Tool, 2005. EUROCON 2005. The International Conference on*, volume 1, pages 354–357. IEEE, 2005.

[76] Muhammad H Rashid. *Power electronics handbook: devices, circuits and applications*. Academic press, 2010.

[77] BM Hasaneen and Adel A Elbaset Mohammed. Design and simulation of dc/dc boost converter. In *Power System Conference, 2008. MEPCON 2008. 12th International Middle-East*, pages 335–340. IEEE, 2008.

[78] DRAGAN Maksimović, ALEKSANDAR M Stanković, V Joseph Thottuvelil, and George C Verghese. Modeling and simulation of power electronic converters. *Proceedings of the IEEE*, 89(6):898–912, 2001.

[79] Marian K Kazimierczuk. *Pulse-width modulated DC-DC power converters*. John Wiley & Sons, 2008.

[80] RB Ridley. Average small-signal analysis of the boost power factor correction circuit. In *VPEC seminar proceedings*, pages 108–120, 1989.

[81] Alberto Reatti and Marian K Kazimierczuk. Small-signal model of pwm converters for discontinuous conduction mode and its application for boost converter. *Circuits and Systems I: Fundamental Theory and Applications, IEEE Transactions on*, 50(1):65–73, 2003.

[82] Karl Johan Åström and Tore Hägglund. *Advanced PID control*. ISA-The Instrumentation, Systems, and Automation Society; Research Triangle Park, NC 27709, 2006.

[83] European Wind Energy Association et al. The european offshore wind industry key 2011 trends and statistics, 2012.

[84] AJ Mahdi, WH Tang, and QH Wu. Parameter identification of a pmsg using a pso algorithm based on experimental tests. In *Energy, Power and Control (EPC-IQ), 2010 1st International Conference on*, pages 39–44. IEEE, 2010.

[85] Bijnan Bandyopadhyay, Fulwani Deepak, and Kyung-Soo Kim. *Sliding mode control using novel sliding surfaces*, volume 392. Springer, 2009.

[86] Fernando Castaños and Leonid Fridman. Analysis and design of integral sliding manifolds for systems with unmatched perturbations. *Automatic Control, IEEE Transactions on*, 51(5):853–858, 2006.

[87] Arnau Doria-Cerezo, Vadim I Utkin, Raul Santiago Munoz-Aguilar, and Enric Fossas. Control of a stand-alone wound rotor synchronous generator: two sliding mode approaches via regulation of the d-voltage component. *Control Systems Technology, IEEE Transactions on*, 20(3):779–786, 2012.

[88] Anders Grauers. *Design of direct-driven permanent-magnet generators for wind turbines*. PhD thesis, School of Electrical and Computer Engineering, Chalmers University of Technology, 1996.

[89] Texas Instruments Europe. Field orientated control of 3-phase ac-motors. *Literature Number: BPRA073*, 1998.

[90] Y. Errami, M. Maaroufi, and M. Ouassaid. Variable structure direct torque control and grid connected for wind energy conversion system based on the pmsg. In *Complex Systems (ICCS), 2012 International Conference on*, pages 1–6, 2012.

[91] Gui-Jia Su, George W Ott, John W McKeever, Kelly S Samons, and Roy L Kessinger. Development of a sensor-less speed control inverter for an automotive accessory permanent magnet motor. In *2000 Future Car Congress*, 2000.

[92] Tomonobu Senjyu, Satoshi Tamaki, Naomitsu Urasaki, Katsumi Uezato, Toshihisa Funabashi, and Hideki Fujita. Wind velocity and position

sensorless operation for pmsg wind generator. In *Power Electronics and Drive Systems, 2003. PEDS 2003. The Fifth International Conference on*, volume 1, pages 787–792. IEEE, 2003.

[93] Lennart Harnefors and H-P Nee. A general algorithm for speed and position estimation of ac motors. *Industrial Electronics, IEEE Transactions on*, 47(1):77–83, 2000.

[94] Yue Zhao, Wei Qiao, and Long Wu. Position extraction from a discrete sliding-mode observer for sensorless control of ipmsms. In *Industrial Electronics (ISIE), 2012 IEEE International Symposium on*, pages 725–730. IEEE, 2012.

[95] Fernando Soares dos Reis, K Tan, and S Islam. Using pfc for harmonic mitigation in wind turbine energy conversion systems. In *Industrial Electronics Society, 2004. IECON 2004. 30th Annual Conference of IEEE*, volume 3, pages 3100–3105. IEEE, 2004.

[96] DM Whaley, WL Soong, and Nesimi Ertugrul. Investigation of switched-mode rectifier for control of small-scale wind turbines. In *Industry Applications Conference, 2005. Fourtieth IAS Annual Meeting. Conference Record of the 2005*, volume 4, pages 2849–2856. IEEE, 2005.

[97] Rene Spee, Shibashis Bhowmik, and Johan HR Enslin. Adaptive control strategies for variable-speed doubly-fed wind power generation systems. In *Industry Applications Society Annual Meeting, 1994., Conference Record of the 1994 IEEE*, pages 545–552. IEEE, 1994.

[98] Marcelo Godoy Simoes, Bimal K Bose, and Ronald J Spiegel. Fuzzy logic based intelligent control of a variable speed cage machine wind generation system. *Power Electronics, IEEE Transactions on*, 12(1):87–95, 1997.

[99] Eftichios Koutroulis and Kostas Kalaitzakis. Design of a maximum power tracking system for wind-energy-conversion applications. *Industrial Electronics, IEEE Transactions on*, 53(2):486–494, 2006.

[100] GLo Bianco, O Honorati, and F Mezzetti. Small-size stand alone wind energy conversion system for battery-charging. *TECHNOLOGICAL EDUCATIONAL INSTITUTE, IRAKLIO,(GREECE).*, 1:62–65, 1996.

[101] Luca Solero, Federlco Caricchi, Fabio Crescimbini, Onorato Honorati, and Fabio Mezzetti. Performance of a 10 kw power electronic interface for combined wind/pv isolated generating systems. In *Power Electronics Specialists Conference, 1996. PESC'96 Record., 27th Annual IEEE*, volume 2, pages 1027–1032. IEEE, 1996.

[102] Don Krupp and Yuri B Shtessel. Chattering-free sliding mode control with unmodeled dynamics. In *American Control Conference, 1999. Proceedings of the 1999*, volume 1, pages 530–534. IEEE, 1999.

[103] G Bartolini and P Pydynowski. An improved, chattering free, vsc scheme for uncertain dynamical systems. *Automatic Control, IEEE Transactions on*, 41(8):1220–1226, 1996.

[104] G Bartolini, A Ferrara, and E Usani. Chattering avoidance by second-order sliding mode control. *Automatic control, IEEE Transactions on*, 43(2):241–246, 1998.

[105] Joseph Bak and Donald J Newman. *Complex analysis*. Springer, 2010.

[106] Eduardo Cattani and Alicia Dickenstein. Introduction to residues and resultants. In *Solving polynomial equations*, pages 1–61. Springer, 2005.

[107] Rolf Herman Nevanlinna and Veikko Paatero. *Introduction to complex analysis*, volume 310. American Mathematical Soc., 1969.

[108] Ilía Nikolaevich Bronshtein, Konstantin Adolfovich Semendiaev, and Kurt August Hirsch. *Handbook of mathematics*. Van Nostrand Reinhold New York, 1985.

[109] Mattias Sandberg. Convergence of the forward euler method for non-convex differential inclusions. *SIAM Journal on Numerical Analysis*, 47(1):308–320, 2008.

[110] Desmond J Higham, Xuerong Mao, and Andrew M Stuart. Strong convergence of euler-type methods for nonlinear stochastic differential equations. *SIAM Journal on Numerical Analysis*, 40(3):1041–1063, 2002.

[111] Morten Bjørhus. A note on the convergence of discretized dynamic iteration. *BIT Numerical Mathematics*, 35(2):291–296, 1995.

[112] Kenneth Eriksson, Don Estep, and Claes Johnson. Applied mathematics body and soul: Vol i-iii. In *Springer-Verlag Publishing*. Citeseer, 2003.

[113] Yue Wang, David G Infield, Bruce Stephen, and Stuart J Galloway. Copula-based model for wind turbine power curve outlier rejection. *Wind Energy*, 2013.

[114] Jae Ho Lee, HyunSu Bae, and Bo Hyung Cho. Advanced incremental conductance mppt algorithm with a variable step size. In *Power Electronics and Motion Control Conference, 2006. EPE-PEMC 2006. 12th International*, pages 603–607. IEEE, 2006.

[115] Marcian Cirstea, Andrei Dinu, Malcolm McCormick, and Jeen Ghee Khor. *Neural and fuzzy logic control of drives and power systems*. Access Online via Elsevier, 2002.

[116] Abdel Ghani Aissaoui, Mohamed Abid, Hamza Abid, Ahmed Tahour, and Abdel Kader Zeblah. A fuzzy logic controller for synchronous machine. *JOURNAL OF ELECTRICAL ENGINEERING-BRATISLAVA-*, 58(5):285, 2007.

[117] Marco Tursini, Roberto Petrella, and Alessia Scafati. Speed and position estimation for pm synchronous motor with back-emf observer. In *Industry Applications Conference, 2005. Fourtieth IAS Annual Meeting. Conference Record of the 2005*, volume 3, pages 2083–2090. IEEE, 2005.

[118] Francesco Parasiliti, Roberto Petrella, and Marco Tursini. Sensorless speed control of a pm synchronous motor by sliding mode observer. In *Industrial Electronics, 1997. ISIE'97., Proceedings of the IEEE International Symposium on*, pages 1106–1111. IEEE, 1997.

[119] Takeshi Furuhashi, Somboon Sangwongwanich, and Shigeru Okuma. A position-and-velocity sensorless control for brushless dc motors using an adaptive sliding mode observer. *Industrial Electronics, IEEE Transactions on*, 39(2):89–95, 1992.

[120] S Bolognani, L Tubiana, and M Zigliotto. Sensorless control of pm synchronous motors with non-sinusoidal back emf for home appliance. In *Electric Machines and Drives Conference, 2003. IEMDC'03. IEEE International*, volume 3, pages 1882–1888. IEEE, 2003.

[121] Kerim Guney and Nurcan Sarikaya. Comparison of mamdani and sugeno fuzzy inference system models for resonant frequency calculation of rectangular microstrip antennas. *Progress In Electromagnetics Research B*, 12:81–104, 2009.

[122] AJ Mahdi, WH Tang, and QH Wu. Improvement of a mppt algorithm for pv systems and its experimental validation. In *International Conference on Renewable Energies and Power Quality, Granada, Spain*, 2010.

[123] V Salas, E Olias, A Barrado, and A Lazaro. Review of the maximum power point tracking algorithms for stand-alone photovoltaic systems. *Solar energy materials and solar cells*, 90(11):1555–1578, 2006.

[124] DP Hohm and ME Ropp. Comparative study of maximum power point tracking algorithms using an experimental, programmable, maximum power point tracking test bed. In *Photovoltaic Specialists Conference, 2000. Conference Record of the Twenty-Eighth IEEE*, pages 1699–1702. IEEE, 2000.

[125] Nicola Femia, Giovanni Petrone, Giovanni Spagnuolo, and Massimo Vitelli. Optimization of perturb and observe maximum power point tracking method. *Power Electronics, IEEE Transactions on*, 20(4):963–973, 2005.

[126] A El Shahat. Stand-alone pv system simulation for dg applications. *Journal of Automation & Systems Engineering*, 6(1):55–72, 2012.

[127] MA Alsumiri, WH Tang, and QH Wu. Maximum power point tracking for wind generator system using sliding mode control. In *Power and Energy Engineering Conference (APPEEC), 2013 IEEE PES Asia-Pacific*, pages 1–6. IEEE, 2013.

[128] Il-Song Kim. Robust maximum power point tracker using sliding mode controller for the three-phase grid-connected photovoltaic system. *Solar Energy*, 81(3):405–414, 2007.

[129] Siew-Chong Tan, YM Lai, Chi K Tse, and Martin KH Cheung. An adaptive sliding mode controller for buck converter in continuous conduction mode. In *Applied Power Electronics Conference and Exposition, 2004.*

APEC'04. Nineteenth Annual IEEE, volume 3, pages 1395–1400. IEEE, 2004.

[130] H Tarik Duru. A maximum power tracking algorithm based on¡ i¿ i¡/i¿¡ sub¿ mpp¡/sub¿=¡ i¿ f¡/i¿(¡ i¿ p¡/i¿¡ sub¿ max¡/sub¿) function for matching passive and active loads to a photovoltaic generator. *Solar Energy*, 80(7):812–822, 2006.

[131] JABER Ghazanfari and MM Farsangi. Maximum power point tracking using sliding mode control for photovoltaic array. *Iranian Journal of Electrical & Electronic Engineering*, 9(3):189, 2013.

[132] Roberto Faranda and Sonia Leva. Energy comparison of mppt techniques for pv systems. *WSEAS transactions on power systems*, 3(6):446–455, 2008.

[133] Amirnaser Yazdani and Prajna Paramita Dash. A control methodology and characterization of dynamics for a photovoltaic (pv) system interfaced with a distribution network. *Power Delivery, IEEE Transactions on*, 24(3):1538–1551, 2009.

[134] Anca Daniela Hansen, Poul Ejnar Sørensen, Lars H Hansen, and Henrik W Bindner. *Models for a Stand-alone PV System*. Riso National Laboratory, Roskilde, 2001.

[135] Sumita Dhali, P Nageshwara Rao, Praveen Mande, and K Venkateswara Rao. Pwm-based sliding mode controller for dc-dc boost converter. *International Journal of Engineering Research and Applications*, 2(1):618–623, 2012.

[136] Nur Mohammad, Muhammad Quamruzzaman, Mohammad Rubaiyat Tanvir Hossain, and Mohammad Rafiqul Alam. Parasitic effects on the performance of dc-dc sepic in photovoltaic maximum power point tracking applications. *Smart Grid & Renewable Energy*, 4(1), 2013.